Measurement of the W boson polarization in top quark decays using the di-lepton final state of the top quark pair in pp collisions with $\sqrt{s} = 7$ TeV

重心系エネルギー7 TeV の陽子陽子衝突事象における トップクォーク対のダイレプトン終状態を用いた トップクォーク崩壊事象中のWボソン偏極度測定

Satoshi HASEGAWA
長谷川 慧

Contents

1 Theoretical background 1

1.1 The standard model and the top quark 1

1.1.1 Quarks and leptons 1

1.1.2 Gauge bosons 2

1.1.3 The Higgs mechanism 2

1.1.4 Unsettled issues in the SM, and the top quark 3

1.2 The top quark pair production and decay in the LHC 4

1.2.1 Theoretical view 4

Parton model and Parton Distribution Function 4

The top quark decay via the weak interaction 5

The *W* boson decay and categorization of the top quark pair decay 6

Parton showering and hadronization 6

1.2.2 Measurement of the top quark pair production cross section 7

1.3 The *W* boson polarization and the top quark decay vertex *Wtb* in the SM 7

1.4 Generalized *Wtb* vertex and *W* boson polarization 9

2 The LHC-ATLAS experiment 12

2.1 The LHC accelerator 12

2.2 The ATLAS detector 15

2.2.1 Inner Detector 16

Pixel detector 16

SemiConductor Tracker(SCT) 17

Transition Radiation Tracker(TRT) 17

2.2.2 Calorimeter 18

Electromagnetic LAr Calorimeter and pre-sampler 18

Hadron tile calorimeter 20

Hadron endcap LAr calorimeter 20

LAr forward calorimeter 21

Calorimeter signal readout 22

2.2.3 Muon Spectrometer 27

Thin Gap Chambers(TGC) 27

Resistive Plate Chambers(RPC) 27

Monitored Drift Tube detector(MDT) 28

Cathode Strip Chambers(CSC) 28

2.2.4 Solenoid and toroid magnets 29
2.3 Monte Carlo simulation and computer modeling of the ATLAS detector 33
2.4 Object Reconstruction 35
2.4.1 Track Reconstruction at the Inner Detector 35
2.4.2 Electron reconstruction 37
Reconstruction procedure 37
Reconstruction efficiency 38
Energy scale and resolution 39
2.4.3 Muon reconstruction 40
Reconstruction procedure 40
Reconstruction efficiency 41
Momentum scale and resolution 41
2.4.4 Lepton isolation 43
2.4.5 Jet reconstruction 47
Reconstruction procedure 47
Energy and direction calibration 48
Uncertainty on the energy scale 49
Momentum resolution 50
Reconstruction efficiency. 52
Fake jet removal 53
2.4.6 b-tagging of jet 54
2.4.7 Missing transverse momentum($E_{\mathrm{T}}^{\mathrm{miss}}$) 55
2.5 Data Acquisition System at ATLAS 59
2.5.1 ATLAS Trigger System and Lepton Triggers 59
Electron trigger 59
Muon trigger 60
Trigger efficiency scale factor 61
2.6 Luminosity measurement 62

3 Muon detector commissioning and its performance evaluation 65
3.1 The TGC detector commissioning 65
3.1.1 The TGC detector system overview 65
3.1.2 The calibration scheme for long term running 69
3.1.3 The commissioning with cosmic data taking 69
3.1.4 Optimization of the TGC trigger logic based on data 70
3.2 The ATLAS muon detector performance 75
3.2.1 Evaluation of muon momentum scale and resolutions 75
3.2.2 Muon trigger efficiency 80
3.2.3 Muon isolation efficiency 81

4 Measurement of W Boson Polarization in Top Quark Decay with $t\bar{t}$ Di-lepton Mode 85
4.1 Data and basic event selection 85
4.2 Event Selection and Background Estimation 86
4.2.1 Event Selection 86

4.2.2 Drell-Yan background estimation 87
4.2.3 Fake background estimation 88
4.2.4 Event selection criteria 90
4.3 Event Reconstruction 98
4.3.1 The top quark pair reconstruction method 98
4.3.2 The behavior of the reconstruction method 100
4.3.3 Reconstructed top quark pair and $\cos\theta^*$ 104
4.4 W Boson Polarization Measurement and its Physics Interpretation 110
4.4.1 Evaluation of Systematic Uncertainties 116
4.4.2 Combination of the Results with BLUE method. 124
4.4.3 Combination of the di-lepton channels 126
4.4.4 The full combination of analyses in ATLAS 128
4.4.5 Physics Interpretation of the Measured W boson polarization 131

5 Summary **133**

Abstract

The Standard Model (SM) is a framework that has succeeded to describe the behavior of the elementary particle to a great extent. After the discovery of a Higgs-boson-like particle in 2012, its reliability has increased more. At the same time, however, the importance of problems related to the Higgs mechanism such as the fine tuning of the mass of the Higgs particle has grown. In order to find a clue to the problems, the top quark is an interesting subject by focusing on the Higgs mechanism from the following two points. One thing is that the top quark mass of 173.2 ± 0.9 GeV is much larger than that of other fermions such as electron and up-quark although their masses are originated from the same Higgs mechanism. The other is that the top quark mass is at the energy scale of the Higgs mechanism, and it is suspected that the top quark has some relation with it.

In the LHC-ATLAS experiment, where protons are collided with 7 TeV center of mass energy, the precise measurement of the top quark properties with enormous top quark samples is possible through mainly the top quark pair ($t\bar{t}$) production. In the ATLAS experiment, the cross section is measured in the various final states, and the result of $177 \pm 3(\text{stat.})^{+8}_{-7}(\text{syst.}) \pm 7(\text{luminosity})$ is consistent with the SM expectation of $164.6^{+11.4}_{-15.7}$ pb. These analyses however, have counted the number of events inclusively after some event selections. In order to investigate prodution and decay of the top quark more closely, it is quite important to look into the kinematical distributions that strongly relate to the top quark properties.

On that point, the W boson polarization measurement in the top quark decay is important from the point that it directly related to the interaction in the top quark decay. In the SM, the top quark decays into a W boson and a b-quark almost exclusively, with V-A weak interaction. Due to the large decay width, the top quark decays before hadronization and behaviors of bare quark can be observed. Here, the W boson polarization fraction in the SM expectation is

$$
\begin{aligned}
F_0 &= 0.687 \pm 0.005 \\
F_L &= 0.311 \pm 0.005 \\
F_R &= 0.0017 \pm 0.0001
\end{aligned}
$$

where F_0, F_L and F_R are the fraction of W boson polarization in longitudinal, left- and right-handed defined with respect to the momentum direction of the W boson ($F_0 + F_L + F_R = 1$). As the result of V-A interaction, the F_R is strongly suppressed and its deviation from zero stands for the existence of new physics.

The W boson polarization can be measured by the charged lepton emission angle distribution in the leptonic decay of the top quark : $t \to Wb \to l\nu b$. The differential cross section as a function of the charged lepton emission angle is

$$
\frac{1}{N}\frac{\mathrm{d}N}{\mathrm{d}\cos\theta^*} = F_0\frac{3}{4}\sin^2\theta^* + F_L\frac{3}{8}(1-\cos\theta^*)^2 + F_R\frac{3}{8}(1+\cos\theta^*)^2,
$$

where θ^* is defined as the angle between the momentum of the charged lepton on the W boson rest frame and that of the W boson on the top quark rest frame. The angle θ^* in one top quark decay can

be reconstructed by measuring the momentum of the b-quark, charged lepton and neutrino from the top quark.

In this study, proton-proton collision data of 1.04 fb^{-1} accumulated with the ATLAS detector is used. The analysis focuses on the di-lepton final state in which high purity top quark samples can be prepared from 10^9 larger background thanks to the signature of the two charged leptons.

The signature of the charged leptons with high energy is important not only for the $\cos\theta^*$ measurement but also for event trigger of the data acquisition. The existence of such object can be used to reject enormous QCD background events in hadron collisions and the performance of charged lepton trigger is essential. The muon trigger system is established systematially during the commissioning period, and the evaluation of the muon reconstruction performance is done.

Concerning the $t\bar{t}$ event reconstruction, the two neutrinos in the event are also important. This analysis establishes method that can reconstruct all the decay products of the two top quark with keeping the kinematical information. By applying the method on the selected events, the W boson polarization fraction is measured from θ^*(in practical, $\cos\theta^*$) distribution and the result is

$$\begin{aligned} F_0 &= 0.920 \pm 0.095(\text{stat.}) \pm 0.104(\text{syst.}) \\ F_L &= 0.172 \pm 0.063(\text{stat.}) \pm 0.074(\text{syst.}) \\ F_R &= -0.092 \pm 0.046(\text{stat.}) \pm 0.057(\text{syst.}). \end{aligned}$$

The background is lowered to almost negligible level as expected, and the uncertainty from the background contribution is less than 0.01. The result is consistent with the SM expectation, for example, F_R is consistent with zero. Also it is consistent with other W boson polarization measurement in the ATLAS experiment.

This analysis is the first measurement of the W boson polarization in the top quark decay in proton-proton collisions at a center of mass energy of 7 TeV. Following the inclusive cross section measurement, this is a more precise measurement by focusing on kinematical variables and the results is consistent with the SM with its uncertainty. In addition to the method to reconstruct $t\bar{t}$ with the di-lepton final state, this study provides the validity of the $t\bar{t}$ production and decay modeling for the future analyses related to the $t\bar{t}$ di-lepton or di-lepton-like signatures such as a fourth-generation quark t' and the charged Higgs boson decays.

Chapter 1

Theoretical background

1.1 The standard model and the top quark

The Standard Model (SM) is a framework based on the quantum field theory, gauge invariance and the Higgs mechanism. In the quantum field theory, all the particles are regarded as excitation state of the corresponding fields. The gauge invariance and the Higgs mechanism introduce interactions and masses as written below.

1.1.1 Quarks and leptons

Discovered elementary fermions categorized as *quarks* u_i, d_i and and *leptons* ν_i, ℓ_i ($i = 1, 2, 3$). The difference between them is that quarks have color charges(red, blue and green). They are furthermore categorized into further according to their chirality left (L) or right (R), and electromagnetic charges Q. Table 1.1 summarize the categorization and their names. The reputation of the structure by index i is called *generation*.

	First generation	Second generation	Third generation	Q	weak charge
quark	$\begin{pmatrix} u(\text{up}) \\ d(\text{down}) \end{pmatrix}_L$	$\begin{pmatrix} c(\text{charm}) \\ s(\text{strange}) \end{pmatrix}_L$	$\begin{pmatrix} t(\text{top}) \\ b(\text{bottom}) \end{pmatrix}_L$	2/3	1/2 + 2/3 $\sin^2\theta_W$
				-1/3	-1/2 - 1/3 $\sin^2\theta_W$
	u_R	c_R	t_R	2/3	2/3 $\sin^2\theta_W$
	d_R	s_R	b_R	-1/3	-1/3 $\sin^2\theta_W$
lepton	$\begin{pmatrix} \nu_e(e\text{−neutrino}) \\ e(\text{electron}) \end{pmatrix}_L$	$\begin{pmatrix} \nu_\mu(\mu\text{−neutrino}) \\ \mu(\text{muon}) \end{pmatrix}_L$	$\begin{pmatrix} \nu_\tau(\tau\text{−neutrino}) \\ \tau(\text{tau}) \end{pmatrix}_L$	0	1/2
				-1	$-1/2 - \sin^2\theta_W$
	e_R	μ_R	τ_R	-1	$-\sin^2\theta_W$

Table 1.1: The categorization of the fermions. The left handed particles form doublets. θ_W is the Weinberg angle. The color triplet of quarks is omitted in this table.

		gauge boson	corresponding charge
electroweak	electromagnetic	photon (γ)	electromagnetic charge
	weak	W boson	hyper charge
		Z boson	weak charge
strong		gluon (g)	color

Table 1.2: The gauge bosons in the SM and corresponding force and charge.

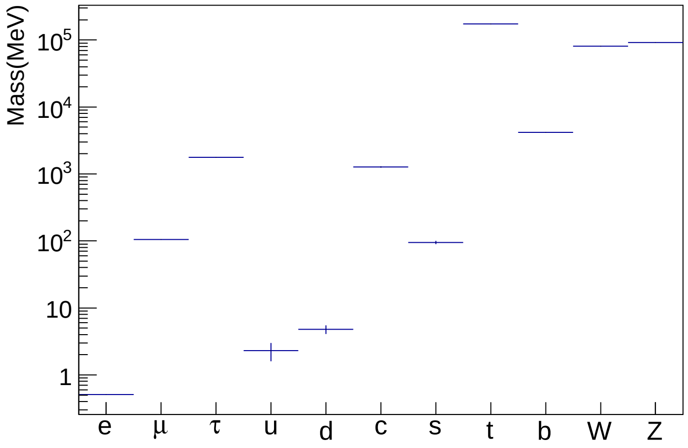

Figure 1.1: The masses of the elementary particles [1]. Masses of the neutrinos are < 2 eV.

1.1.2 Gauge bosons

The forces, propagated by the gauge bosons with spin 1, are introduced naturally from the principle of the gauge invariance under $\mathrm{SU(3)_C \times SU(2)_W \times U(1)_Y}$ transformation. Table 1.2 summarizes the relation between the symmetry, gauge boson and the charges to which the gauge boson couple. Gauge boson related to $\mathrm{SU(3)_C}$ is *gluon*, and couples to color triplets of quarks. The counterpart of $\mathrm{SU(2)_L}$ and $\mathrm{U(1)_Y}$ are mixed and form $W^{\pm}/Z$ bosons and photon γ that correspond to the weak interaction and electromagnetic interaction respectively. As the result of the mixture, the W boson does interact only with particles with chirality left.

1.1.3 The Higgs mechanism

Observed quarks and $W^{\pm}, Z$ bosons have masses. The principle of the gauge invariance, however, prohibits them from having their masses in the SM. Instead, the SM introduces the Higgs field, which is a doublet of scalar complex fields, and quarks and $W^{\pm}, Z$ bosons couple to the Higgs field. The Higgs field has a special potential and its vacuum expectation value has non-zero value of 246 GeV. Here, the coupling between quarks, $W^{\pm}, Z$ bosons and the vacuum of the Higgs field plays as their masses. Figure 1.1 shows the masses of the elementary particles. Three out of four degrees of freedom are used for the redefinition of the $W^{\pm}, Z$ bosons here, and the one is left as a physical object, that is the Higgs particle. It is worth mentioning that the mass is only the parameter to distinguish particles in different generations. In other words, the coupling of fermions with the Higgs field introduces the generation structure into the model.

1.1.4 Unsettled issues in the SM, and the top quark

Although the SM succeeded to explain observed results to a great extent, it has also some difficulties. For example, from the point of view of forces, the SM does not include gravity. While it unites the electromagnetic and weak interaction as electroweak interaction at energy scale of 100 GeV, the unification of strong interaction is not achieved in the theory. On top of that, the unification is expected to be around the GUT scale $\sim 10^{15}$ GeV. Here the interval between it and the electroweak scale is needed to be explained, which is so-called *hierarchy problem*. From the point of view of unnaturalness of the theory, the SM explains Higgs mass of 126 GeV as the result of a cancellation of large intrinsic Higgs mass of scale $O(10^{19})$ GeV and also large quantum correction to it of scale $O(10^{19})$ GeV, so-called *fine-tuning problem*.

Aiming at conquering them, various theoretical models such as suppersymmetry have been proposed, which result in introduction of new particles. But no new particle out of the SM has been discovered so far.

Some particles in these proposed theories are expected to be heavy, $O(100)$ GeV or grater, and searches for these particles need high energy colliders such as the Large Hadron Collider(LHC) in order to create them artificially. The LHC has started proton-proton collision with center of mass energy of 7 TeV, and the high statistics of the accumulated data with the ATLAS detector enables to explore new energy regions.

On the other hand, the candidate of the Higgs particle, that had been only the undiscovered particle in the SM, is discovered [2] [3]. There are two points to be clear : one is the understanding of the particle itself, the other is that of the mechanism. As to the later, the top quark is one of the interesting subjects. While the top quark obtains its mass by the Higgs mechanism as all the other quarks do, its mass of 173.2 ± 0.9 GeV [4] is much heavier than that of other quarks, which is not explained in the SM. Furthermore, the mass is at the same enrgy scale as the vacuum expectation value of the Higgs filds after the symmetry breaking. From these points, the top quark can be expected to play important role in the Higgs mechanism.

In addition, in order to claim the existence of any new particle, detail understanding of the known particles, especially the top quark, are unavoidable. The top quark decays to one W boson and one b quark almost exclusively, and the W boson to a pair of quarks or leptons. Due to the large mass of the top quark, thees particles obtain large energies. Especially, high energy charged leptons and apparent imbalance of momentum due to undetectable neutrinos in the decay are also important signature in searches of heavy particles expected in proposed theories beyond the SM.

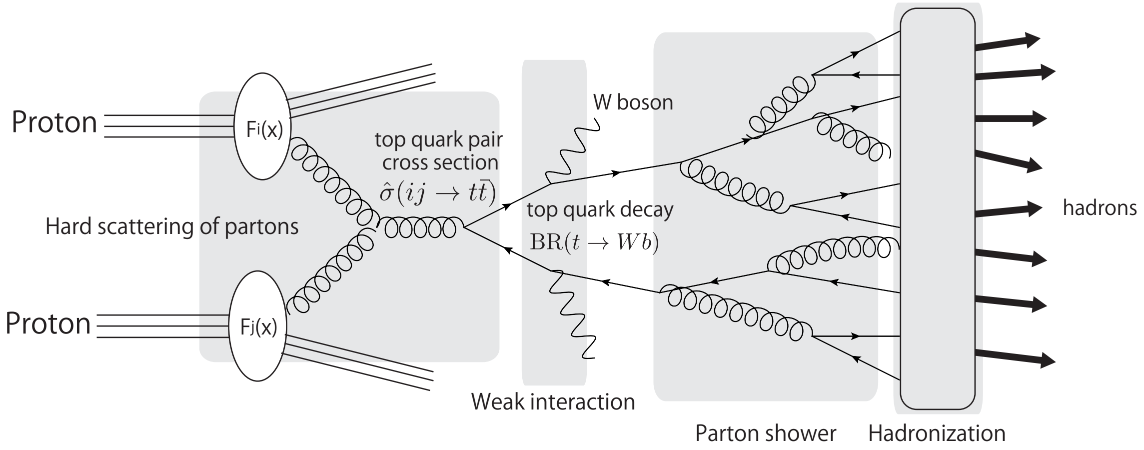

Figure 1.2: A scheme of physics processes in the top quark production and decay. A hard process occurs as collision of partons which distribute in protons with PDF $F_i(x)$, and top quark pair is produced. The produced two top quarks decay into W bosons and bottom quarks each through the weak interaction. The bottom quarks undergo parton showering which is chains of parton emissions, and hadronize.

1.2 The top quark pair production and decay in the LHC

1.2.1 Theoretical view

The main top quark production process in the LHC is top quark pair production. As Figure 1.2 shows, the production and decay process are understood as the integration of knowledge on the proton composition, quantum chromodynamics(QCD), the weak interaction, and radiation and hadronization of quark and gluons, as described below.

Parton model and Parton Distribution Function

High energy collisions of protons are treated as the parton model. This model regards protons as composites of valence quarks, sea quarks and gluons, which are called partons. The valence quarks, which consist of two up-quarks and one down-quark, determine the quantum number of protons. Each parton in a proton carries some fraction x of the total proton energy ($0 < x < 1$). A parton distribution function (PDF) describes the fraction distribution of the partons. Figure 1.3 shows an example of the PDF. In QCD calculation, splitting of a parton into other partons ($q \to qg, g \to gg, g \to q\bar{q}$) appears. Since the effect can be regarded as an effective modification of the PDF, the PDF is defined including this effect. It is defined at some energy scale (usually at the order of 1 GeV), and is extrapolated to the energy scale of the physics of interest which is called renormalization scale μ_R. The extrapolation is done by following the DGLAP evolution equation that takes into accout the partons splitting and also the running of the coupling strength of the strong interaction in accordance with energy scale. Also, in high oder of QCD calculation of some hard process, soft contribution that can change the type of partons appears. Since it also works as effective modification of the PDF, the soft term is cut off from the calculation and is incluced in the PDF definition. This is called factorization and its energy scale

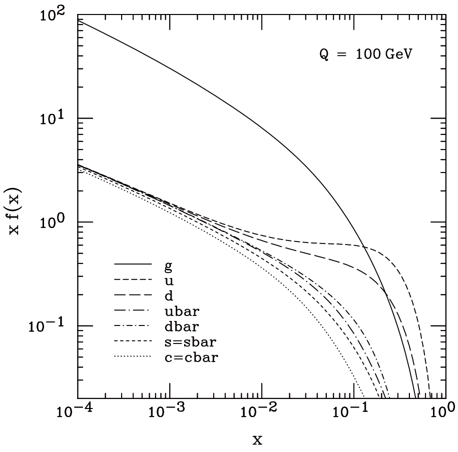

Figure 1.3: An example of parton distribution function at $\mu(Q) = 100$ GeV (calculation of CTEQ6M [5]).

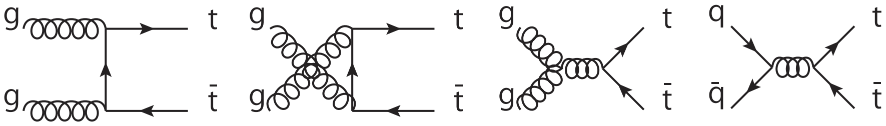

Figure 1.4: Leading order diagram of the top quark pair production [6].

is called factrization scale μ_F.

In the collision of protons, hard interactions occur in the parton level. One parton i from one proton and another j from the other proton contribute the top quark pair production. The cross section of such process can be written as $\hat{\sigma}_{ij\to t\bar{t}}(\hat{s}, \mu_F, \mu_R)$ where $\hat{s}$ is the total energy in the parton interaction, The total cross section of the top quark pair is integration of $\hat{\sigma}$ over the combination of partons :

$$\sigma_{t\bar{t}} = \sum_{i,j=q,\bar{q},g} \int \mathrm{d}x_i \mathrm{d}x_j F_i(x_i, \mu_F) F_j(x_j, \mu_F) \hat{\sigma}_{ij\to t\bar{t}}(\hat{s}, \mu_F, \mu_R) \tag{1.1}$$

where $x_{i,j}$ are the energy fraction of the parton i, j, and $F_{i,j}$ is the PDF for the partons i, j. The leading order processes of the top quark pair production in a hadron collider are $gg \to t\bar{t}$ and $qq \to t\bar{t}$ as Figure 1.4 shows. In the LHC with $\sqrt{s} = 7$ TeV, the contribution from gg account for 80% of the total. This is because the contribution of the gluons in the PDF is large at $x > 0.05$ which is the typical threshold value for the top quark pair production. A theoretical expectation of the next-to-next leading order calculation is $164.6^{+11.4}_{-15.7}$ pb.

The top quark decay via the weak interaction

The top quark decay is induced by only the weak interaction. Produced top quarks by strong interaction is represented by the superposition of the weak interaction eigenstate, and , as the results, the Lagrangian that is related to the top quark decay is written with *Cabbibo-Kobayashi-Masukawa*(CKM) matrix as

$$\mathcal{L} = \frac{g_W}{\sqrt{2}}\Big(V_{td}\bar{d}_L\gamma^\mu W_\mu t_L + V_{ts}\bar{s}_L\gamma^\mu W_\mu t_L + V_{tb}\bar{b}_L\gamma^\mu W_\mu t_L\Big) + \text{h.c.} \tag{1.2}$$

Here $|V_{tb}| \gg |V_{td}|, |V_{ts}|$ and the top quark decays into a bottom quark and a W boson in 99.8% [1].

Furthermore, its decay width is 1.46 GeV which is much larger than the energy scale of QCD. and, it decays before it forms any hadrons unlike other quarks, which means its decay can be treated as that of free quark.

The *W* boson decay and categorization of the top quark pair decay

The W^+ (W^-) boson can decay into a pair of $\{u_L, \bar{d}_L\}$, $\{c_L, \bar{s}_L\}$ or $\{\bar{\ell}_L, \nu_L\}$ (their charge conjugate for W^-), and its branching ratio is [1]

- $W \to$ quarks : 67.6 ± 0.27 %
- $W \to e\nu_e$: 10.75 ± 0.13 %
- $W \to \mu\nu_\mu$: 10.57 ± 0.15 %
- $W \to \tau\nu_\tau$: 11.25 ± 0.20 %

The top quark pair has two W bosons in its intermediate states, and the final state can be categorized based on the decay producets of the W bosons, which are characterized by the number of charged leptons (only e and μ are considered).

- single-lepton : One W boson decays into leptons, and the other to hadrons. This accounts for 34.4% of all the top quark pair decay.
- di-lepton : Both W bosons decay into leptons. 6.5% of the total.
- full hadronic : Both W bosons decay into hadrons. 45.5% of the total

In addition to them, W can decay into τ. leptonic decay of $\tau \to e, \mu$ are included into the single-lepton and di-lepton channels. Other channels where τ decaying into hadrons belong to another category.

Parton showering and hadronization

Generated quarks from a top quark or a W boson may emit gluons and the gluons can also emit gluons and quarks, and they forms some hadrons in the final state. This can be handled with two steps theoretically. The *parton showering model* treats such repetition of generation with a *splitting function* derived from the QCD. The hadronization model transforms gluons into quark pairs, and makes hadrons from the quarks.

---

[1] In the world average [1], the absolute values of the CKM matrix elements are

$$\begin{pmatrix} |V_{ud}| & |V_{us}| & |V_{ub}| \\ |V_{cb}| & |V_{cs}| & |V_{cb}| \\ |V_{tb}| & |V_{ts}| & |V_{tb}| \end{pmatrix} = \begin{pmatrix} 0.97427 \pm 0.00015 & 0.22534 \pm 0.00065 & 0.00351^{+0.00015}_{-0.00014} \\ 0.22520 \pm 0.00065 & 0.97344 \pm 0.00016 & 0.0412^{+0.0011}_{-0.0005} \\ 0.00867^{+0.00029}_{-0.0003} & 0.0404^{+0.0011}_{-0.0005} & 0.999146^{+0.000021}_{-0.000046} \end{pmatrix} \tag{1.3}$$

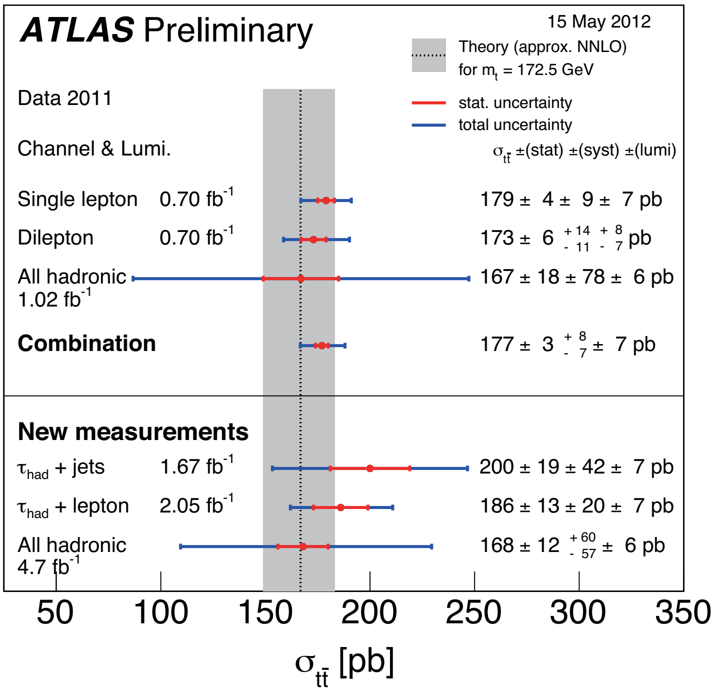

Figure 1.5: Results of the top quark cross section measurements in the ATLAS experiment.

These steps determine the distribution of the hadrons in the final state. The theoretical expectation can be compared to experiments quantitatively by comparing the distribution of directional particle flows from energetic partons, so-called *jets*. The jets are treated as one kind of physics objects as described in section 2.4.5.

1.2.2 Measurement of the top quark pair production cross section

One of the basic quantities of the top quark is the cross section of the top quark pair production. The ATLAS experiment has measured it with various final states as shown in Figure 1.5. Their combined result of $\sigma_{t\bar{t}} = 173.3 \pm 2.3(\text{stat.}) \pm 7.6(\text{syst.}) \pm 6.3(\text{lumi.})$ pb [7] is consistent with the theoretical expectation of $164.6^{+11.4}_{-15.7}$ pb.

The measurements, however, just count the number of events after some event selections. That means they have treated the various steps as shown in Figure 1.2 inclusively. More precise measurements can be achieved by looking into the process of the productions and decays exclusively.

1.3 The *W* boson polarization and the top quark decay vertex *Wtb* in the SM

The *W* boson polarization measurement in the top quark decay is important from the point that it directly related to the interaction in the top quark decay. In the top quark decay, there are three types of decay from the point of view of the W boson polarization as shown in Figure 1.6. In this document, the fraction $F_{L,R,0}$ are defined as

$$F_{L,R,0} = \frac{\Gamma_{L,R,0}(t \to Wb)}{\Gamma_{\text{total}}(t \to Wb)}, \quad (\Gamma_{\text{total}} = \Gamma_L + \Gamma_R + \Gamma_0, \quad F_L + F_R + F_0 = 1) \tag{1.4}$$

where Γ is total or partial decay width of the top quark, and L, R and 0 stand for the W boson polarization of left-, right-handed and longitudinal along the direction of its momentum in the top quark rest frame. In the SM, the top quark decays into a W boson and a b-quark almost exclusively ($\sim 99.8\%$), with V-A weak interaction.

In the leading order calculation with bottom quark massless limit ($m_b \to 0$), the each decay width is

$$\Gamma_0(t \to Wb) = \frac{g^2}{64\pi}|V_{tb}|^2 \frac{m_t^3}{m_W^2}\Big(1 - \frac{m_W^2}{m_t^2}\Big)^2 \tag{1.5}$$

$$\Gamma_L(t \to Wb) = \frac{g^2}{32\pi}|V_{tb}|^2 m_t\Big(1 - \frac{m_W^2}{m_t^2}\Big)^2 \tag{1.6}$$

$$\Gamma_R(t \to Wb) = 0 \tag{1.7}$$

and the polarization fraction is

$$F_0 = \frac{m_t^2}{2m_W^2 + m_t^2} \tag{1.8}$$

$$F_L = \frac{2m_W^2}{2m_W^2 + m_t^2} \tag{1.9}$$

$$F_R = 0 \tag{1.10}$$

Here, $F_R = 0$ is one consequence of the V-A interaction and the ratio of F_0 to F_L is determined only by their masses and $m_t^2/2m_W^2$.

According to a next-to-next leading order calculation [8], the W boson polarization fractions in the SM are

$$F_0 = 0.687 \pm 5 \qquad F_L = 0.311 \pm 5 \qquad F_R = 0.0017 \pm 1 \tag{1.11}$$

where $m_t = 172.8 \pm 1.3$ GeV, $m_W = 80.401 \pm 31$ GeV and $m_b = 4.8$ GeV are assumed. As the result of V-A interaction, the F_R is strongly suppressed and its deviation from zero stands for the existence of new physics. The ratio of F_0 to F_L is determined by the ratio of $m_t^2 : m_W^2$ in the leading order with $m_b \to 0$ limit.

The CDF and D0 experiments have reported a combined result using proton and anti-proton collision data of 2.7 - 5.4 fb^{-1} in the center of mass energy of 1.96 TeV brought by the Tevatron accelerator [9] ($F_L = 1 - F_0 - F_R$):

$$\begin{aligned} F_0 &= 0.722 \pm \pm 0.062(\text{stat.}) \pm 0.052(\text{syst.}) \\ F_R &= -0.033 \pm \pm 0.034(\text{stat.}) \pm 0.031(\text{syst.}) \end{aligned} \tag{1.12}$$

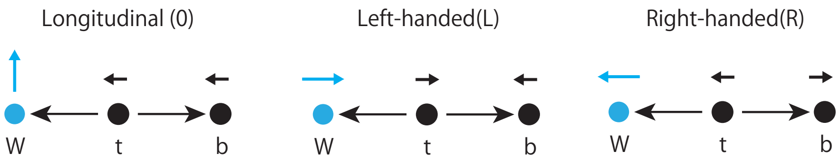

Figure 1.6: The three types of the top quark decay based on the W boson polarization

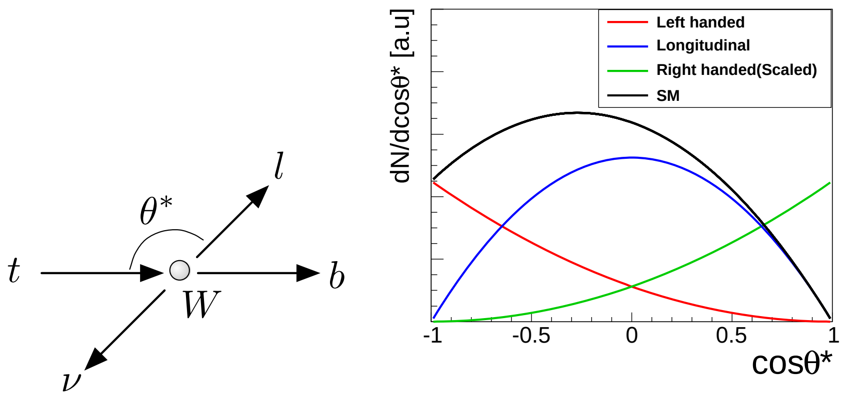

Figure 1.7: (left) The angle θ^* is defined as the supplementary angle of the one between momenta of the charged lepton or down-type quarks from the W boson and the bottom quark on W boson rest frame. (right) The $\cos\theta^*$ distribution from the W boson with each polarization and the SM prediction.

and it is consistent with the SM expectation.

The W boson polarization can be measured experimentally by charged lepton emission angle distribution in the leptonic decay of the top quark :$t \rightarrow Wb \rightarrow l\nu b$. If θ^* is defined, as shown in Figure 1.7(left), as the angle between the momentum of the charged lepton on the W boson rest frame and that of the W boson on the top quark rest frame, the distribution is

$$\frac{1}{N}\frac{\mathrm{d}N}{\mathrm{d}\cos\theta^*} = F_0\frac{3}{4}\sin^2\theta^* + F_L\frac{3}{8}(1-\cos\theta^*)^2 + F_R\frac{3}{8}(1+\cos\theta^*)^2.$$

The angle θ^* in one top quark decay can be reconstructed by measuring the momentum of b-quark, charged lepton and neutrino from the top quark.

Figure 1.7(right) shows the $\cos\theta^*$ distribution in the SM. The suppression of F_R is one of the consequence of the V-A weak interaction, and the ratio between F_L and F_0 is mainly determined by the masses of the top quark and the W boson.

1.4 Generalized *Wtb* vertex and *W* boson polarization

Apart from the SM, generalized interaction of the Wtb vertex is

$$\begin{aligned}\mathcal{L}_{\mathrm{eff}} =& \bar{t}\gamma^{\mu}(V_L P_L + V_R P_R) b W_{\mu} \\ &+ \bar{t} i\sigma^{\mu\nu} p_{W\nu}(g_L P_L + g_R P_R) b W_{\mu} + \text{ Hermite conjugate}\end{aligned} \tag{1.13}$$

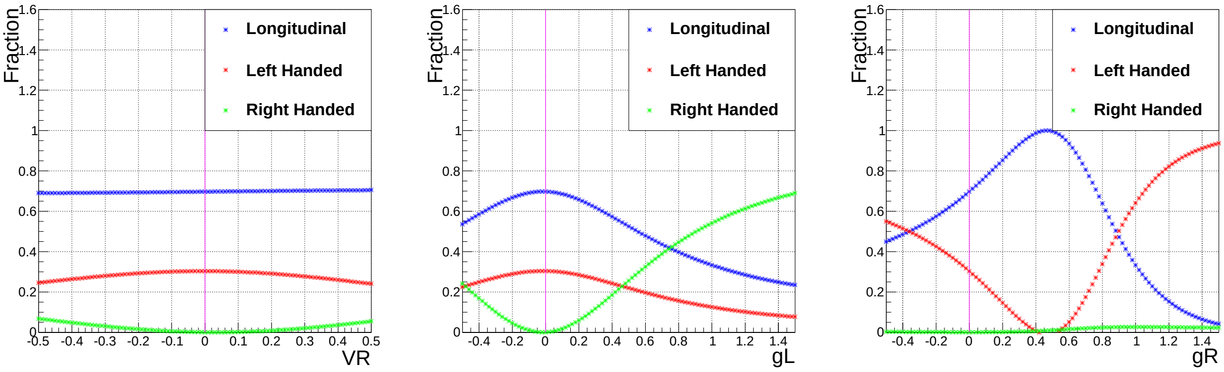

Figure 1.8: V_R(left), g_L(middle), g_L(right) dependence of the W boson polarization fraction. The vertical line shows the nominal value. In these, $m_t = 172$ GeV, $m_W = 80.4$ GeV$m_b = 4.2$ GeV, $V_L = 1, V_R = g_L = g_R = 0$ are assumed.

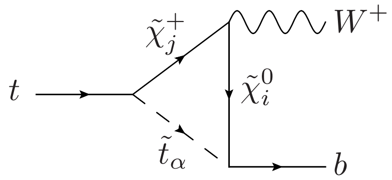

Figure 1.9: An example diagram that contribute to the top quark decay vertex in the Minimal Supersymmetric Standard Model.

where $P_L = \frac{1}{2}(1 - \gamma^5)$ and $P_R = \frac{1}{2}(1 + \gamma^5)$, $V_{L,R}$ and $g_{L,R}$ are parameters. The four terms represent the decays from a top quark to a bottom quark with each chirality :

- $V_L : t_L \to b_L$
- $V_R : t_R \to b_R$
- $g_L : t_L \to b_R$
- $g_R : t_R \to b_L$

Setting $V_L = 1$ and $V_R = g_L = g_R = 0$, it is identical to the SM Lagrangian, equation (1.2) (in the limit of $V_{tb} \to 1, V_{ts}, V_{td} \to 0$). The combinations of the parameters in which only one of them is no-zero and the derived W boson polarization from the combinations are

- $(V_L, V_R, g_L, g_R) = (0, 1, 0, 0) \to (F_0, F_L, F_R) = (0.70, 0.00, 0.30)$
- $(V_L, V_R, g_L, g_R) = (0, 0, 1, 0) \to (F_0, F_L, F_R) = (0.10, 0.01, 0.90)$
- $(V_L, V_R, g_L, g_R) = (0, 0, 0, 1) \to (F_0, F_L, F_R) = (0.10, 0.90, 0.01)$

in the tree level calculation with $m_t = 172.5, m_W = 80.4, m_b = 4.2$ GeV. Figure 1.8 shows how the fractions evolve as the parameters V_R, g_L, g_R increase/decrease, based on the calculation in [10].

In case some new particles that contribute to the top quark decay exist, deviation of the effective Lagrangian parameter $\{V_L, V_R, g_L, g_R\}$ from the values of the SM can be seen. Figure 1.9 shows one example in the Minimal Supersymmetric Standard Model, and the deviation of the parameter can be 0.05 % in $\mathrm{Re}(g_R)$ [11]. By measuring the parameter of the effective Lagrangian, new physics search in a model-independent way is possible.

Chapter 2

The LHC-ATLAS experiment

2.1 The LHC accelerator

The Large Hadron Collider (LHC) collides protons with 7 TeV center of mass energy, which provides enough energy to provide top quark pair production with large statistics.

The LHC complex consists of a pre-injector complex and the LHC main rings as Figure 2.1 shows. The LINAC2 is a duoplasmatron and produces ionized protons (H^+) from hydrogen gas, and boost them to 50 MeV. The produced proton beam is accelerated by the Booster, Proton Synchrotron(PS) and Super Proton Synchrotron(SPS) to 1.4, 25 and 450 GeV step-by-step. The two LHC rings are for protons turning around clockwise and counter-clockwise. The rings has a radio frequency (RF) of a 400MHz superconductivity cavity system for beam acceleration up to 3.5 TeV(in 2011 run. In designed, 7 TeV.), and 1232 di-pole superconductivity magnets with 8.33T magnetic field for beam circulation. In the protons collisions with 7 TeV center of mass energy, the top quark pair production cross section is $164.6^{+11.4}_{-15.7}$ pb (the top quark pair) which is more than twenty times larger than that in the Tevatron accelerator($\sim$ 7pb, the top quark pair). There are four interaction points and one of them is for the ATLAS experiment.

The LHC is designed to receive bunches from SPS and put them in every ten “buckets”(=40MHz) and the LHC has 3546 “bunch spaces”. The bunch spaces are not fully filled due to its injection scheme. The LHC rings are filled by twelve injections of the SPS, and the SPS is filled by three to four injections by the PS. There is a dead time in these injection, due to rising time of bunch kicker magnet. Also, some bunch spaces in the LHC ring are need to be kept empty for rising time of dump kicker magnet. Figure 2.2 shows the rising time of the LHC kicker magnet that takes $< 3\mu$s to be stabilized. These facts determine the maximum filling pattern of the LHC as Figure 2.3 shows. In the 2011 run, 1380 bunches are filled in each ring, that is the half of the maximum filling scheme, and collisions are occurred every 50 ns.

High instantaneous luminosity L is essential for high statistics data. The number of events of a particular process N_{event} is proportional to its cross section σ_{event} and the integrated luminosity :

$$N_{\mathrm{event}} = \sigma_{\mathrm{event}} \int \mathrm{d}tL. \tag{2.1}$$

The instantaneous luminosity can be described as

$$L = \frac{n_1 n_2 n_b f_{\text{rev}} \gamma}{2\pi \sigma^* \beta^*} F \tag{2.2}$$

where n_1, n_2 are the number of protons in a group of protons called a bunch in each ring, σ^* is normalized emittance of the beams and γ is the Lorentz factor. The parameter β^* and σ^* describe how small the beams are at the interaction point. n_b is the number of the colliding bunch pairs, and f_{rev} is the machine revolution frequency (~11kHz). F stands for geometric luminosity reduction due to collision with non-zero crossing angle of the beams (120 μrad). Concerning these parameters, there are experimental limits. One of them is the *beam-beam limit* that collisions with parameter ξ larger than 0.015 is not stable, where the parameter ξ is defined as

$$\xi = \frac{n_b r_p}{4\pi \sigma^*} N_{IP} \tag{2.3}$$

where r_p is the classical proton radius, N_{IP} is the number of interaction point of the accelerator. For σ^* which is a typical geometrical limit of the emittance in the LHC, the limit on the number of protons in one bunch is 1.15×10^{11}. In the run in 2011, the maximum number of protons in one bunch is 1.49×10^{11}, and minimum emittance is 2.6 μm. The maximum peak luminosity reached at 3.6×10^{33} cm^{-2}s^{-1}.

In addition to the instantaneous luminosity, life time τ of beam is also important for studies with high statistics. The number of protons in the beams decrease due to collisions (τ_{nucl} = 44.85 h), scattering in the beam (intra-beam scattering, τ_{IBS} = 100 h) and collisions with gas in the rings (τ_{gas} = 80 h). In total, typical life time (the time required to reach $1/e$ of the initial luminosity) is about 15 hours.

More detail about the LHC machine can be found in [12].

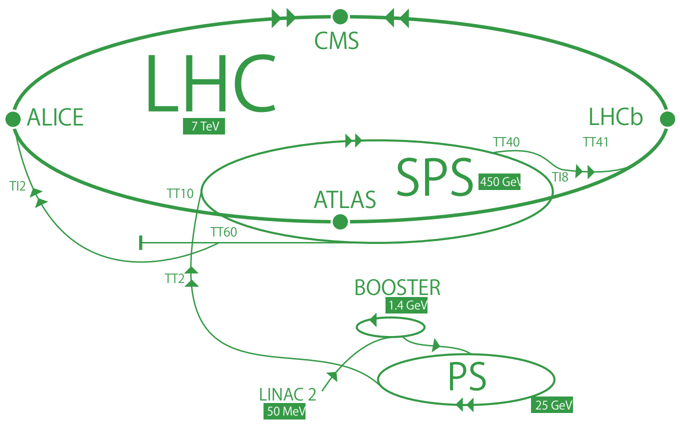

Figure 2.1: An illustration of the LHC complex that consists of LINAC2, Booster, PS, SPS and main LHC rings.

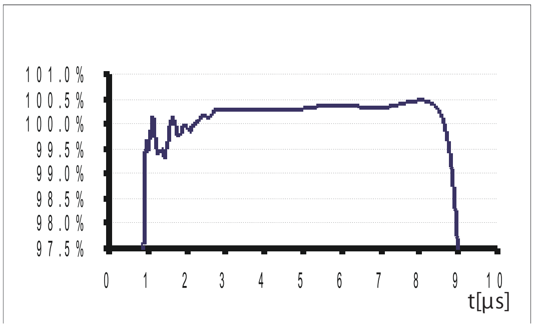

Figure 2.2: The current pulse shape of the LHC kicker(prototype). It takes $< 3\mu$s to be stabilized. The LHC filling scheme must have a margin to wait the kicker become fully operated.

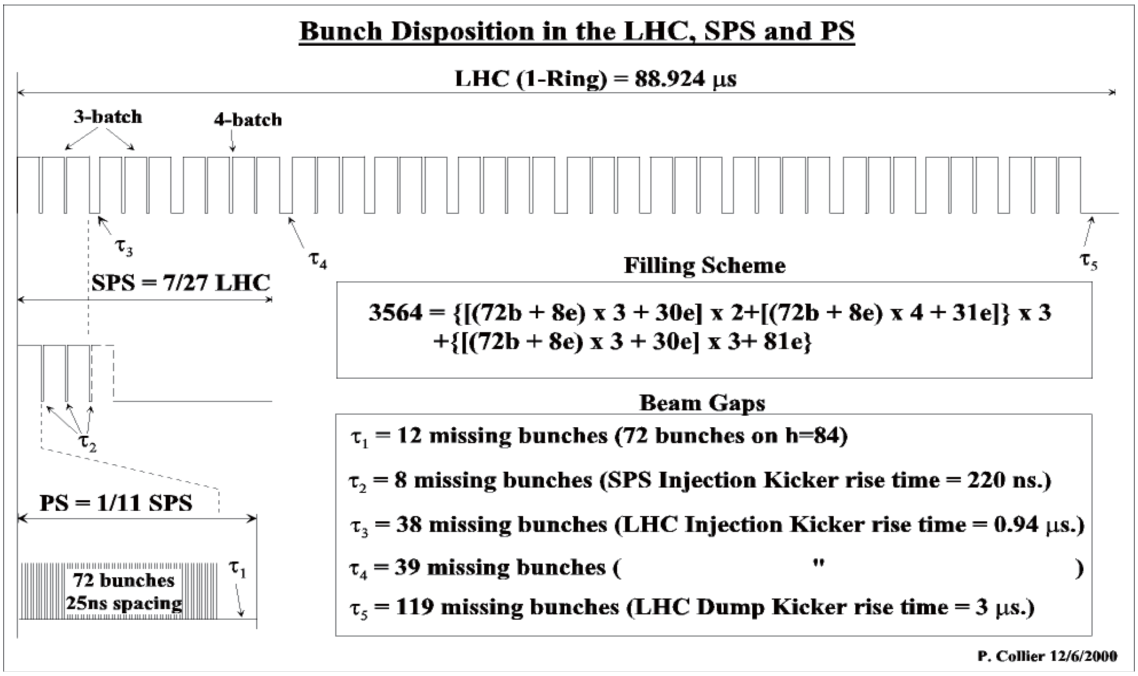

Figure 2.3: LHC maximum fill pattern. The LHC is filled by the SPS, and the SPS is by PS. In the scheme, dead time due to kicker magnet rising time must be taken into account, and as the results, filling pattern has several groups of bunches, so-called *bunch trains*.

2.2 The ATLAS detector

The proton-proton collision events brought by the LHC are observed by the ATLAS detector. The components of the detector are roughly categorized into an inner detector, calorimeters and a muon spectrometer, as Figure 2.4 shows.

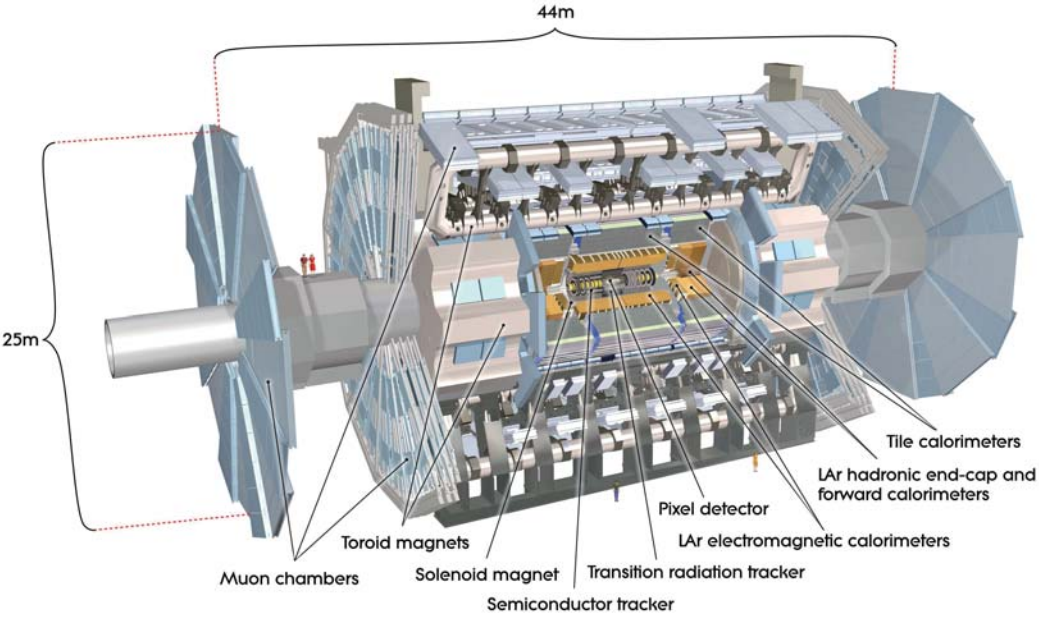

Figure 2.4: The ATLAS detector that consists of an inner detector, calorimeters and a muon spectrometer. Also solenoid and toroidal magnets are implemented.

The inner detector is allocated in the most inner part of the ATLAS detector, and installed in a magnetic field of 2 T. It measures momenta of charged tracks from their curvature. Also transition radiation detector is implemented for electron-pion separation. More detail of the inner detector is described in section 2.2.1.

In order to measure energy of particles, electromagnetic and hadronic calorimeters are implemented surrounding the inner detector. Electrons are reconstructed from the energy deposits especially on the electromagnetic calorimeter, associated with reconstructed tracks in the inner detector. High energy quarks and gluons emerged in hard scattering make directional particle flows, so-called *jets*, which are reconstructed from energy deposits on the calorimeters. The calorimeters are summarized in section 2.2.2.

High energy muons can penetrate the calorimeters just loosing energy of ~3 GeV and reach at the muon spectrometer outside of the calorimeter. The muon spectrometer measures the muon momenta from their curvature in toroidal magnetic field. More detail of the muon spectrometer is described in the section 2.2.3.

In the ATLAS detector, the axes of coordinate are taken as following. The origin is the center of the detector, interaction point. The z axis is defined along the beam direction and take the direction of counter-clockwise beam to be positive. The x and y is defined on the transverse plane of the z axis,

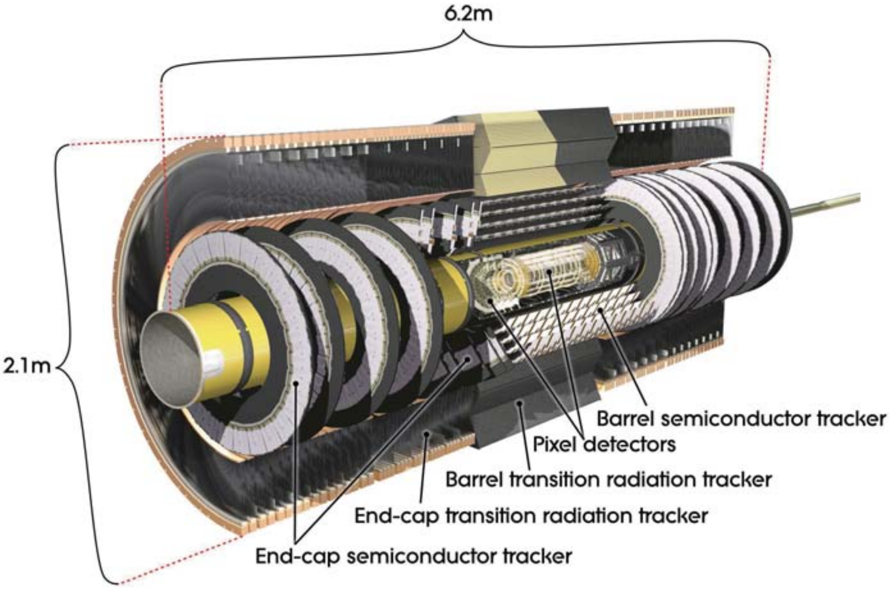

Figure 2.5: A cut-away figure of the ATLAS inner detector

and x towards the center of the LHC ring, and y upward. Angle ϕ is defined on the transverse place as $\phi = \arctan(y/x)$ and azimuth angle θ is defined with respect to z axis. In the analysis pseudo-rapidity $\eta \equiv -\ln(\tan(\theta/2))$ is often used.

2.2.1 Inner Detector

The inner detector consists of three types detector : Pixel detector, SemiConductor Tracker(SCT) and Transition Radiation Tracker(TRT). The first two and TRT cover $|\eta| < 2.5$ and $|\eta| < 2.0$ respectively. Figure 2.5 and Figure 2.6 are the cut-away figure and the cross section of the inner detector, respectively. All of them has two types : barrel and end-cap. They implemented in the 2T magnetic field in the direction z by a solenoid magnet, and measure the charged track momentum and charge by detecting their bending trajectory with space-points. Table 2.1 summarizes the precision of the detectors. The Pixel and SCT provides high precision measurement while TRT provides electron/hadron separation by detection of transition radiation, which are discussed in the following sections respectively.

Pixel detector

The Pixel detector are composed by 1744 modules. Figure 2.7 shows one module, which consists of sensor with $6.08\times1.64\text{cm}^2$ active region and control electronics. The “FrontEnd(FE)” are connected to the sensor with the bump bonding, that also connect them electronically. The sensor module is an array of bipolar diodes consist of 250μm thick n-bulk. It has 144 columns × 328 rows = 47232 pixels, 90% of them are $382.5\times30\mu\text{m}^2$ and left $582.5\times30\mu\text{m}^2$. Typical operating high voltage is 150V and can be increased up to 600V against degradation due to long operation. More information can be found in [13].

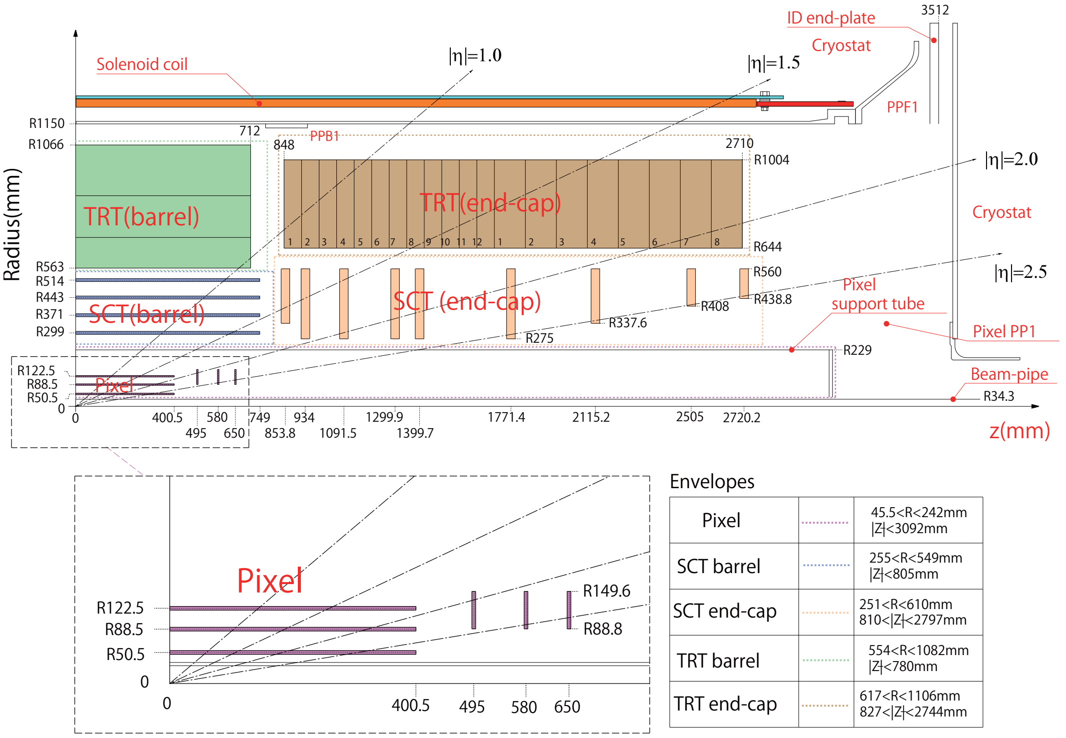

Envelopes		
Pixel	┈	45.5<R<242mm |Z|<3092mm
SCT barrel	┈	255<R<549mm |Z|<805mm
SCT end-cap	┈	251<R<610mm 810<|Z|<2797mm
TRT barrel	┈	554<R<1082mm |Z|<780mm
TRT end-cap	┈	617<R<1106mm 827<|Z|<2744mm

Figure 2.6: Cross section of the ATLAS inner detector

SemiConductor Tracker(SCT)

The SCT uses micro-strip of n-in-p semiconductor of 80 μm pitch, thickness of 285μm. The nominal operation voltage is 480V. As Figure 2.8 shows, one module consists of two sensors with rotated +20 μrad and -20 μrad around their geometrical center, so that the module has sensitivity to the direction of the strips. The resolution of the detector is 17 μm in R-ϕ direction and 580 μm in z direction. More detail is found in [14].

Transition Radiation Tracker(TRT)

TRT is a drift tube tracker with transition radiator, and, in addition to the measurement of charged particle trajectory, it also performs electron/hadron separation by detecting extra energy deposit due to transition radiation of electron.

The drift tube tracker consists of a straw of 4mm diameter and 31μm diameter tungsten wire plated with 0.5-0.7mm gold. In the tube, mixture gas of Xe:CO$_2$:O$_2$=70:27:3 is filled, and gain of the primary electron in the ionization of charged particles is 2.5$\times$10^4 with cathode operation at -1530V.

As the transition radiator, polypropylene is used. In the endcap, 15μm thick polypropylene foils are allocated between radially aligned drift tube layers, as Figure 2.9(left). In the barrel, the tubes are embedded in a mat of 19μm-diameter polypropylene as Figure 2.9(right) shows.

The energy emission I of a particle with electric charge of ez (e is elementary electric charge) at

Pixel	
end-cap	10(R-ϕ), 115(z)
barrel	10(R-ϕ), 115(R)
SCT	
barrel	17(R-ϕ), 580(z)
end-cap	17(R-ϕ), 580(R)
TRT	
	130

Table 2.1: The intrinsic accuracy(μm) of the ATLAS inner detectors.

the boundary of a medium and vacuum is [1]

$$I = \alpha z^2 \gamma \hbar \omega_p / 3 \tag{2.4}$$

where α is the fine structure constant, γ is the Lorentz factor of the particle, $\hbar$ is the Planck constant and ω_P is the plasma frequency of the medium. Here, $\hbar\omega_P = \sqrt{\rho(\text{in g/cm}^3)\langle Z/A \rangle} \times 28.81$ eV and $\hbar\omega_P \sim 20$ eV for styrene. Due to its Lorentz factor dependence, the probability of transition radiation emission of electrons is larger than that of hadrons with the same momentum. In order to detecting the transition radiation, the TRT readout has two thresholds. The lower one is aiming at measurement of drift time for tracking, and the higher is used for transition radiation. The time that the signal excess the threshold is counted in the interval of 3ns and it is used in the electron identification, which is discussed in section 2.4.2.

2.2.2 Calorimeter

Outside of the inner detector, electromagnetic and hadronic calorimeters are installed. Figure 2.10 is cut-away figure of the ATLAS calorimeters. In total, region up to $|\eta| < 4.9$ is covered, which provides good resolution of missing E_T. Figure 2.11 and 2.12 shows the radiation length of the electromagnetic calorimeter and interaction length of the hadron calorimeter, respectively. The electromagnetic calorimeter provides more than 22 and 24 radiation length in the barrel and endcap regions. The hadron calorimeter has about 10 interaction length, which is adequate for energy measurements and prevention of punch through of hadrons.

Electromagnetic LAr Calorimeter and pre-sampler

The calorimeter consists of 2.2mm thick lead absorber and LAr is filled between the gaps, in the barrel part that covers region $|\eta| < 1.475$ and in the endcap of $1.375 < |\eta| < 3.2$. The absorber is accordion shape as Figure 2.13. Thanks to this design, the amount of absorber and support structure is almost uniform in ϕ, and the detector performance is also uniform. The gap between the lead plates is 2.1mm in the barrel and 0.9-3.1mm in the end-cap. Electrodes for readout and high-voltage supply are implemented with flexible large size printed boards and are allocated in the center of the gaps supported by honeycomb spacers. The board consists of three thin copper layers insulated by

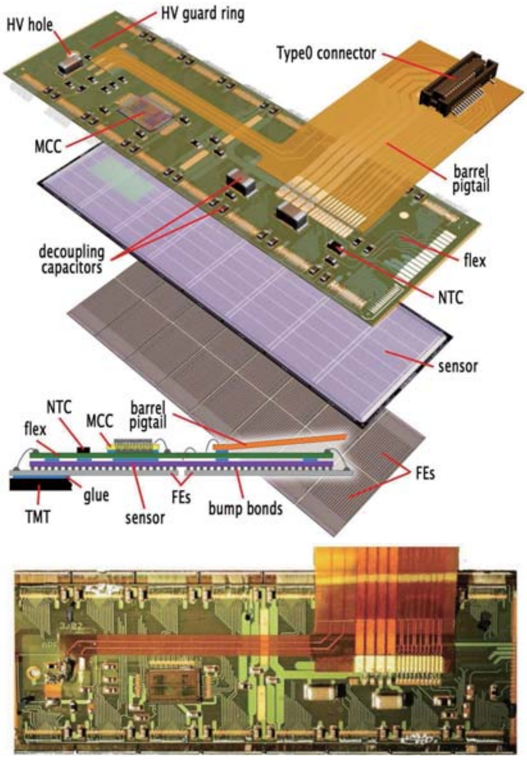

Figure 2.7: An illustration and picture of one module of the Pixel detector

polymide. The two outer layers are for high voltage with typical operating voltage of 2kV for the barrel and 0.9-2.5kV in the end-cap. The signals are readout from the middle layers via capacitive coupling.

The ϕ division of the calorimeter readout block is achieved by ganging several electrodes, while that in η and depth separation are done by etching of the copper layers of the electrodes. More detail of the electromagnetic LAr calorimeter is in [15](barrel) and [16](end-cap), and in [17] specially for the electrode.

In region up to $|\eta| < 1.8$, another LAr calorimeter, so-called *pre-sampler*, is implemented in front of the accordion calorimeter. It aims at correcting energy deposits due to materials in front of the calorimeter which is shown in Figure 2.14. The depth of the LAr in the pre-sampler is 11mm in the barrel and 4mm (2mm×2) in the end-cap. More detail is in [18].

The LAr readout hardware had a trouble during the data taking. In 84% of the total integrated luminosity used in this analysis is affected. Three front-end electronic boards have broken and information from the region $\eta = [0, 1.4]$, $\phi = [-0.8, 0.6]$ were not read out. The malfunction results in ill-reconstruction of jets and electrons. In the Monte Carlo simulation, the malfunction not implemented. In order to make the same situation in the data and simulation, special treatments are done in the region. The details are described in section 2.4.2(electron reconstruction) and section 2.4.5(jet reconstruction).

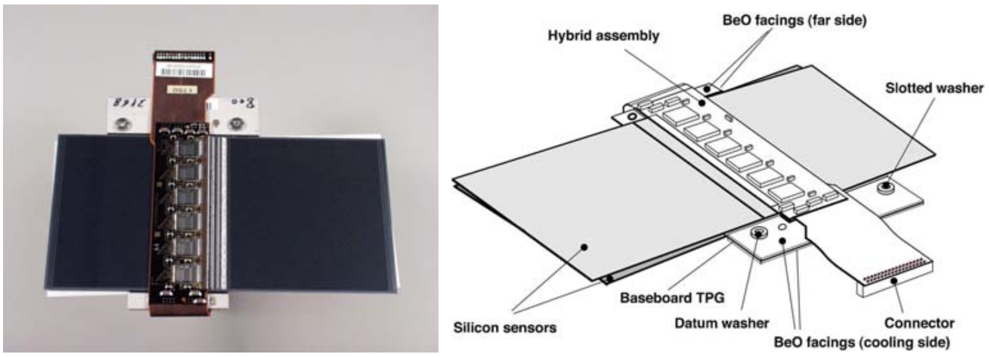

Figure 2.8: A illustration and picture of one module of the SCT detector

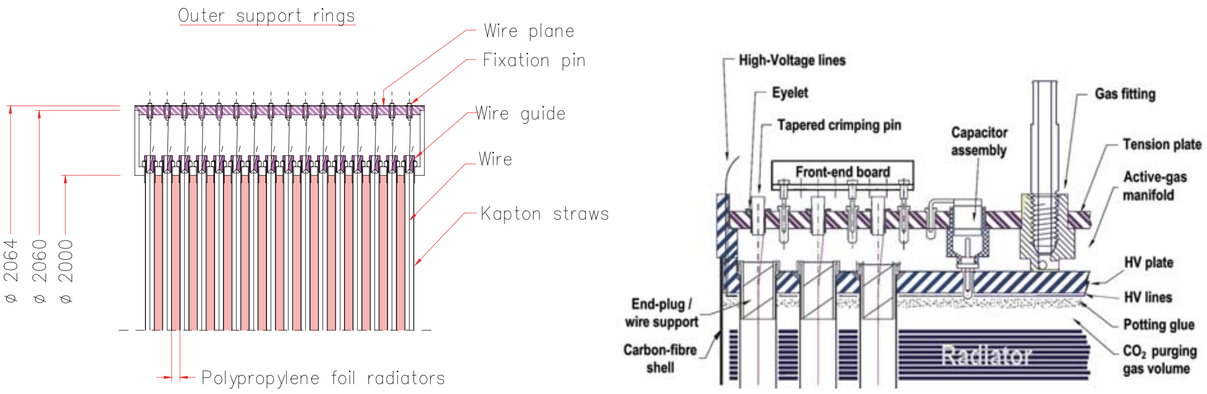

Figure 2.9: The structure of the TRT detector, for barrel (left) and end-cap (right).

Hadron tile calorimeter

The Hadron tile calorimeter covers region $|\eta| < 1.7$. It is a sampling calorimeter with steal as the absorber and scintillator as the active medium with ratio by volume of 4.7:1, stacked as Figure 2.15 shows. The signal light is measured by photo multiplier via wave length shift fibers from both side of each scintillator tile. Three dimensional cell structure is achieved by grouping the fibers. The grouping in depth is 15, 4.1 and 1.8 interaction length and granularity in $\delta\eta \times \delta\phi$ is 0.1×0.1 in the first two layers and 0.1×0.2 in the last, as Figure 2.16 shows. Between the barrel and extended barrel region, extra scintillators are implemented which are also drawn in this figure .

Hadron endcap LAr calorimeter

It covers region $1.5 < |\eta| < 3.2$. It is a sampling calorimeter with copper absorber and LAr active medium. Figure 2.17 shows its schematic view. The front wheel consists of 24 copper plates with 25mm thick with one 12.5mm front plate, and the rear consists of 16 plates with 50mm with one 25mm thick front plate. The gaps of the plate filled with LAr are all 8.5mm. Three electrodes are inserted between them dividing the space into 1.8mm×4 as Figure 2.18 shows. The outer two electrodes are for high voltage, with nominal voltage of 1800V resulting in 430ns drift time. The

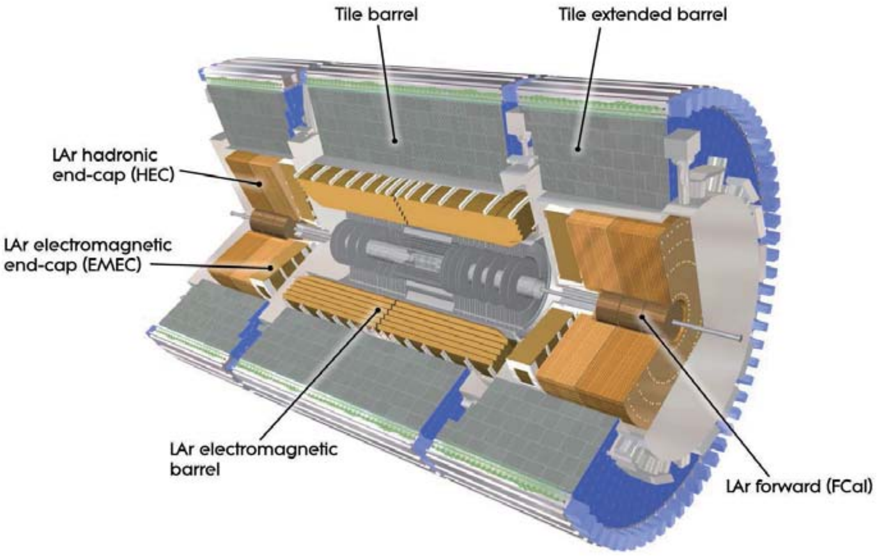

Figure 2.10: A cut-away figure of the ATLAS calorimeter detector

middle one is for read out defining lateral segmentation by etching the electrode(as is done in the electromagnetic LAr calorimeter). The granularity of $\delta\eta \times \delta\phi$ is 0.1×0.1 in $|\eta| < 2.5$ and 0.1×0.2 in $|\eta| > 2.5$.

LAr forward calorimeter

The calorimeter covers $3.1 < |\eta| < 4.9$ and consists of three wheels : the first (inner) works as electromagnetic calorimeter with copper absorber and the last two as hadron calorimeter with tungsten absorber. They use LAr as the active medium. Figure 2.19 shows $x - y$ cross section of the calorimeter(the most inner one). The electrodes are inserted into holes that are oriented parallel to the beam direction. The length of typical gap, filled by LAr, is about 2 mm.

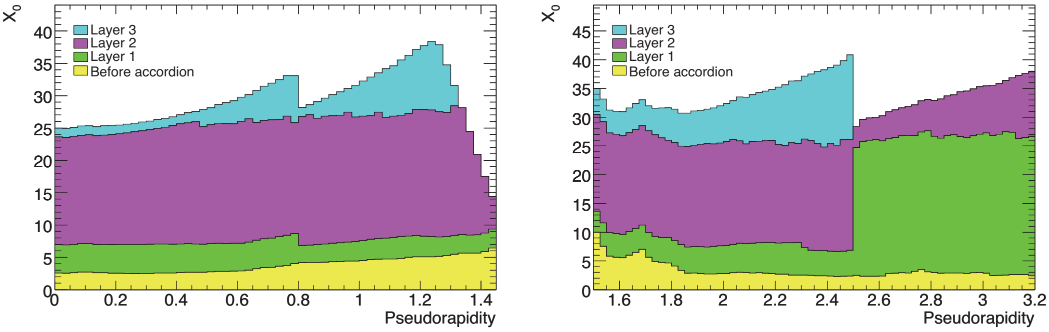

Figure 2.11: Radiation length before the EM calorimeter and in each calorimeter layer

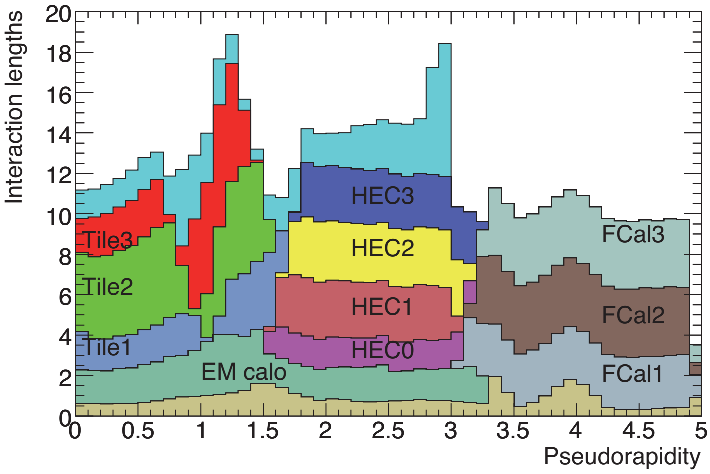

Figure 2.12: Interaction length before calorimeter and in each layers.

Calorimeter signal readout

The calorimeter signal is fed into pre-amplifier and shaper. Figure 2.20 shows an example, of the signal shape in the electromagnetic LAr calorimeter detector after the shaper with respect to a rectangular input, indicating also sampling intervals of 25ns. In the nominal operation, five points sampling is used.

One of important tasks of the readout electronics is optimal filtering of input signal in order to determine energy deposit and timing for each cell. The method fits the normalized nominal signal shape to the input signal with a χ^2 minimization. The fitting quality is also used to reject fake signals in the jet reconstruction, as described in section 2.4.5. More detail about the filter is found in [19].

On the readout electronics, the level 1 trigger decision is implemented, which is also discussed related to the electron trigger, in section 2.5.1.

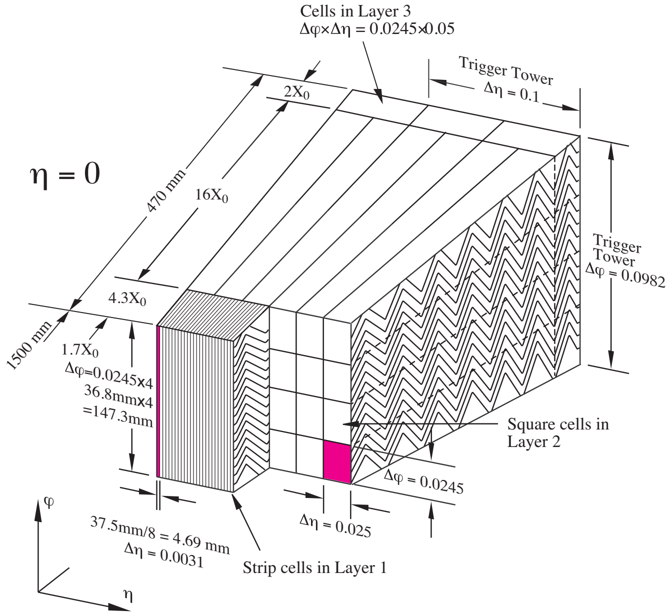

Figure 2.13: A illustration of the barrel electromagnetic LAr calorimeter.

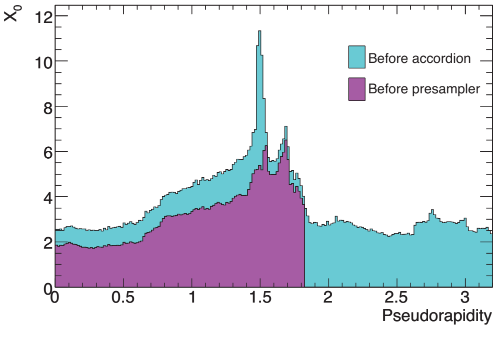

Figure 2.14: The radiation length before the pre-sampler.

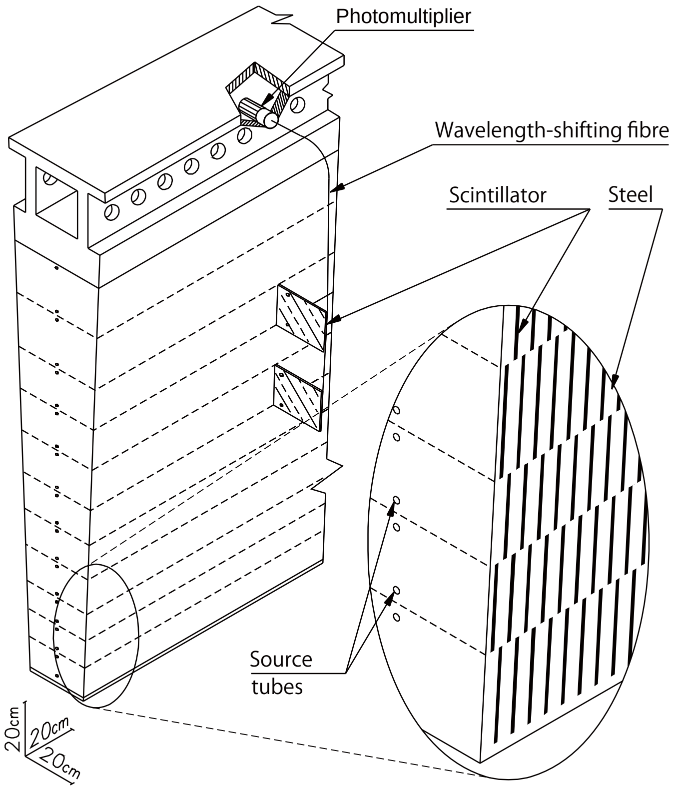

Figure 2.15: An illustration of one module of the Tile calorimeter.

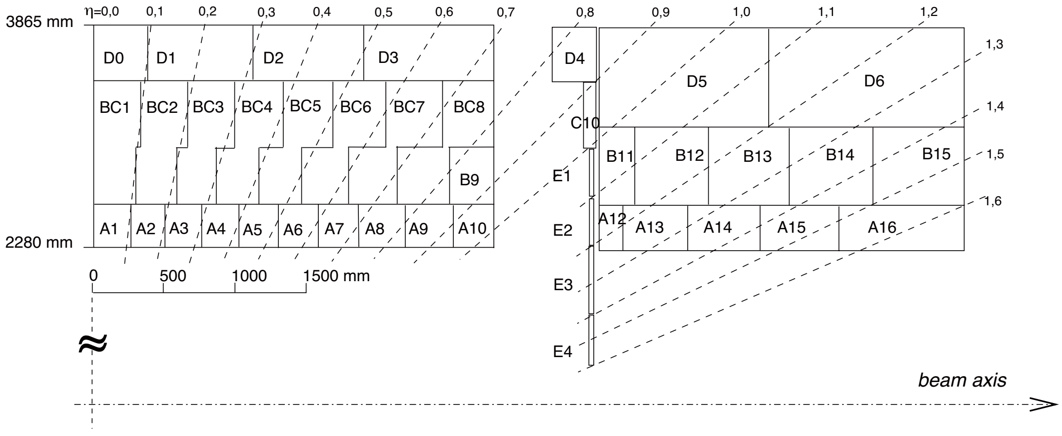

Figure 2.16: An illustration of the Tile calorimeter segmentation in η and depth direction.

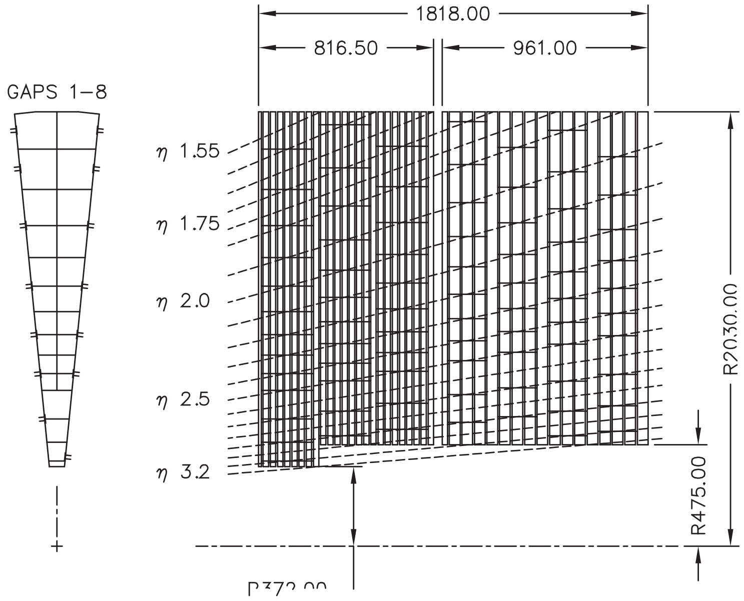

Figure 2.17: An illustration of LAr hadron calorimeter and its segmentation of the readout.

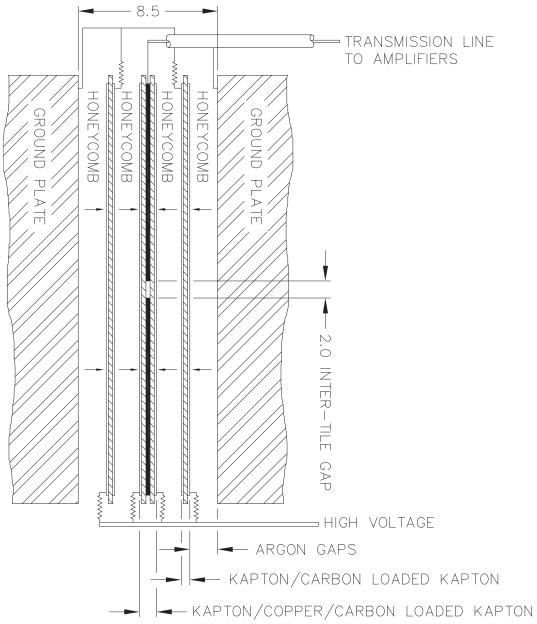

Figure 2.18: The structure of the LAr forward calorimeter.

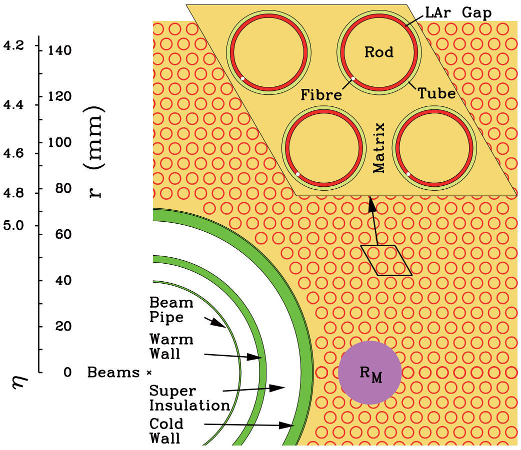

Figure 2.19: The cross section of the LAr forward calorimeter. The circle of R_M shows the size of Moliere radius.

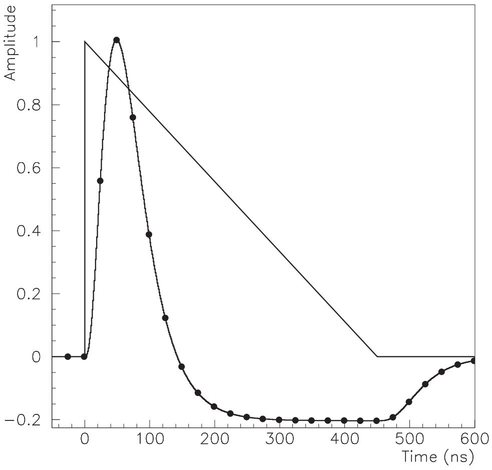

Figure 2.20: An example of the signal shape in the electromagnetic LAr calorimeter.

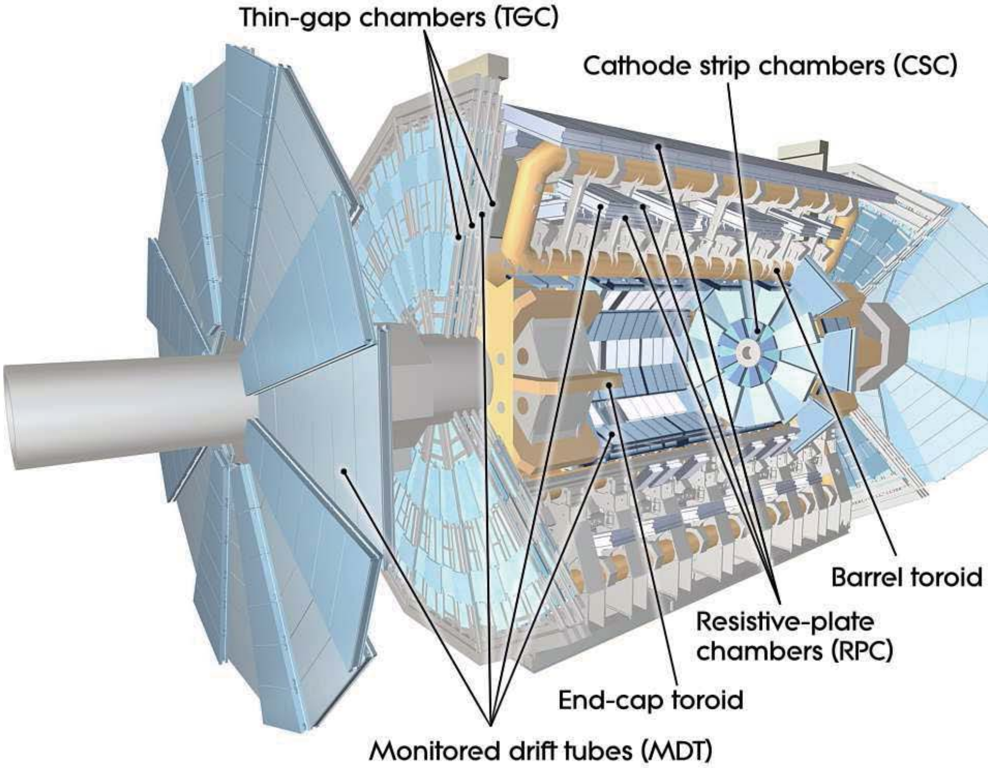

Figure 2.21: A cut-away of the muon spectrometer.

2.2.3 Muon Spectrometer

The ATLAS muon spectrometer consists of chambers for the level 1 trigger decision(the TGC and RPC) and that for precise tracking(the MDT and CSC). Both detector measures muon momentum by reconstruct tracks bent by the toroidal magnetic field. Figure 2.21 shows cut-away figure of the muon spectrometer.

Thin Gap Chambers(TGC)

The detector is one of the trigger detector, and covers the region $1.05 < |\eta| < 2.4$(for readout it covers up to $|\eta| = 2.7$). The detector is described in section 3.1.1 in more detail.

Resistive Plate Chambers(RPC)

The trigger detector covers region $|\eta| < 1.05$. It performs level 1 trigger decision by detecting muons with three stations of the RPC detectors allocated as shown in Figure 2.22. The scheme and hardware implementation of the logic is similar to that of the TGC.

The chamber is a gaseous parallel electrode-plates detector. Two resistive plates of phenolic-melaminic are allocated with 2mm gaps by spacers. The gap is filled with mixture gas of $C_2H_2F_2$, Iso-C_4 H_{10} and SF_6 = 94.7:5:0.3. Between the gap, high voltage of 4.9kV/mm is applied, and primary

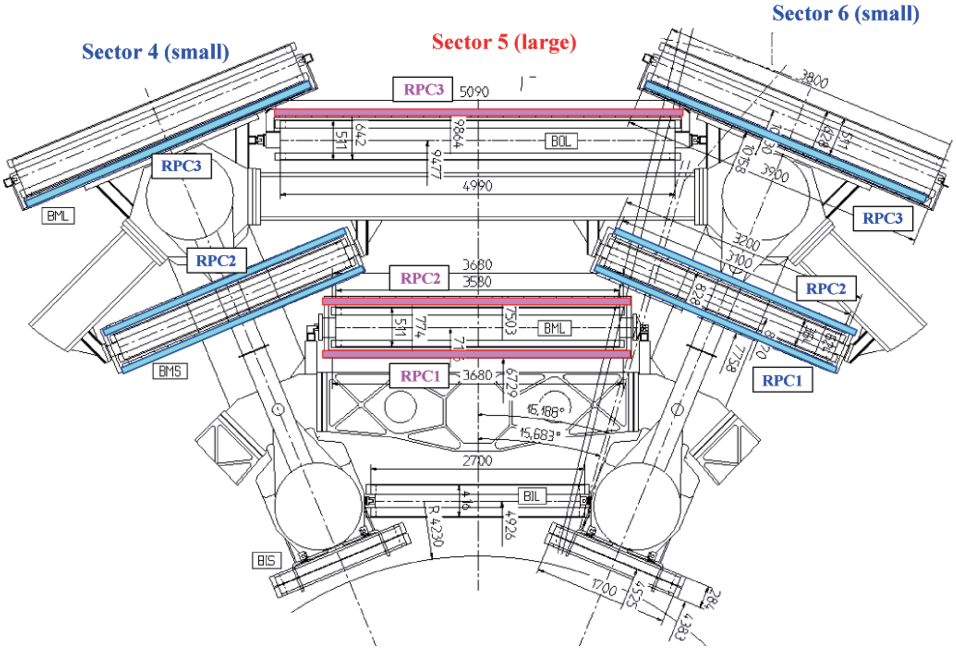

Figure 2.22: The allocation of the RPC chambers.

electrons due to charged particles make avalanche. The signal is read out through capacitive coupling strips with pitch of 23-35mm, as Figure 2.23.

Monitored Drift Tube detector(MDT)

The detector is drift tube chambers with 30mm diameter tubes filled with Ar:CO_2=93:7 gas of 3 bar, and wires of 50 μm tungsten-rhenium with nominal operating voltage of 3080V. Figure 2.24(left) shows the drift time as a function of the most approaching point of tracks. Figure 2.24(right) shows the precision of the measurement. Although the resolution is worsen as the irradiation rate increase, it has track resolution better than 100 μm for tracks of r > 5mm even in the expected worse case of 150Hz/cm^2.

The tubes are stacked into layers, typically 6 or 8 layers, and form one chamber. The chambers are allocated mainly three stations in barrel and end-cap. All the chambers are allocated so that they has sensitivity in $R(\eta)$ of the tracks. The ϕ information of the tracks are given by the trigger chambers as described in muon reconstruction in section 2.4.3.

Cathode Strip Chambers(CSC)

The detector is allocated in 2< $|\eta|$ < 2.7 of the most inner muon station, where the track count rate is highest ~ 150Hz/cm^2. It consists of four layers of multi-wire proportional chambers with a node wires of 2.5mm pitch and two dimensional(η and ϕ) readout strips. The distance between wire and strips is 2.5mm. With mixture of gas Ar:CO_2=80:20 and nominal operation voltage with 1900V,

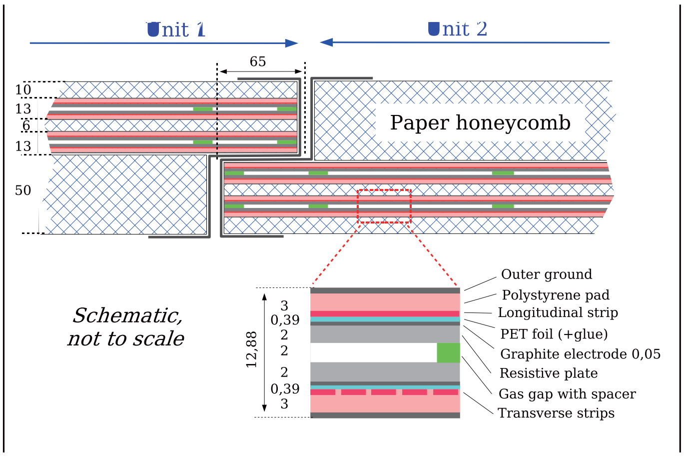

Figure 2.23: The RPC chamber structure.

typical gain is 6×10^4. The pitch of the strip is 5.6mm (5.3mm) in η direction and 13mm(21mm) in ϕ direction in a smaller(larger) type chamber.

The chamber determines the track position with precision of 60 μm by reconstructing the charge distribution as Figure 2.26 from multiple readout channels and find the center. Also correlation of the signal heights in η and ϕ readout is utilized.

2.2.4 Solenoid and toroid magnets

The ATLAS detector has a solenoid and toroidal superconductivity magnets for charged particle momentum measurement.

One Solenoid magnet is aligned so that it produce magnetic field of 2T in z direction for the particle momentum measurement in the inner detector. Figure 2.27 shows the magnetic field strength in z and r direction by the magnet.

One barrel solenoid makes magnetic field up to $|\eta| \sim 1.5$ and two endcap magnets cover the regions beyond. These toroidal magnets are in eight-fold symmetry, and so is the magnetic field. Figure 2.28 shows the field strength by the toroidal magnets in $\phi = 0$ and $\pi/8$. The region $\eta \sim 1.5$ corresponds to a gap between the barrel and end-cap magnets.

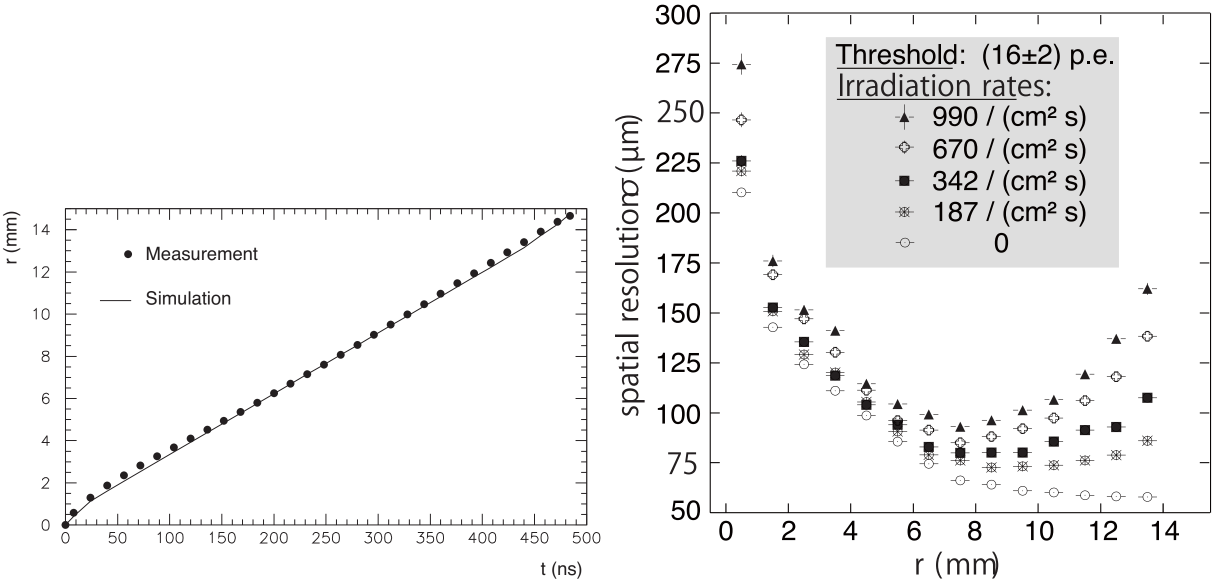

Figure 2.24: (left)The MDT drift time. (right)The precision of the MDT.

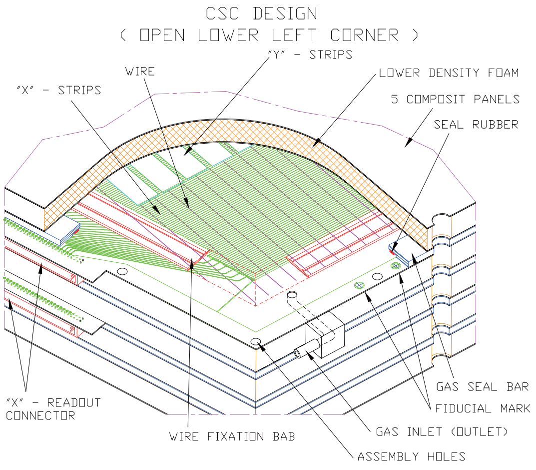

Figure 2.25: The structure of the CSC detector. “x”-strip is the one that is sensitive to η and “y” is to ϕ.

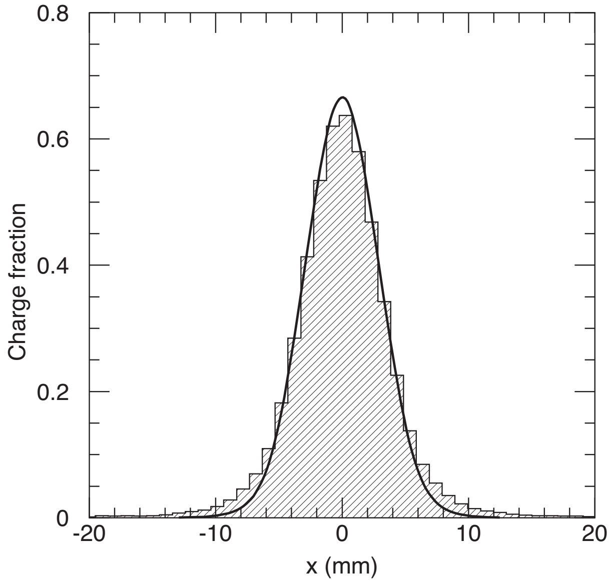

Figure 2.26: The charge distribution in the CSC detector.

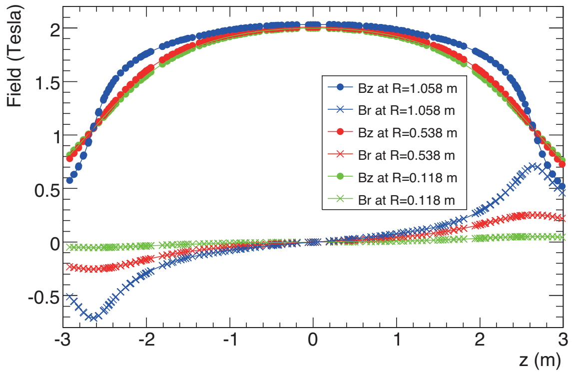

Figure 2.27: (left) The magnetic field strength induced by the solenoid magnet.

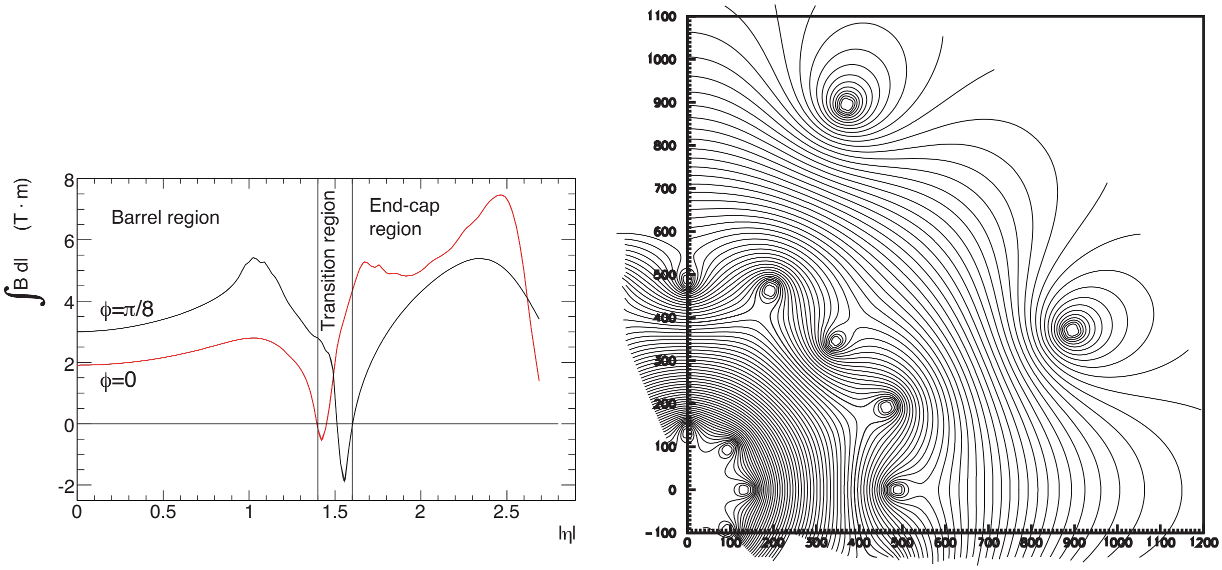

Figure 2.28: Magnetic field by toroidal magnet. (left)The integral magnetic field strength induced by the toroidal magnets. The dip around $\eta = 1.5$ corresponds to the gap between barrel and end-cap magnets. (right) Magnetic field strength around the transition region.

2.3 Monte Carlo simulation and computer modeling of the ATLAS detector

Computer simulation of the ATLAS detector is used in order to understand the detector performance and behavior of physics processes in the detector.

In order to calculate the final states in the proton-proton collisions, it is needed to defined the initial states, that is, the composition of protons. The composition is not only two up quarks and one down quark, called *valence* quarks, but also gluons and other quarks, called *sea* quarks, which carry relatively small fractions of energy of protons. And in the collisions of protons with the center of mass energy of 7 TeV, the collision is needed to be described as the collision of quarks and gluons, called *partons*. Parton distribution function (PDF) describes the possibility of quarks and gluons to bring a fraction x out of the total energy of proton. Here, x is [0,1]. Figure 2.29 shows an example of parton distribution function. CTEQ66, one of the PDF set, describes the distributions of $u_v = u - \bar{u}$, $d_v = d - \bar{d}$, $\bar{u} + \bar{d}$, $\bar{d}/\bar{u}$, g and $s = (\bar{s})$ at a certain energy scale Q_0 in the following formats [5] [20] [21] :

$$xf(x, Q_0) = A_0 x^{A_1}(1-x)^{A_2} e^{A_3 x}(1 + e^{A_4} x)^{A_5} \qquad (u_v, d_v, \bar{u} + \bar{d}, g) \tag{2.5}$$

$$xf(x, Q_0) = A_0 x^{x_1}(1-x)^{A_2} + (1 + A_3 x)(1 - x^{A_4}) \qquad (\bar{d}/\bar{u}) \tag{2.6}$$

$$xf(x, Q_0) = A_0 x^{A_1}(1-x)^{A_2} P(x) \qquad (s = \bar{s}) \tag{2.7}$$

where A_i are parameters for each parton, and $P(x)$ is some smooth function [21]. The parameters are determined by fitting theoretical expectation based on the PDF to data of deep inelastic scattering experiments. It is performed in the diagonalized space with respect to correlated uncertainties of the parameters, and assuming some constraints. Eventually, fitting are done with 22 degrees of freedom, and CTEQ66 gives the center value and $22 \times 2 = 44$ sets for uncertainties of each parameter up and down.

A Monte Carlo generator(MC generator) gives one final state based on the matrix element calculation with a given initial state according to the PDF. And hadronization of quarks such as a b-quark

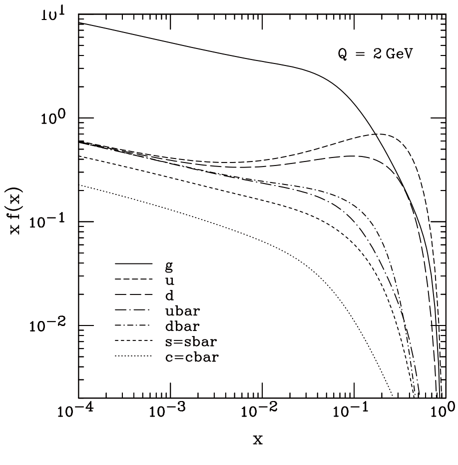

Figure 2.29: An example of parton distribution function at $Q = 2$ GeV (calculation of CTEQ6M [5]).

from a top quark decay are emulated based on a parton shower model. Table 2.2 summarize the generators and parton showers used in this analysis.

Process	Generator, Parton shower
$t\bar{t}$	NC@NLO + HERWIG v6.510
Z+jets	ALPGEN + HERWIG/Jimmy
di-boson	ALPGEN + HERWIG
top quark with W boson	MC@NLO + Herwig/Jimmy

Table 2.2: The summary of Monte Carlo generator used in this analysis.

These calculations from the initial state to the final state with hadronization are performed step-by-step and are recorded so that the chain is fully traceable. This means, in the Monte Carlo simulation, *truth* information of particles as of production at the interaction point can be compared to information reconstructed by the detector.

The emulated interaction is passed to detector simulation by the GEANT4 [22] simulator. It simulates the interaction of particles with various materials of the ATLAS detector, and the detector response such as ionization of gas in a detector is digitized. The output of the process is the same as the one from the real ATLAS detector, and it can be processed by the same software for the real data.

Under the high luminosity condition of the LHC, multiple collisions in one bunch crossing is expected. With typical condition of the LHC in 2011, the expectation is about ten[1]. In data, it is practically impossible to count the number of collision in a particular bunch crossing event. Instead, the average of the number in some time interval (2 minutes) is calculated from the luminosity measurement. Figure 2.30 shows the distribution. All the interactions except for the hardest one in one bunch crossing is called *pile-up* events. In the Monte Carlo simulation, such events are produced with PYTHIA6 and overlaid onto the main simulated events [23] [24]. Simulation with various number of interactions (1-20) is prepared, which is also shown in the figure, and each events are re-weighted according to the distribution in the data.

---

[1] The number is obtained by inserting typical values in the 2011 run : $n_1 = n_2 =\sim 10^{11}, \gamma \sim 4000, \beta^* = 1.0$, $\sigma^* \sim 1\mu$m, for one bunch crossing $n_b = 1, f_{\text{rev}} = 1$ in to the equation (2.2).

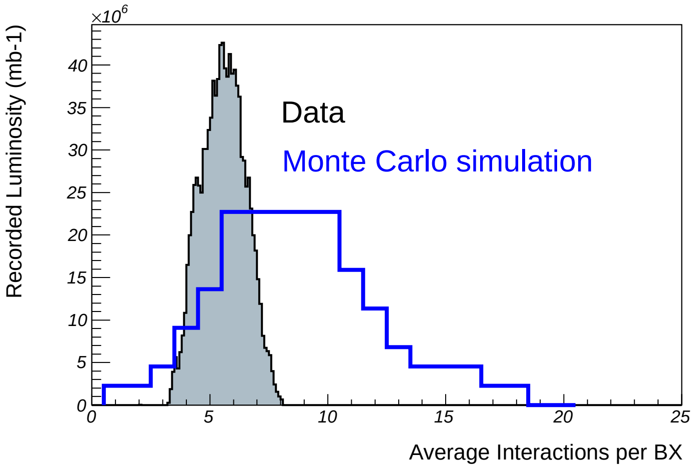

Figure 2.30: The mean of the number of interaction event μ in data, and prepared Monte Carlo simulation(not to scale).

2.4 Object Reconstruction

The analysis targets at di-lepton channel of the top quark pair, $t\bar{t} \rightarrow W^{+}bW^{-}\bar{b} \rightarrow l^{+}\bar{\nu}bl^{-}\nu\bar{b}$. The final state has two charged leptons, two neutrinos, and two bottom quarls associating extra partons. The ATLAS detector detects and reconstructs them. Figure 2.31 shows the event display of one typical signal ($e\mu$ channel) candidate. The b-quarks from top quark decays make many particles in parton shower and hadronization, which results in directional particle flows, so-called *jets*. In the event display, two localized and large energy deposits on the calorimeter are seen and they are reconstructed as jets. Especially jets from b-quarks can be identified from flight length of B-hadrons, which is called b-tagging. Electrons can be reconstructed from the signatures of large energy deposit on the electromagnetic calorimeter associated with one track. Muons can be identified from the tracks in the muon spectrometer which is matching to one track in the inner detector. Electrons and muons in the signal emerge from weak bosons. One of the characteristics of such leptons is that they are *isolated* from other particles, while leptons in semi-leptonic decays of hadrons have lots of particles around them. Two neutrinos are not observed in the detector, but their total transverse momenta is visible indirectly from unbalance of the transverse momentum in the event. This is called missing transverse energy, or $E_{\mathrm{T}}^{\mathrm{miss}}$ in short. In the following sections, reconstruction of these objects are summarized.

2.4.1 Track Reconstruction at the Inner Detector

The tracking in the inner detector is done by two methods. The one is "in-side out" and starting tracking from the silicon detector hits and extrapolating found track candidates into TRT region. The other method is "outside-in" which starts from TRT and extrapolates tracks into inside. The method works well for particles emerges away from the interaction point such as K_S decay and photon conversion $\gamma \rightarrow e^{-}e^{+}$.

The tracking is performed by Hough transformation for rough tracking for outside-in method, and

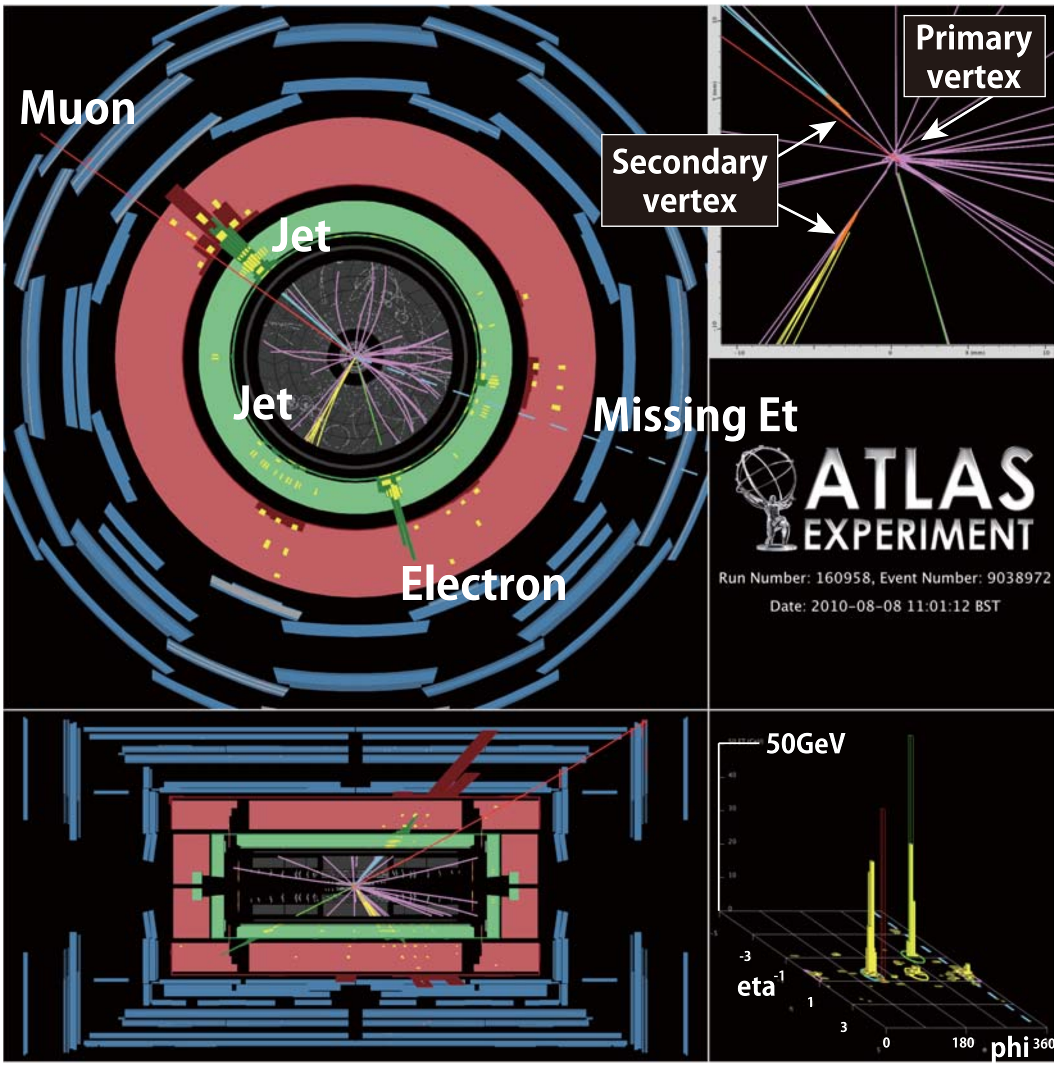

Figure 2.31: One signal candidate from data, which leaves clear typical signatures of the $e\mu$ channel. b-quarks are observed as jets that are localized energy deposits on the calorimeter. Bottom-right figure shows the energy deposits on η-ϕ plane. Looking into tracks associated to each jets as the top right figure, that in b-quark jets make another vertex apart from the primary one, which is called secondary vertex. This is the evidence of B-hadron and can be used for b-tagging of the jets. Electron deposit large energy on the electromagnetic calorimeter associated with one inner detector track, while the energy does not leak to the hadron calorimeter much. In the top-left figure, inner/outer circle out of the two stands for the electromagnetic/hadron calorimeter and the histogram heights corresponds to energy deposits. Muons can penetrate the calorimeter and leave tracks on the inner detector and muon spectrometer. These leptons from the signal are expected to be isolated, which is clearly seen from the bottom-left figure. The neutrinos are not directly observed but their total transverse momentum can be measured from the unbalance of the transverse momentum, which is indicated with dotted-lines on the figures.

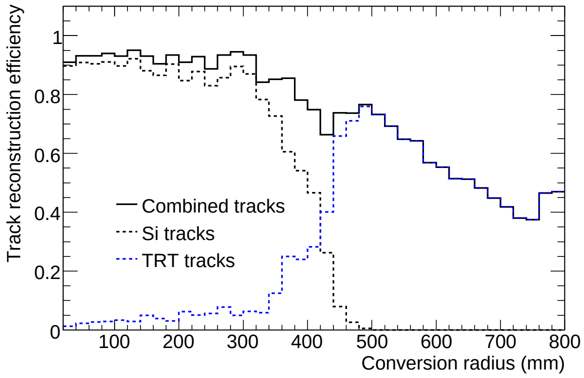

Figure 2.32: Track reconstruction efficiency of photon conversion tracks with respect to conversion point. The momentum of gamma is $P_T = 20$GeV. TRT-standalone tracks cover the region beyond radius of 400mm where inside-out tracks can not support.

Kalman-filter for that of inside-out and also for precise measurement in outside-in method.

Figure 2.32 shows the reconstruction efficiency of photon conversion. The two methods works complementary and realizes the high efficiency in the wide range.

2.4.2 Electron reconstruction

Reconstruction procedure

Electrons are reconstructed based on energy deposits on the calorimeter and tracks matching to the deposits.

The reconstruction algorithm searches a cluster on EM calorimeter with energy of more than 2.5 GeV in a scan window of $\eta \times \phi = 0.075 \times 0.125$, which works for almost 100% for electrons with $E_T > 15$GeV. And it searches a inner detector track that matches to the cluster. $\Delta\eta$ between the cluster and track is required to be smaller than 0.05 and $\Delta\phi$ than $0.05 - 0.10$.

The energies of the electron candidates are rebuilt with $3 \times 7 (5 \times 5)$ window in the barrel(endcap) region, taking into account energy deposit in from of the calorimeter, lateral and longitudinal energy leakage in the calorimeter. Their directions are determined by the track directions.

The candidates are equired to pass the quality criteria implemented by multi-variate analysis program, so-called MVTA, with the input variables summarized in the Table 2.3. Some distributions that give strong discrimination is shown in Figure 2.33.

Since this analysis is interested in the electrons from W boson, the ones from photon conversions are needed to be rejected. Photon conversion probability is constant with its energy and its cross section is given by the formula

$$\sigma = \frac{7A}{9X_0N_A}$$

where N_A is the Avogadro number, where A is the atomic mass and X_0 is the radiation length of the material. Figure 2.34(left) shows the amount of the material from the interaction point, and Figure

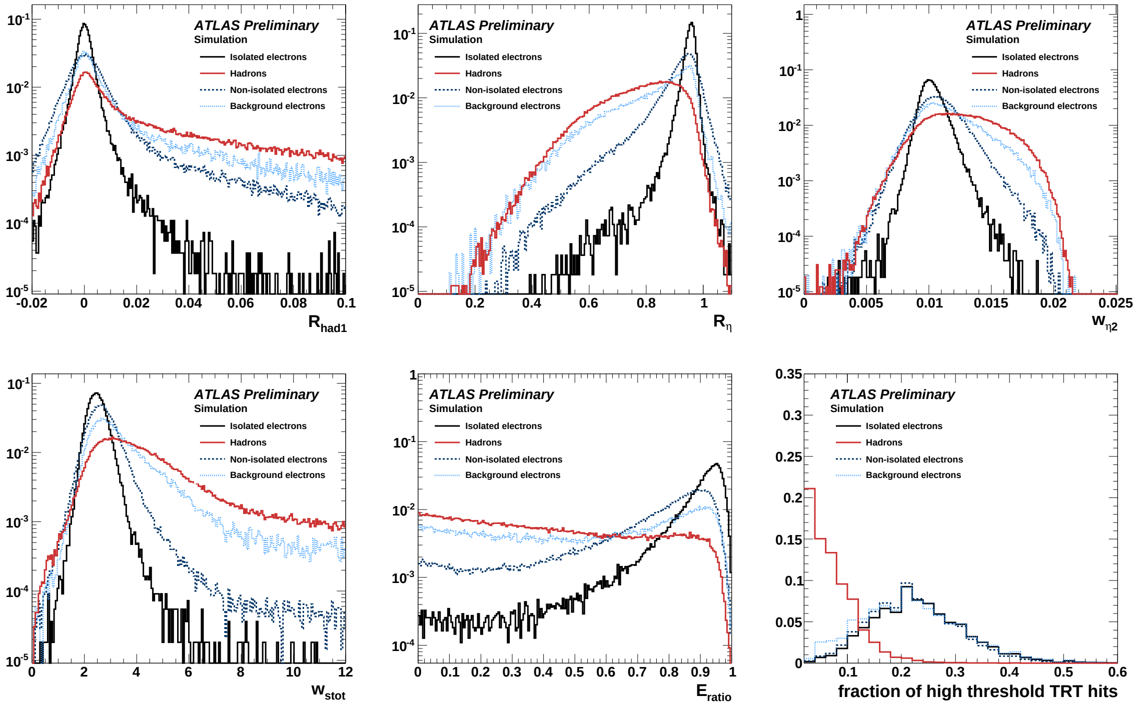

Figure 2.33: Some typical distributions used in the electron quality selections. (Top) R_{had1}, R_η, W_{eta2} (bottom) w_{stot}, E_{ratio} and the fraction of high threshold hits in the TRT. The definition of them as in Table 2.3. More details in [25].

2.34(right) shows the conversion probability for a photon with $P_T = 1$ GeV as a function of its flight length. In $\eta = 1.5$, for example, the conversion probability is about 0.6, which is not negligible.

Electrons are identified as ones from photon conversion by searching another electron with which the electron makes a cross point assuming that they are from a massless particle, photon. The tagged electrons are rejected from the list of electrons used in this analysis.

Due to the LAr hardware problem mentioned in section 2.2.2, electrons are not well reconstructed in the region where the electronics boards have broken. In the physics analysis, electrons candidates reconstructed with some dead cells are rejected. In order to emulate the condition, all reconstructed electrons in the simulation are checked based on the same hardware conditions as data, and are rejected if they are not satisfy the quality check. This special treatment is done for 86% of the simulated events, that corresponds to the fraction of the data affected by the hardware issue.

Reconstruction efficiency

The reconstruction efficiency is evaluated in both data and Monte Carlo simulation. Such evaluation needs pure electron samples without bias. Here, *tag-and-probe* method with Z boson events is used.

In general, the method uses Drell-Yan events that provide high purity leptons by tagging the event with one of the leptons in the event. For the *tag* lepton, high purity lepton is used by requiring tight selection criteria in the reconstruction. And, if needed, it is required that the online trigger in the event

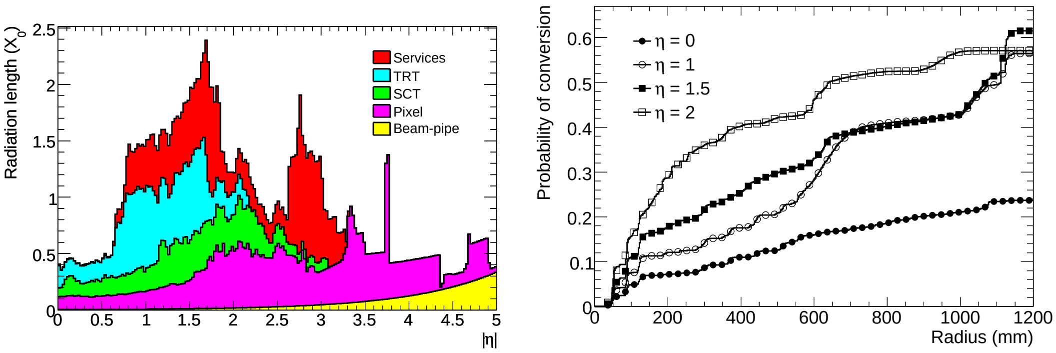

Figure 2.34: (left) Material in ATLAS detector as a function of $|\eta|$. (right) Photon conversion probability for photons with 1 GeV for different directions. [25]

has fired due to the tag lepton. The other reconstructed lepton, so-called *probe* lepton, is expected to be high purity lepton without requiring the tight criteria since they reconstructs the resonance. Also the probe leptons are trigger-bias free. The probe lepton can be used to estimate the efficiencies of detection, reconstruction and trigger.

The Z boson decaying into di-electron produces high energy electrons around $\mathcal{O}(10)$ GeV and up to few hundreds GeV, which are just the region which the analysis looks into.

For tag electron, the requirements as described in the previous selection are applied. For probe electron, clusters before taking matching with tracks are used, since the cluster formation of true electrons is almost 100% for electrons with $E_T > 15$ GeV.

Figure 2.35 shows the reconstruction efficiencies in data and Monte Carlo simulation. The contaminating backgrounds are estimated from a control region that is outside of Z boson mass window and same charge sign combination(e^+e^+ and e^-e^- events). The systematic uncertainties are taken into account by changing the Z mass region in $M_{ee} = [80 : 100], [75 : 105], [85 : 95]$ and control region $M_{ee} = [60, 120], [58, 122], [62, 118]$. Also deviation by changing the identification requirement on the tag electron are taken into account.

Energy scale and resolution

The reproduction of the energy scale and resolution of reconstructed electron in the Monte Carlo simulation are tuned based on the Drell-Yan, $Z \to ee$, events.

As the the energy scale, the momentum of the reconstructed electron is scaled by equation

$$E_{\mathrm{MC}}^{\mathrm{corr}} = \frac{E_{\mathrm{MC}}}{1 + \alpha(\eta)} \tag{2.8}$$

where α is the correction factor as a function of η, so that the invariant mass distribution of di-electron reproduce the Z boson mass peak in data. Figure 2.36 shows the estimated α.

As to the resolution, reconstructed momentum in the Monte Carlo simulation is smeared by equation

$$E_{\mathrm{MC}}^{\mathrm{smear}} = E_{\mathrm{MC}}(1 + Gaus(0, \beta(\eta))) \tag{2.9}$$

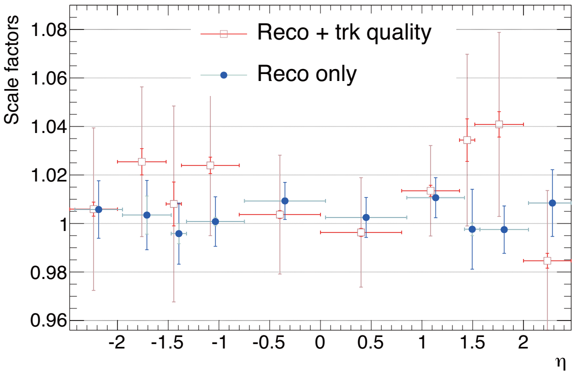

Figure 2.35: The scale factor of electron reconstruction efficiency. “Reco + trk quality” is the one used in this analysis.

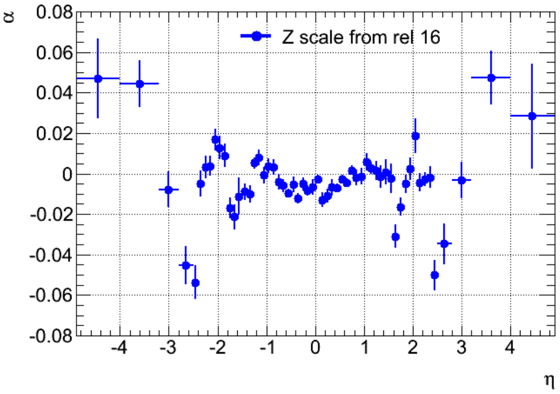

Figure 2.36: Electron energy scale factor α which applied onto the reconstructed electrons in the Monte Carlo simulation with equation (2.8).

where *Gaus* is a random number that follows the Gaussian distribution with mean of 0 and sigma of β. The β is also tuned with Z boson events, and $\beta = 0.1$ in $|\eta| < 0.6$ and $\beta = 0.15$ in the rest region are obtained.

2.4.3 Muon reconstruction

Reconstruction procedure

In the ATLAS detector, muon tracks are reconstructed independently in the inner detector and muon spectrometer, and combined. The reconstruction in the inner detector is as section 2.4.1.

The reconstruction in the muon detector starts from R and ϕ direction separately since the MDT has high precision in R once ϕ information from the MDT and TGC are available. The first tracking in the R direction is done with the MDT tube resolution. The reconstructed tracks in each direction are combined and re-tracking is performed with full-precision of the MDT with ϕ information.

The reconstructed muon tracks in the muon spectrometer are extrapolated toward the interaction point. It is done taking into account the energy deposit during passing through the detector, which typically accounts for 3 GeV.

The matching with track reconstructed in the inner detector is done based on the χ^2 fitting of the track parameter.

Combined tracks are required to pass quality selection criteria summarized in Table 2.4.

Reconstruction efficiency

The muon reconstruction efficiency is evaluated in data and Monte Carlo simulation, with the tag-and-probe method which is also used for the estimation for electron in section 2.4.2. The track reconstruction efficiencies in the inner detector and muon spectrometer are evaluated individually, and they are combined. This is possible by using inner detector tracks in order to look into the performance of track reconstruction in the muon spectrometer, and vice versa, since the muon tracks are reconstructed independently. Table 2.5 summarize the requirements on the tag and combined muons, and matching between tracks of the inner detector and muon spectrometer.

Figure 2.37 shows the inner detector track reconstruction efficiency, and Figure 2.38 shows combined muon reconstruction efficiency.

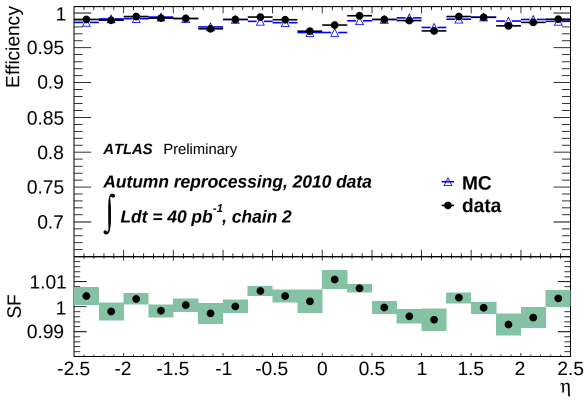

Figure 2.37: The muon reconstruction efficiency in the inner detector. [26]

Momentum scale and resolution

Muon momentum scale and resolution in the Monte Carlo simulation have been tuned with Z boson events, as done for electrons in section 2.4.2. A detail description of the procedure in early phase(data in 2010) is summarized in section 3.2.1.

The scale factor α is defined

$$P_T^{MC,scaled} = \alpha P_T^{MC,measured} \tag{2.10}$$

and evaluated results are in Table 2.6. They are all close to 1.

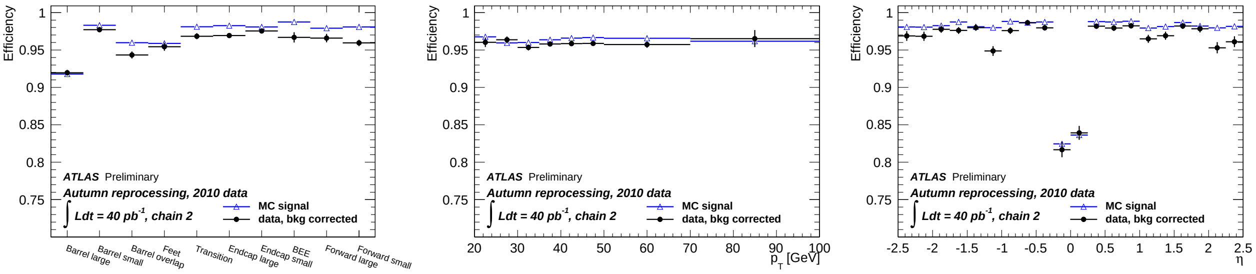

Figure 2.38: The muon reconstruction efficiency as combined muons in each detector region(left), in P_T(middle) and in η(right). [26]

As to muon momentum resolution, it is divided into two components of resolution in the inner detector and muon spectrometer since the resolutions are determined their combination.

The reconstruction resolutions in data and the Monte Carlo simulation is parameterized. The resolution in the muon spectrometer are parameterized with an equation :

$$\sigma_{\mathrm{MS}}/P = \frac{p_0^{\mathrm{MS}}}{P_T} \oplus p_1^{\mathrm{MS}} \oplus p_2^{\mathrm{MS}} P_T \tag{2.11}$$

where the parameter p_0^{MS}, p_1^{MS} and p_2^{MS} are the parameter related to the energy loss in the material, multiple scattering and intrinsic resolution terms, respectively. For the resolution at the inner detector, two parameterization are adapted in two regions, $|\eta| < 1.9$ and $|\eta| > 1.9$. The latter is the region beyond the TRT detector coverage.

$$\sigma_{\mathrm{ID}}/P = p_1^{\mathrm{ID}} \oplus p_2^{\mathrm{ID}} P_T \quad |\eta| < 1.9 \tag{2.12}$$

$$\sigma_{\mathrm{ID}}/P = p_1^{\mathrm{ID}} \oplus p_2^{\mathrm{ID}} P_T \frac{1}{\tan^2\theta} \quad |\eta| > 1.9 \tag{2.13}$$

The resolution is evaluated in this parameterization in the same technique with the evaluation of reconstruction efficiency, The difference between data and Monte Carlo simulation is compensated by smearing the reconstructed muon momentum in the Monte Carlo simulation, muon by muon, following the equation [27]

$$P_T^{\mathrm{smear}} = P_T\Big[1 + \frac{\frac{\Delta(\mathrm{MS})}{\sigma_{\mathrm{MS}}^2} + \frac{\Delta(\mathrm{ID})}{\sigma_{\mathrm{ID}}^2}}{\frac{1}{\sigma_{\mathrm{MS}}^2} + \frac{1}{\sigma_{\mathrm{ID}}^2}}\Big] \tag{2.14}$$

Here Δ(MS) and Δ(ID) are

$$\Delta(\mathrm{MS}) = \frac{\Delta p_0^{\mathrm{MS}}}{P_T} g_0^{\mathrm{MS}} + \Delta p_1^{\mathrm{MS}} g_1^{\mathrm{MS}} + \Delta p_2^{\mathrm{MS}} P_T g_2^{\mathrm{MS}} \tag{2.15}$$

$$\Delta(\mathrm{ID}) = \Delta p_1^{\mathrm{ID}} g_1^{\mathrm{ID}} + \Delta p_2^{\mathrm{ID}} P_T g_2^{\mathrm{ID}} \quad |\eta| < 1.9 \tag{2.16}$$

$$\Delta(\mathrm{ID}) = \Delta p_1^{\mathrm{ID}} g_1^{\mathrm{ID}} + \Delta p_2^{\mathrm{ID}} P_T \frac{1}{\tan^2\theta} g_2^{\mathrm{ID}} \quad |\eta| > 1.9 \tag{2.17}$$

where Δp_i is the difference of parameter p_i between data and Monte Carlo simulation, and g_i is randomly chosen number of Gaussian distribution with mean of 0 and standard deviation of 1. Detail numbers are in [27].

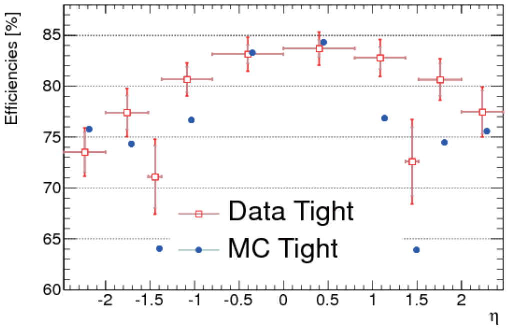

Figure 2.39: Electron isolation efficiency with respect to η in data and the Monte Carlo simulation. [28]

2.4.4 Lepton isolation

The analysis is interested in the leptons from the W bosons, and one type of the backgrounds has leptons from semi-leptonic decay of heavy hadrons. The latter leptons tend to have many other particles around the lepton compared to the former. For the electrons and muons used in this analysis, less activity around them, so called *isolation*, is required.

For electrons, total E_T in the cone of $\Delta R = 0.3$ except for the electron energy is required to be less than 3.5 GeV. The isolation criteria for electron is evaluated with the tag-and-probe method, which is described in section 2.4.2. For the tag electron, reconstructed electrons passing the isolation criterion is used, and just reconstructed electrons before the isolation requirement is used for the probe electron, The definition of the Z boson mass window, background control region and the estimation of systematic uncertainties are the same as 2.4.2. Figure 2.39 shows the evaluated isolation efficiency.

For muons, the variable of energy deposits in the cone of $R = 0.3$ around the muons are defined as for electrons(above), and is required to be smaller than 4 GeV. Also, the sum of transverse momenta of tracks in the cone of $R = 0.3$ around the muons are required to be smaller than 4 GeV. Furthermore, muons which has any jet with $P_T > 20$ GeV within the radius of 0.4 around the muons are removed. The efficiency of the isolation is summarized in section 3.2.3.

variable	description
R_{had1}	Ratio of E_T in the first layer of the hadronic calorimeter to the one of the EM cluster. This is used over the range $\lvert\eta\rvert < 0.8$ and $\lvert\eta\rvert > 1.37$. Isolated electrons deposit most of their energy at the EM calorimeter and the leakage to the hadron calorimeter is small compared to that of hadrons and non-isolated electrons.
R_{had}	Ratio of E_T in the hadronic calorimeter to the one of the EM cluster. This is used over the range $\lvert\eta\rvert > 0.8$ and $\lvert\eta\rvert < 1.37$.
R_η	Ratio of the energy in 3×7 cells to the one in 7×7. The larger the leakage of energy to η direction is, the smaller the variable is. Isolated electron tends to deposit its energy locally and R_η tends to be close to 1.
$\omega_{\eta 2}$	Lateral shower width defined as $\omega_{\eta 2} \equiv \sqrt{\frac{\sum E_i \eta_i^2}{\sum E_i} - (\frac{\sum E_i \eta_i}{\sum E_i})^2}$ where E_i is the energy and η_i is the pseudo-rapidity of i-th cell and the sum is calculated in a window of 3×5 cells. This definition corresponds to the RMS of cluster η distribution weighted by clusters' energies.
ω_{stot}	Shower width defined as $\omega_{\text{stot}} = \sqrt{\frac{\sum E_i (i - i_{\text{max}})}{\sum E_i}}$ where i runs over all the strips in a window of $\Delta\eta \times \Delta\phi \approx 0.0625 \times 0.2$ and i_{max} is the index of the highest energy strip. The isolated electron tends to have smaller value compared to the others.
E_{ratio}	Ratio of the energy difference between the largest and second largest energy deposit to the total in the cluster : $E_{\text{ratio}} = \frac{E_{\text{the largest}} - E_{\text{the second largest}}}{\sum E_i}$. Isolated electron tends to distribute around 1 and that of hadrons tend to be smaller.
$n_{\text{pixel}}, n_{\text{Si}}$	The number of hits on the pixel and silicon detectors. $n_{\text{pixel}} \geq 1, n_{\text{Si}} \geq 7$ are required.
d_0	Impact parameter of the track with respect to the beam spot. $d_0 < 1$ mm is required.
$\Delta\eta, \Delta\phi$	$\Delta\eta(\Delta\phi)$ between the extrapolated track and the cluster position in the strip layer (in the middle layer) . Isolated electrons has sharp distributions in both case.
E/p	Ratio of the cluster energy to the momentum of the track. Electrons are expected to have the ratio close on 1, but others tend to have smaller.
n_{TRT}	The number of hits on the TRT detector.Background electrons tend to have smaller entries as is the case in n_{pixel}, and n_{Si}.
f_{HT}	The fraction of high threshold TRT hits. The variable has strong separation of electron and hadron as described in section 2.2.1.
n_{BL}	The number of hits on Pixel b-layer, which is required to be ≥ 1.

Table 2.3: The variables used in the MVTA of the electron quality selections. Isolated electrons stands for the ones from the weak bosons, as the discrimination from ones from heavy quarks decay. More details in [25].

detector	requirements
Most inner layer	At least one hit on the most inner layer of the pixel detector, or the extrapolated track of the muon passes through dead or un-instrumented region of the detector.
Pixel	At least two hits in the pixel detector. If the track passes through dead region, it is counted as one hit.
SCT	At least six hits in the SCT detector. If the track passes through dead region, it is counted as one hit.
Silicon detector	The total number of layers of the pixel and SCT detector without hits must be less than three.
TRT	let the $N_{\mathrm{TRT}}^{\mathrm{hit}}$ be the number of hits on the TRT along the track, $N_{\mathrm{TRT}}^{\mathrm{outliers}}$ be the one of hits lying in the vicinity of the track but removed at the final track fitting, and $n = N_{\mathrm{TRT}}^{\mathrm{hit}} + N_{\mathrm{TRT}}^{\mathrm{outliers}}$, the fllowings are required $\lvert\eta\rvert < 1.9 : n > 5$ and $N_{\mathrm{TRT}}^{\mathrm{outliers}}/n < 0.9$ $\lvert\eta\rvert >= 1.9$: if $n > 5$, $N_{\mathrm{TRT}}^{\mathrm{outliers}}/n < 0.9$

Table 2.4: The detector hit requirements on the reconstructed muon.

Tag muon	
reconstruction	combined muon
isolation	$\sum P_T^{\mathrm{track}}/P_T^{\mathrm{tag\ muon}} < 0.2$ where the numerator is the P_T sum of tracks in $\Delta R < 0.4$ around the muon.
muon P_T	$P_T > 20$ GeV
muon *eta*	$\lvert\eta\rvert < 2.4$ (= in the muon trigger acceptance.)
trigger matching	associated to the trigger for which the event taken.
z_0	longitudinal distance from the primary vertex $\lvert z_0\rvert < 10$ mm
Probe muon	
reconstruction	inner detector track or muon spectrometer track
muon P_T	$P_T > 20$ GeV
muon η	$\lvert\eta\rvert < 2.5$ (= the full acceptance of the muon reconstruction)
z_0	$\lvert z_0\rvert < 10$ mm, $\lvert z_0^{\mathrm{probe}} - z_0^{\mathrm{muon}}\rvert < 3$ mm .
charge	Opposite charge with tag muon
opening angle	$\Delta\phi(\mathrm{tag,\ probe}) > 2.0$
invariant mass	$\lvert m_{\mu\mu} - m_Z\rvert < 10$ GeV
Matching between muons in the inner detector and muon spectrometer	
ΔR	$\Delta R < 0.01$
charge	same charge.

Table 2.5: The condition required on the tag and probe muon in the reconstruction efficiency estimation.

region	Scale Factor α
$\lvert\eta\rvert < 1.05$	0.9997 ± 0.0002
$1.05 < \lvert\eta\rvert < 1.7$	0.9999 ± 0.0006
$1.7 < \lvert\eta\rvert < 2.0$	0.9990 ± 0.0012
$2.0 < \lvert\eta\rvert < 2.5$	1.0013 ± 0.0007

Table 2.6: The scale factor for muon momentum scale in the Monte Carlo simulation

2.4.5 Jet reconstruction

Reconstruction procedure

Quarks, including bottom quarks in top quarks decays, are not observed directory but as hadrons due to the color confinement of the QCD. High energy quarks make directional flows, so-called jets, as the result of parton shower and hadronization. Since jets are not a physics object like electron or muon, but a phenomenon, there is ambiguity in its definition. In general, jets are reconstructed by gathering energy deposits and tracks under some algorithm, *Anti-kt* algorithm is used for the energy deposits on calorimeter in this analysis.

In the reconstruction, the energy deposits are gathered as clusters. Here, only the cells with significant energy deposits compared to noise and their neighbors are considered. The clusters with more than two peaks are split into smaller clusters so that all the clusters have just one peak.

The Anti-kt algorithm forms jets with the clusters. At the step, clusters are no longer treated as groups of cells but just objects with momenta. The sort is done based on the distance between clusters which is defined as[2]

$$d_{ij} = \min({P_T}_i^{-2}, {P_T}_j^{-2})\Delta R^2 \quad (i, j : \text{indices of the clusters}) \tag{2.18}$$

where ${P_T}_i$ is transverse momentum of cluster i, and ΔR is the distance between the two clusters in the η-ϕ space. Starting from the combination of clusters that gives the shortest distance, if ΔR is smaller than a certain threshold $R_{\text{cone size}}$, the two clusters are merged into one. In this analysis, $R_{\text{cone size}} = 0.4$ is used. If $\Delta R > R_{\text{cone size}}$, the cluster with smaller P_T^{-2} is removed from the cluster list in this step and treated as one jet. This procedure is repeated until all the clusters are included in jets.

The anti-kt algorithm has following desirable features compared to the other ones.

Infrared safe In general, extra partons with very small energy may emerge in parton showering, and make clusters with small energy. For the jet reconstruction algorithms, it is desirable that defined jets does not alter depending on the existence of such radiations, and such algorithms are called "infrared safe".

The anti-kt algorithm merge clusters in ascending order of d_{ij}, which means clusters with large energy tends to be merged before ones with small one. Therefore the most of the jet reconstruction are defined by the energetic clusters and less energetic ones act just like perturbation, and it is infrared safe.

Collinear safe In the parton shower, the more particles a parton decays into, the less energetic the each particle is. The division of the momentum to them may fluctuate and the order of cluster merger is easily swayed. Since jets are defined in order to investigate to the parton shower development but the kinematics of the original partons emerged in the hard scattering, it is desirable that algorithms construct the same jet regardless how many particles a parton decays into, which is called collinear safe. Since anti-kt algorithm gather clusters in the radius of R as mentioned in "passive area" above, and it has this desirable feature.

---

[2] The point of the anti-kt algorithm is the definition of the distance. For example, the Cam/Aachen algorithm uses just ΔR and the kt algorithm uses P_T^2 instead of P_T^{-2}. Historically, the anti-kt is derivation of kt. The abbreviation "kt" stands for transverse momentum and equivalent to P_T in this document.

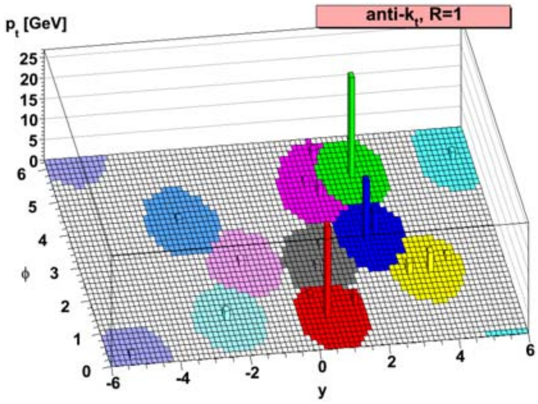

Figure 2.40: Constructed jets with anti-kt algorithm. A group of cells with the same color corresponds to one jets.

Passive area Passive area of a jet is defined as area where one test cluster with negligibly small energy, so-called "ghost cluster", is merged into the jet. The passive area of anti-kt jet is $\pi R^2_{\text{cone size}}$, that is the jets collect clusters within the radius of $R_{\text{cone size}}$.

Active area Active area A of a jet is defined as effective region, when ghost clusters distributes evenly in the η-ϕ space, calculated from the number of ghost clusters merged into the jets(N_{ghosts}) and ghost clusters density(ν) : $A = N_{ghosts}/\nu$. The area of anti-kt jets is also $\pi R^2_{\text{cone size}}$, and it corresponds to the color region in Figure 2.40.

Due to the hardware in the LAr detector mentioned in section2.2.2, jet reconstruction quality is worsen in the effected region. In this analysis, the events with jet with $P_T > 20$ GeV, in the region are vetoed.

Energy and direction calibration

The energy and direction of reconstructed jets are calibrated.

The overestimate of energy due to pile-up events are taken into account as a function of the number of vertexes. Figure 2.41 shows the correction.

In the reconstruction, the jet directions is defined with respect to the interaction point. At this step, the kinematics variables are re-calculated with respect to the primary vertex. This does not change energies of jets much but improved their angular resolution in < 1%.

Next, the reconstructed jets energy is translated into the "truth" jet, which is an object defined by performing the anti-kt algorithm on the truth particles with lifetime longer than 10 ps in the Monte Carlo simulation. The response function R which is defined as

$$R = \frac{E^{jet}_{recon}}{E^{jet}_{truth}} \tag{2.19}$$

is evaluated as Figure 2.42 shows.

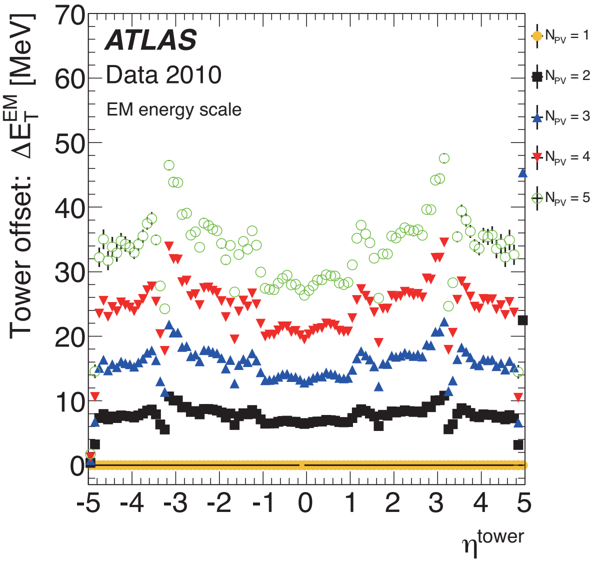

Figure 2.41: The correction of pileup effect on the jet energy by cell tower level with respect to the events of $N_{\mathrm{PV}} = 1$.

Finally, biased on η of jets is calibrated, which emerge due to ununiformity of the calorimeter active region in η direction due to the detector structure. Regions with dead material tend to obtain smaller visible energy deposits compared to well-implemented region. The energy calibration works stronger on the cell with large energy deposits, and η of reconstructed jets tend to be swayed toward the region. Figure 2.43 shows the amount of the calibration.

Uncertainty on the energy scale

The jet energy scale is verified with jets, each of which one single track is associated with, by comapring jet energy to the momentum of the track. The unncertainty on the energy scale comes from several components.

One is non-closure of the jet energy scale calibration. The reconstructed jets are calibrated as above, the response of reconstructed jets, however, still are not unity, especially for lower P_T jets as Figure 2.44 shows. This is caused because the same correction scale factor is applied on the jet energy and momentum. The discrepancy from the unity is taken account to as a systematic uncertainty.

There is uncertainty from the understanding of the detector. The proto type of the ATLAS detector is tested with test-beam in 2004, and the detector response with respect to particles with energy of 20-350 GeV is obtained. And uncertainty on the measurement is taken into account the jet measurement.

The noise modeling in the calorimeter is taken into account by changing the noise fluctuation in the Monte Carlo simulation based on the data observation.

The precise measurement of effect of dead material is studied, for example, with single isolated track events [29]. The measurement, however, uses reconstructed inner track and dead region of inner detector tracking can not be tested. In order to take into account it, the special Monte Carlo

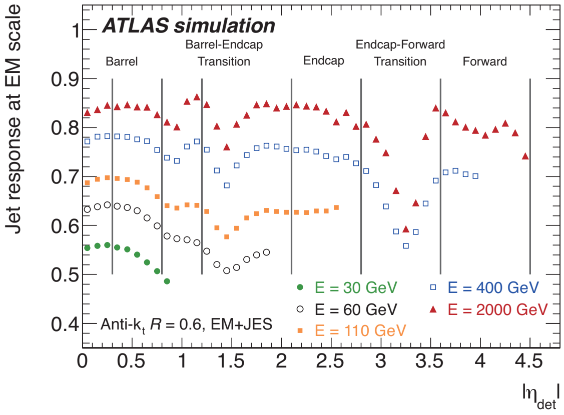

Figure 2.42: The response function R as a function of $|\eta|$ and jet energy.

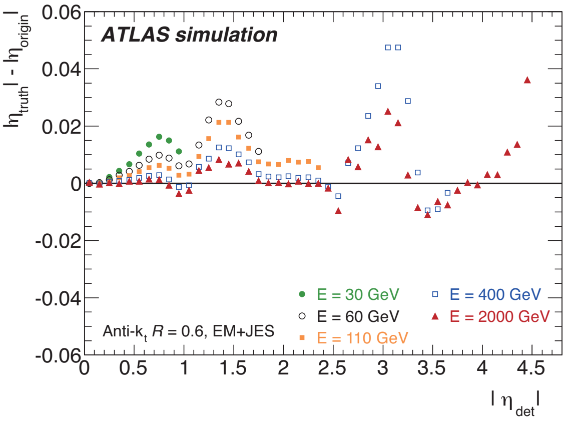

Figure 2.43: Jet η calibration after jet energy correction.

simulation with the dead material in the inner detector is modified by 5% is prepared and its effect on the jet reconstruction is evaluated.

The difference from Monte Carlo simulation, especially parton showers is evaluated as the difference between the base sample, PYTHIA Monte Carlo, and ALPGEN+HERWIG+JIMMY. Also PYTHIA PERUGIA tune [30] is tested, which is independent tune with PYTHIA, and it is known for a well description of the internal structure of jets.

The Figure 2.45 summarizes the jet energy scale uncertainties coming from these sources.

Momentum resolution

Momentum resolution is evaluated from data with two methods. The first one(di-jet valance) use the P_T balance of di-jet events, assuming the equivalent resolution of the jets in the same detector region. The soft radiation effect is estimated by extrapolating the third jets momentum ${P_T}^{3\text{rd}} \to 0$.

The other method uses the transverse momentum of the di-jet system $\vec{P}_T$. The non-zero value of

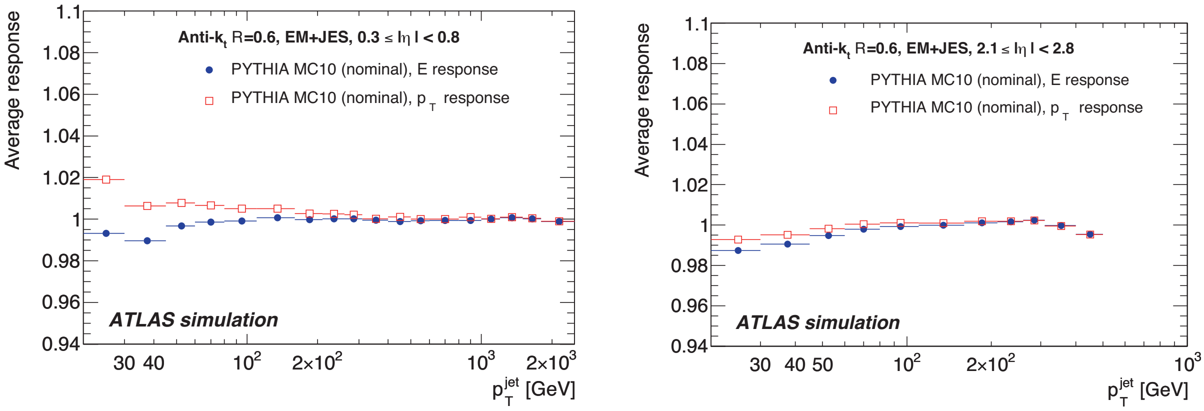

Figure 2.44: Jet energy response after the calibration in each region. They are expected to be unity but slightly away, since the same ccalibration factor is applied for energy and momentum.

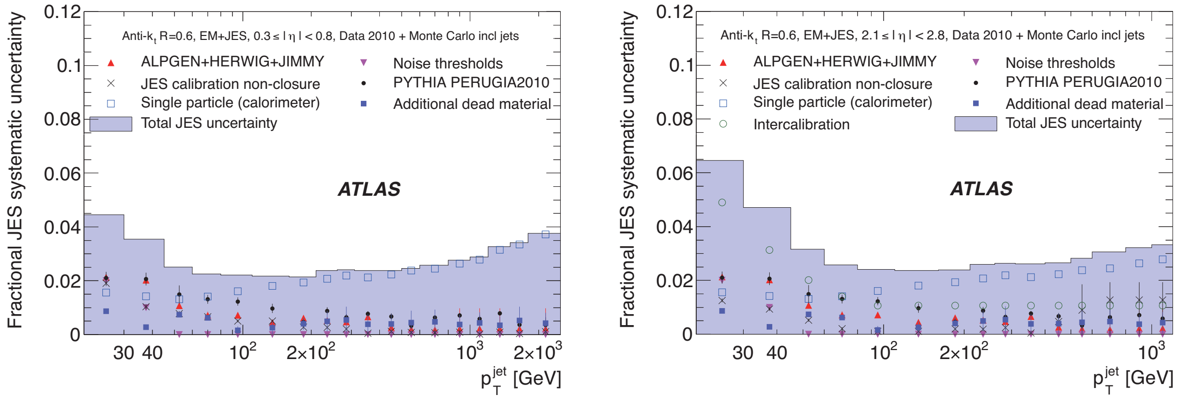

(a) $0.3 \leq |\eta| < 0.8$ (b) $2.1 \leq |\eta| < 2.8$

Figure 2.45: Jet energy scale uncertainties in each η region [31].

$\vec{P}_T$ comes from intrinsic effect due to radiation at particle level, $\sigma^{particle}$, and calorimeter resolution σ^{cal}. If $\vec{P}_T$ is projected along the axis(η) that bisects the opening angle $\Delta\phi$ between the two jets and another axis ψ that is orthogonal to η, $\sigma^{particle}$ contributes on both η and ψ. Meanwhile, σ^{cal} does not contribute on the ψ direction, because the third jets is produced preferential close to one of the high energy jets. Assuming the equivalent resolution of the two jets in the same detector region,

$$\frac{\sigma(p_t)}{p_t} = \frac{\sigma_{\psi}^{2\ \text{calo}} - \sigma_{\eta}^{2\ \text{calo}}}{\sqrt{2}p_T\sqrt{\cos\Delta\phi}} \tag{2.20}$$

and the similar equation is applicable for a pair of jets in different detector region.

Figure 2.46 shows the energy resolution measured by the two methods, and they agree within 2-3% up to $p_T = 500$ GeV. Figure 2.47 shows the uncertainties of the methods and combined uncertainty in quadrature taking into account their result difference. For di-jet balance method, uncertainties

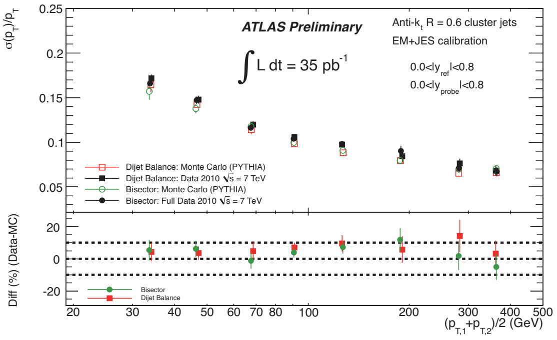

Figure 2.46: Jet energy resolution in data and Monte Carlo simulation measured in the two methods.

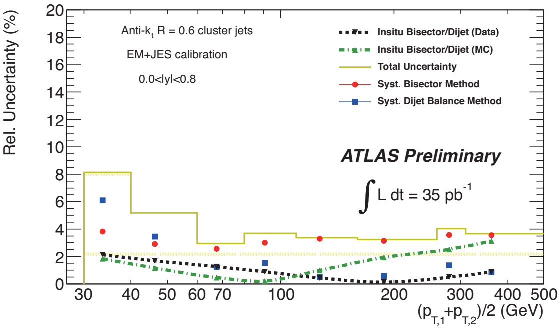

Figure 2.47: The uncertainties of the jet energy resolution measurements.

from $\delta\phi$ cut between the di-jet and soft radiation modeling are considered. For bi-sector method, momentum threshold of the third jet is taken into account.

Reconstruction efficiency.

The efficiency is evaluated in two steps. It is confirmed that the matching efficiency of track jet to a calorimeter jet in data is described well by the Monte Carlo simulation. The track jet is reconstructed with the same algorithm as the calorimeter jet, anti-kt, but not with energy deposit on the calorimeter but with track momentum. Since track and calorimeter jets are reconstructed with completely exclusive detectors, the good agreement of the Monte Carlo simulation to data supports that the jet reconstruction efficiency estimated in the Monte Carlo simulation is applicable to data.

The matching efficiency is estimated by the tag-and-probe method (the method is described in section 2.4.2). Di-jet events are tagged with the highest P_T calorimeter jet, and another track jet that makes large opening angle $|\Delta\phi| > 2.8$ with the leading jet. And the matching efficiency of the track jet to a calorimeter jet is evaluated. Figure 2.48(left) shows the results in data and Monte Carlo simulation and good agreement is seen.

Calorimeter jets reconstruction efficiency with respect to the truth jet is evaluated in the Monte Carlo simulation. Figure 2.48(right) shows the results and it reached at plateau of almost 100% around

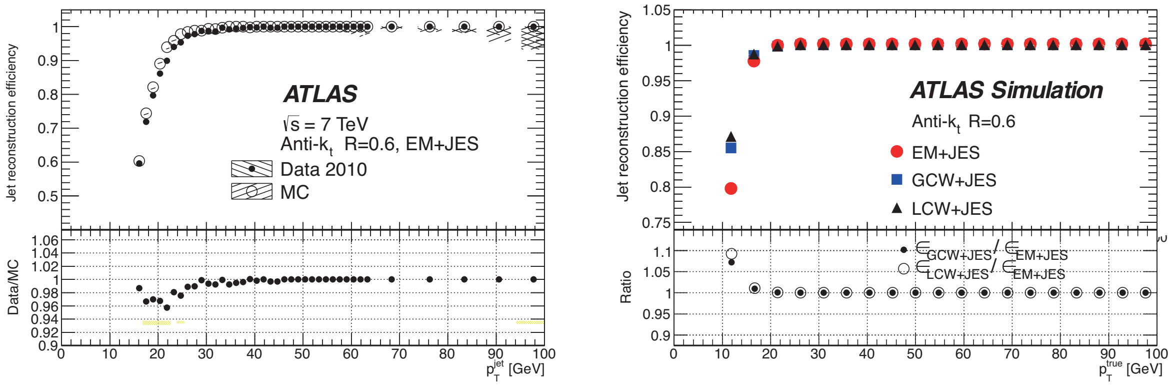

Figure 2.48: (left) Jet matching efficiency from track jet to calorimeter jet. (right) Calorimeter jet reconstruction efficiency with respect to truth jets.

$P_T = 25$ GeV.

The systematic uncertainties on this measurement are evaluated by varying the event selections in the tag-and-probe method : $\Delta\phi$ cut, and distance threshold for matching between calorimeter and track jets. And 3% uncertainties is assigned for jets with $P_T < 30$ GeV.

Fake jet removal

In the reconstructed jets, the energy deposits not coming from physics, such as noise and cosmic ray may contributes. In order to identify such events, following criteria are applied.

Noise burst may happen on hadronic endcap calorimeter(HEC)

Such fake jets can be identified by a large energy fraction on HEC f_{HEC} and poor signal shape $f_{\mathrm{HEC\ quality}}$ compared to ideal signal shape, which is mentioned in section 2.2.2.

Coherent noise in the electromagnetic calorimeter

It can be identified by a large energy fraction on the calorimeter f_{EM} and signal shape quality $f_{EM\ quality}$, which is mentioned in section 2.2.2.

Accidental cosmic ray

This can be identified by jet "timing" t_{jet} that is defined as a weighted sum of reconstruction time on each cell t_{cell} by the square of its energy E_{cell}, numerically, $t_{\mathrm{jet}} = \sum_{\mathrm{cell}} t_{cell} E_{\mathrm{cell}}^2 / \sum_{\mathrm{cell}} E_{\mathrm{cell}}^2$

Also, low f_{EM} can be used to reject cosmic because particles from interactions should leave a certain fraction of their energy on the first layer of the calorimeter. Furthermore, the energy fraction of charged tracks associated to a jet with respect to the energy of the jet f_{CH} can be also used, which rejects fake jets by cosmic rays such that the cosmic muons pass though calorimeter but not the inner detector.

non-collision background

Threshold to the maximum energy fraction in any calorimeter layer f_{MAX} is set.

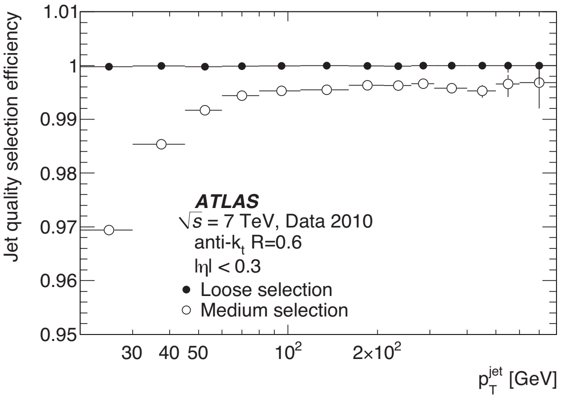

Figure 2.49: Jet selection efficiency by bad jet rejection criteria. “Loose selection” corresponds to the one used in this analysis, which keeps almost 100% throughout the whole range. The same tendency was seen in other $|\eta|$ region too.

The efficiency of these criteria was measured in di-jet event with $P_T > 20$ GeV , and it is found to be almost 100 % as figure 2.49 shows.

2.4.6 b-tagging of jet

The one of the most important signature of the top quark decay is the existence of b-quark jets. B hadron has enough long lifetime of $O(10^{-12})$ second, for example, lifetime of $B^{\pm}$ is $(1.636 \pm 0.011)^{-12}$ seconds and $c\tau = 491\mu$m, so that it may fly a measurable distance before it decays. The identification of b-quark jet, so called *b-tagging*, is based on the flight length of B hadrons. Track of their daughter particles reconstruct a vertex apart from the primary vertex, so-called *secondary vertex*, The b-tagger used in this analysis associates tracks to calorimeter jets, and measures the significance of the secondary vertex.

Table 2.7 summarize the requirements on tracks to be associated with jets, and the association condition. Figure 2.50 shows the significance of transverse and longitudinal impact parameters of each tracks associated each jets. Tracks from heavy quarks tend to have large significance.

This analysis adopts a b-tagger that is combination of two algorithm. The one algorithm uses the impact parameter significance of the tracks and evaluated probability by comparing to the Monte Carlo simulation. The other algorithm [32] reconstructs a line and positions of the primary and secondary vertex on the line with a Kalman filter, and evaluates the significance of the separation of the point. Figure 2.51 shows the output scores from the two method and their combination. It is clearly seen that heavy quark jets tend to obtain high score.

Performance of b-tagger must be discussed with efficiency and also light jet rejection power simultaneously. The figure 2.52 shows the b-tagger efficiency and rejection power, which are anti-correlation each other with respect to the threshold on the score. This analysis adopts the threshold corresponding to 70% b-tagging efficiency point, which corresponds to light jet rejection power of ~ 100.

The discrepancy in the score distribution between data and the Monte Carlo simulation are com-

Track quality	
on the pixel and SCT detectors	at least 7 hits
on the pixel detector	at least 2 hits
on the most inner pixel detector	at least 1 hits
Track kinematics	
P_T	> 1 GeV
Impact parameter	
transverse impact parameter $\lvert d_0 \rvert$	< 1 mm
longitudinal impact parameter$\lvert z_0 \rvert$	$\sin\theta < 1.5$ mm
track jet association	
$\Delta R(\text{jet}, \text{track}) = \sqrt{(\eta_{\text{jet}} - \eta_{\text{track}})^2 + (\phi_{\text{jet}} - \phi_{\phi})^2}$	$\Delta R < R$ where R is threshold varied with jet P_T. e.g. R=0.45 for jets with $P_T = 20$ GeV e.g. R=0.25 for jets with $P_T = 150$ GeV

Table 2.7: Track quality requirements for *b*-tagging and association condition with jets

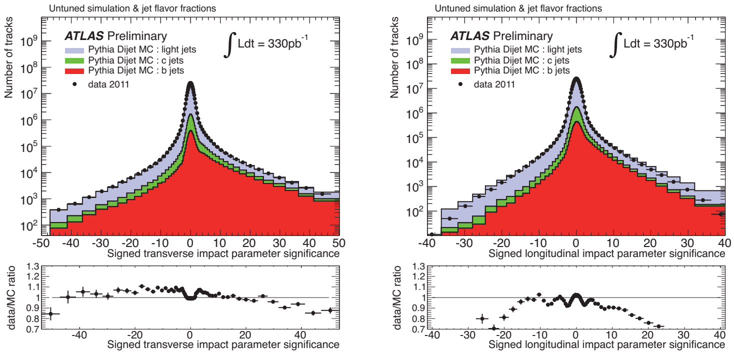

Figure 2.50: Impact parameter significance d_0/σ_{d_0}(left) and z_0/σ_{z_0}(*right*).

pensated by applying scale factors on the simulated events, and left discrepancy is taken into account as systematic uncertainties on the scale factor, as summarized in Table 2.8.

2.4.7 Missing transverse momentum($E_{\mathrm{T}}^{\mathrm{miss}}$)

Neutrinos that do only weak interaction escape the ATLAS detector without leaving any trace, which make apparent non-conservation of momentum. In hadron colliders, thep initial total momentum of colliding partons along beam axis is unknown and its conservation can not be discussed. Meanwhile that on the transverse plane is known and it is zero. Here, missing transverse energy is defined with energy of each visible object projected to $x(y)$-axis as

$$E_{\mathrm{x(y)}}^{\mathrm{miss}} = -\Big(\sum_{e} E_{x(y)} + \sum_{\mu} E_{x(y)} + \sum_{\text{jets}} E_{x(y)} + E_{\mathrm{x(y)}}^{\text{cell-out}} \Big) \tag{2.21}$$

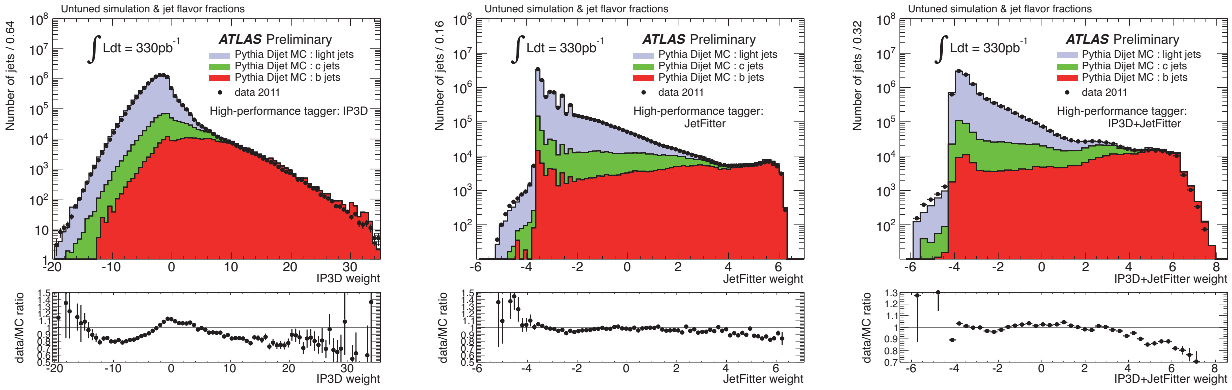

Figure 2.51: The distribution of b-tagging scores for the algorithms to be combined (left and middle), and the one for the combined algorithm(right).

b-tagging efficiency	
P_T (GeV)	Scale Factor
20-30	0.935 ± 0.089
30-60	0.949 ± 0.051
60-90	0.965 ± 0.124
90-140	0.928 ± 0.093
140-200	0.928 ± 0.140

light jet rejection $\|\eta\| < 1.2$		light jet rejection $1.2 < \|\eta\| < 2.5$	
P_T (GeV)	Scale Factor	P_T (GeV)	Scale Factor
20-25	1.075 ± 0.105	20-25	1.075 ± 0.153
25-40	1.057 ± 0.121	25-40	1.210 ± 0.168
40-60	0.997 ± 0.099	40-60	1.060 ± 0.133
60-90	0.964 ± 0.108	60-90	1.047 ± 0.135
90-140	0.947 ± 0.113	90-140	0.952 ± 0.107
140-200	0.926 ± 0.131	140-200	1.024 ± 0.121
200-300	0.926 ± 0.132	200-300	0.986 ± 0.114
300-500	0.957 ± 0.119	300-500	1.087 ± 0.133

Table 2.8: Scale factors for b-tagging efficiency and light jet rejection

where $E_{x(y)}$ is energy projected to $x(y)$ direction of the object. For electrons and muons, only ones that passed the selection in section 2.4.2 and 2.4.3 with isolation criteria in section 2.4.4 are used. For jets, in addition to jets defined in section 2.4.5 jets with $7 < P_T < 25$ GeV are taken into account as soft-jets. The $E_{\mathrm{x(y)}}^{\mathrm{cell-out}}$ is the contribution from cells that forms a cluster but not used as physics jets or soft-jets.

Figure 2.53 shows the distribution of $E_{\mathrm{T}}^{\mathrm{miss}}$ in the data accumulated with a minimum bias trigger, in which most of the events are just QCD interactions . The distribution of data is well modeled by Monte Carlo simulation. Figures 2.54 ,left and right show the width of the $E_{\mathrm{T}}^{\mathrm{miss}}$ distribution with respect to the total sum of transverse energy in the events in data and MC each. Data is taken by the minimum bias trigger here too. In general, the larger transverse energy is, the larger the fluctuation is. Fitting a square root function of the total transverse energy, its coefficient is 0.41 in data and 0.43 in the Monte Carlo simulation.

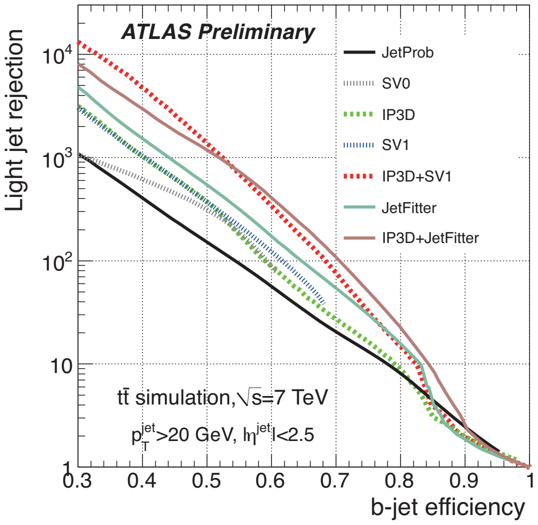

Figure 2.52: The performance of *b*-tagging algorithm. "IP3D+JetFitter" is the one used in this analysis, and "IP3D" and "JetFitter" are the ones to be combined.

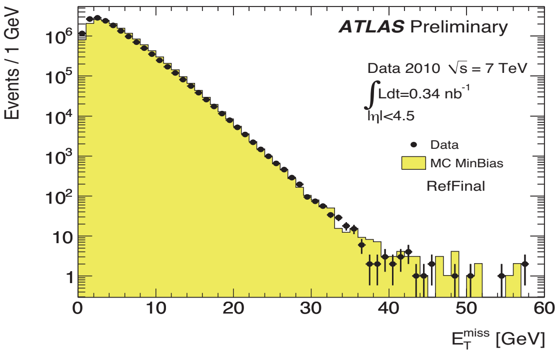

Figure 2.53: E_T^{miss} distribution in minimum bias triggered data. Monte Carlo simulation of color histogram describes the distribution of data well.

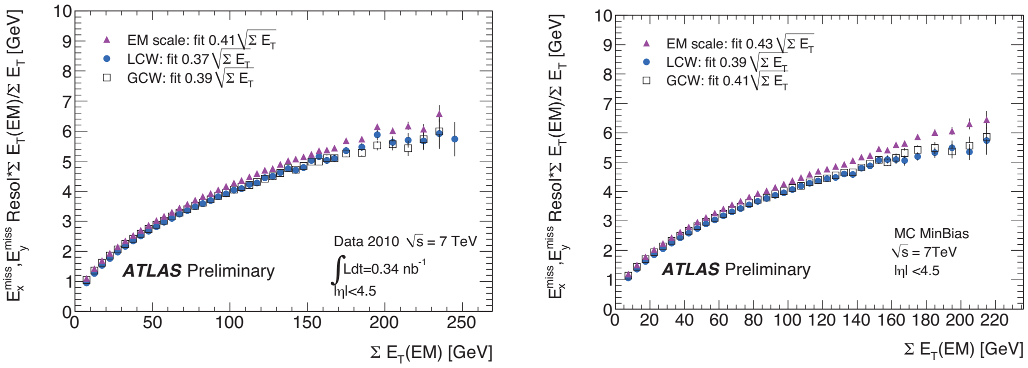

Figure 2.54: The resolution of $E_{\mathrm{T}}^{\mathrm{miss}}$ as a function of sum of transverse energy in the event in data (left) and MC (right).

2.5 Data Acquisition System at ATLAS

2.5.1 ATLAS Trigger System and Lepton Triggers

Efficient data acquisition is the one of the crucial points of experiments. LHC produces proton-proton collisions with high rate of 40 MHz but the most of them are low QCD interaction, which is not interesting from the point of view of top quark physics ; the cross section of the total inelastic scattering calculated with Pythia [33] is 79 mb [34] which is almost 10^9 times larger than the one of the top quark pair of 165 pb. Therefor, it is mandatory to screening events before data recording for the effectual data taking.

The data for the analysis is taken with single electron and muon triggers. The top quark decays that the analysis targets at contain charged leptons in the final state. The signature of such charged leptons can be used to distinguish hard collision events from uninteresting events of low energy QCD interaction.

The trigger system in ATLAS is implemented as three-step decision logic. The first one, called level 1, makes trigger decision on electronic boards within 2.5 micro seconds and reduced event to 75kHz. For electron the electromagnetic calorimeters processes the one for electrons and the RPC and TGC detectors for muons as described in detail later. For the events in which a level 1 trigger fires, the second step trigger, so called level 2, starts to look into the event. In order to achieve both high-speed decision of 40 micro seconds and efficiency, the level 2 trigger system reads out the detector information from only the region around which a level 1 trigger fires. At this step, event rate is reduced to 2 kHz. The final-step trigger, called event filter or EF, perform the similar examination as the level 2 trigger system but with all the detector information within about 4 seconds. Final event record rate is around 200 Hz. Figure 2.55 shows the actual trigger rate in year 2011.

	time	event reduction
Level 1	2.5 μs	40 MHz →75 kHz
Level 2	40 ms	→2kHz
Event Filter	4 s	→∼ 200 Hz

Table 2.9: Designed trigger computation time and event reduction.

Electron trigger

For electron trigger, about 30% of total trigger rate is allocated [36] with electon/γ triggers, and it is optimized within the limitation. The threshold is tuned for electron with $E_T > 14$ GeV, and the level 2 and event filter are for ones with $E_T > 20$ GeV.

The electron level 1 trigger algorithm searches peaks of energy deposit in the calorimeter towers defined as $\Delta\eta \times \Delta\phi = 0.1 \times 0.1$ blocks in the EM and hadron calorimeters as Figure 2.56. And the sum of energy deposits on 2×2 towers are required to be local maximum in the EM and hadron calorimeter each, and to pass an E_T threshold.

The electron level 2 trigger performs energy clustering and track matching to the cluster. It is seeded by the level 1 trigger, and it receives η and ϕ information where the level 1 triggers fire, and

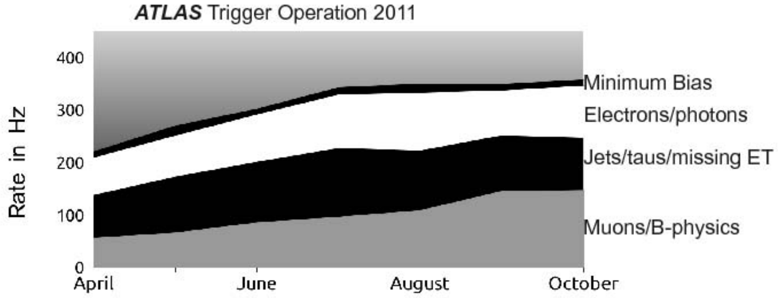

Figure 2.55: Actual trigger rate of triggers and total in the year 2011 [35]

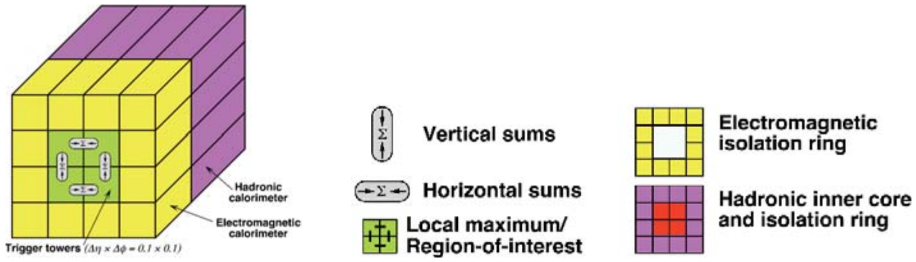

Figure 2.56: An illustration of calorimeter tower for the electron level 1 trigger.

retrieve detector information in $\Delta\eta\times\Delta\phi = 0.4\times0.4$ around it. In this step, the clustering is performed in the second layer of the EM calorimeter with full granularity of the detector. The cell with the highest E_T and others in $3\times7(\Delta\eta\times\Delta\phi = 0.075\times0.175)$ in $|\eta| < 1.4$ and in $5\times7(\Delta\eta\times\Delta\phi = 0.125\times0.175)$ in $1.4 < |\eta| < 2.47$ around the cell forms a cluster. The level 2 trigger decision uses energy deposit in hadron calorimeter, shower shape in η direction and energy deposit ratio E_{ratio} like offline electron identification in the section 2.4.2. Also tracking in the inner detector in the corresponding region is performed. Unlike offline tracking as summarized in the section 2.4.1, only inside-out tracking is performed to keep the algorithm fast.

In the event filter, the same reconstruction algorithm is performed in the region, and variables as listed in the section 2.4.2 are used.

Figure 2.57 shows the trigger efficiency evaluated by the tag-and-probe method (section 2.4.2) taking into account the systematic uncertainties coming from the requirement of identification of tag electron, and selection of Z mass window. More detail is summarized in [36] [3].

Muon trigger

The muon trigger used in this analysis is the one of which level 1 is tuned for muons of $P_T > 10$ GeV, and level 2 and EF for ones of $P_T > 18$ GeV [4].

---

[3] In the reference, the trigger used in this analysis is labeled as *e20_medium*.

[4] The trigger is called *mu18_medium*. More detain including its naming schema is summarized in [37].

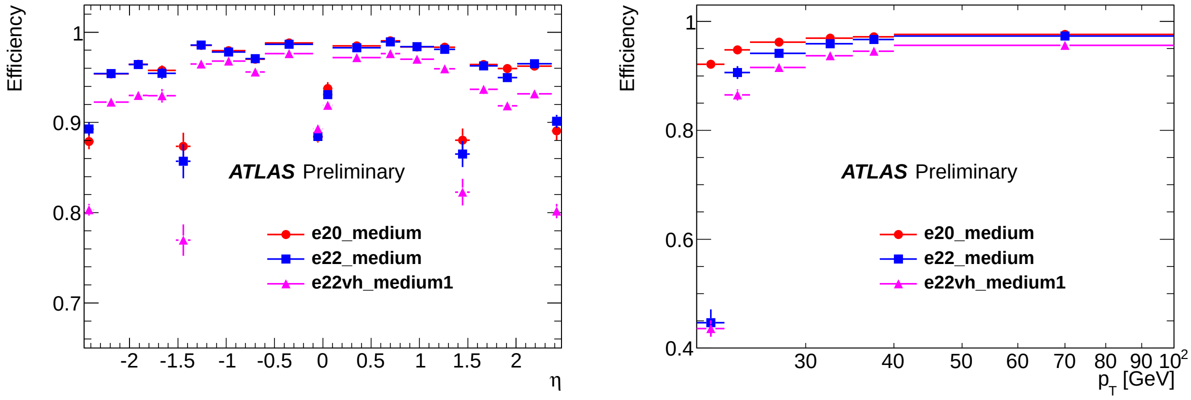

Figure 2.57: Electron trigger efficiency with respect to reconstructed electrons as a function of η(left) and E_T(right). The one labeled as *e20_medium* is the one used in this analysis.

Muon level 1 trigger is fired by the RPC and TGC detectors with logic implemented on hardware. The RPC three layers are allocated so that the first and third layers surround the toroidal magnets, and they detect muons passing through the magnetic field with being bent. The RPC measures P_T of the track from the curvature. Meanwhile, the TGC three layers are allocated outside of the magnet and detect muons after passing through the magnetic field. The TGC measures P_T of muons from displacement of the trajectory from an imaginary track of infinite momentum muon which passes the same point on the third layer.

The muon level 2 algorithm retrieves MDT hit information around the level 1 trigger. It performs fast tracking, and calculates the muon P_T based on look up table. And it associates the track with ones reconstructed with the inner detector, and checks if the momentum of the combined track passes the P_T threshold.

In the muon EF, the same track reconstruction is performed in the level 2 trigger region. Tracks reconstructed by muon detector is extrapolated to the interaction point and muon track parameter there is obtained. At this step, track matching between tracks at the muon detector and inner detector is performed in both way, inside-out and outside-in, in parallel.

Trigger efficiency scale factor

The difference between data and the Monte Carlo simulation is compensated by applying scale factors $\mathrm{SF}_{\mathrm{event}}$ on the simulated event. Since the signal of this analysis $t\bar{t} \to W^+bW^-\bar{b} \to l^+\bar{\nu}bl^-\nu\bar{b}$ has two charged leptons, the scale factor for each event is the products of the scale factors for each charged lepton. The scale factor for di-electron event is the product of the trigger scale factors for each electron :

$$\mathrm{SF}_{\mathrm{event}} = \mathrm{SF}^{e1}(\eta) \times \mathrm{SF}^{e2}(\eta) \qquad \text{(The trigger fired for both electrons.)} \tag{2.22}$$

$$\mathrm{SF}_{\mathrm{event}} = \mathrm{SF}^{e1}(\eta) \times \frac{1 - \mathrm{eff}_{\mathrm{data}}}{1 - \mathrm{eff}_{\mathrm{MC}}} \qquad \text{(The trigger fired only for electron 1.)} \tag{2.23}$$

where $\mathrm{SF}^{e1,2} \equiv \mathrm{eff}^{e1,2}_{\mathrm{data}}/\mathrm{eff}^{e1,2}_{\mathrm{MC}}$ is the scale factor, and $\mathrm{eff}^{e1,2}_{\mathrm{data,MC}}$ is the trigger efficiency in data and the Monte Carlo simulation.

The muon trigger matching does not work is Monte Carlo simulation due to a mere technical issue, and muon trigger matching is not required in Monte Carlo. Instead, the scale factor for muon is defined so that the event is re-weighted by muon trigger efficiency in data. In di-muon channel, the scale factor for an event is

$$\mathrm{SF}_{\mathrm{event}} = \mathrm{eff}^{\mu_1}(P_{T,1}, \eta_1, \phi_1) \times \mathrm{eff}^{\mu_2}(P_{T,2}, \eta_2, \phi_2). \tag{2.24}$$

The data for the analysis in the $e\mu$ channel are taken with both the single electron and the muon triggers. The scale factor for the simulated events in which the electron triggers fires (regardless of the muon trigger) is

$$\mathrm{SF}_{\mathrm{event}} = SF^{\mathrm{electron}}(\eta). \tag{2.25}$$

For the other events in which the electron triggers does not fire but the muon trigger does, the scale factor is the product of the one for the efficiency of the muon trigger and the one for the inefficiency of the electron trigger :

$$\mathrm{SF}_{\mathrm{event}} = \mathrm{eff}^{\mu}_{\mathrm{data}} \times \frac{1 - \mathrm{eff}^{\mathrm{electron}}_{\mathrm{data}}}{1 - \mathrm{eff}^{\mathrm{electron}}_{\mathrm{MC}}}. \tag{2.26}$$

2.6 Luminosity measurement

Measurement of luminosity $\mathcal{L}$ can be done from the number of a particular “visible”(detectable) events μ_{vis} with its cross section σ_{vis}.

$$\mathcal{L} = \frac{\mu_{\mathrm{vis}} n_b f_r}{\sigma_{\mathrm{vis}}} \tag{2.27}$$

where n_b is the number of colliding bunches on the ring and f_r is the machine revolution frequency. The cross section is the total inelastic scattering multiplied by the efficiency of detectors and method : $\sigma_{\mathrm{vis}} = \epsilon\sigma_{inelastic}$.

The ATLAS detector has two sub-detectors for the luminosity measurement, namely LUCID [38] and BCM [39]. The LUCID (LUminosity measurement using a Cherenkov Integrating Detector) is a Cherenkov detector with C_4H_{10} gas, installed at ±17m away from the interaction point covering $5.6 < |\eta| < 6.0$ with 16 tubes in each side. The Cherenkov photons are read out by photo multiplier tubes. It is installed as Figure 2.58 shows. The BCM(Beam Condition Monitor) is four diamond sensors allocated in both side of $|\eta| = 4.2$, as Figure 2.59 shows.

The evaluation of the efficiency ϵ is done by providing proton collisions with known luminosity. It is possible with the *van der Meer*(vdM) scan. The absolute luminosity is given, by the definition, as

$$\mathcal{L} = \frac{n_b f_r n_1 n_2}{2\pi\Sigma_1\Sigma_2}. \tag{2.28}$$

where $n_{1,2}$ are the number of protons in a bunch, and Σ_x and Σ_y are the beam width in x and y direction assuming the Gaussian distribution. The vdM scan moves one of the bam in the horizontal or vertical

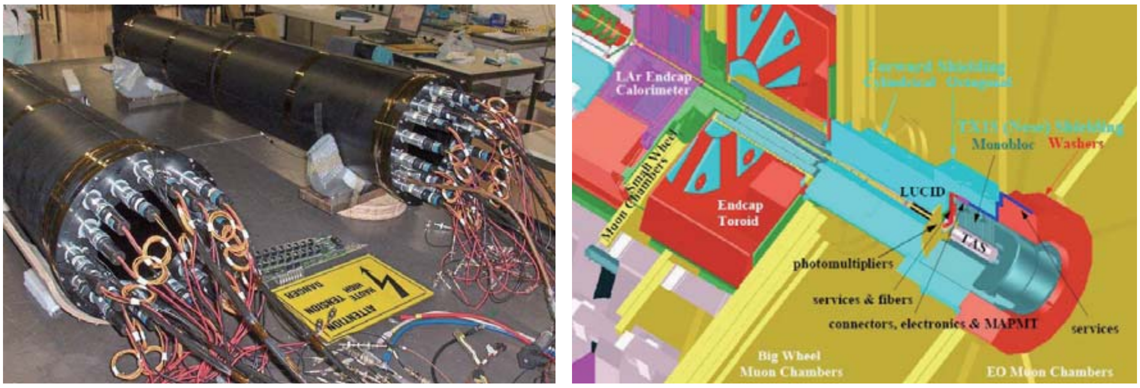

Figure 2.58: (left) The LUCID detector module for each side. (right) The allocation of the LUCID detector.

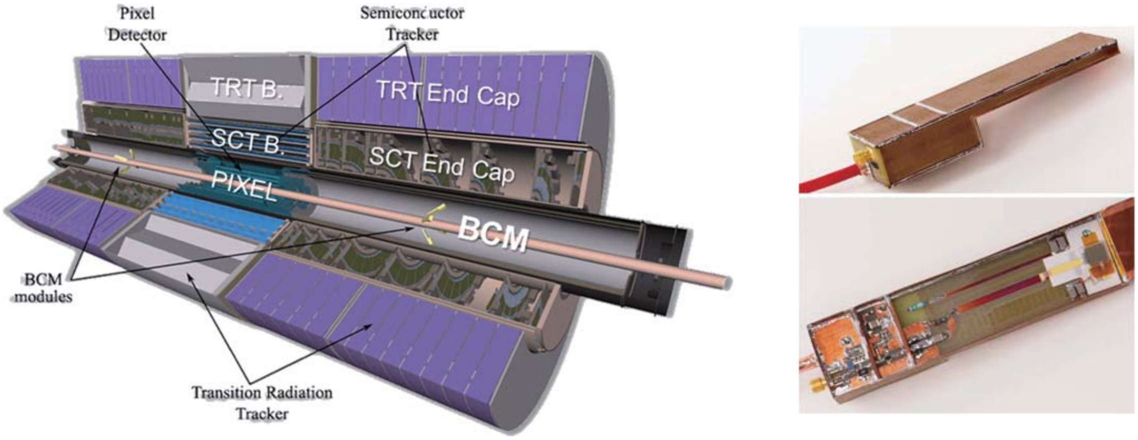

Figure 2.59: (left)The allocation of the BCM detector. (right) One module of the BCM diamond detector.

direction and evaluate the beam width Σ_x and Σ_y from the position dependence of the luminosity as Figure 2.60. By measuring the beam population $n_{1,2}$, the beam collision with known luminosity is provided and the efficiency can be evaluated.

The main uncertainties on the calibration with the vdM scan comes from the beam population measurements during the dvM scan (3.0%), the dependence on the fitting function of the vdM scan data (0.8%) and the discrepancy of the calibration result during the calibration period between the horizontal and vertical BCM detectors (0.7%). Also long term consistensy during the data taking and pile-up effect dependence between the detectors (1.0% each) are taken into accout, the total uncertainty of the luminosity of the data is 3.7% [40].

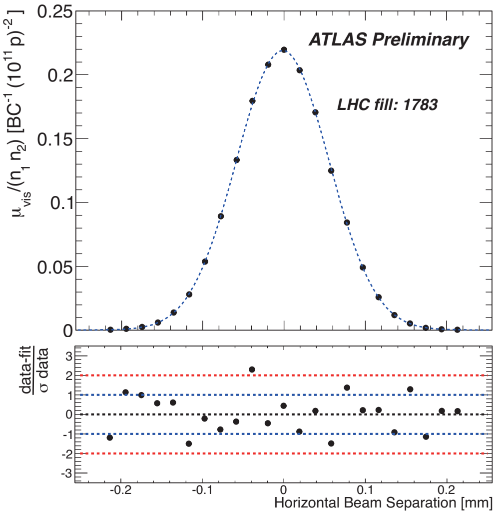

Figure 2.60: One result of the vdM scan in the horizontal direction [40].

Chapter 3

Muon detector commissioning and its performance evaluation

3.1 The TGC detector commissioning

3.1.1 The TGC detector system overview

The TGC muon trigger system consists of gas detectors called Thin Gap Chambers. The chamber is designed similar to a multi-wire proportional chamber as shown in Figure 3.1. and it has gold-plated tungsten wires in the mixture gas of CO_2:n-pentane=55:45. Its wire anode pitch is 1.4 mm and the distance of wire-cathodes is 1.8 mm. The cathod strip layers are allocated orthogonal to the wires. The output signal is immediately digitized with an amplifier-shaper-digitizer which is implemented on each chamber.

The chambers are aligned radially and forms discs with a diameter of 25m as Figure 3.2 shows, so that the wire channels have sensitivity to η position and the strip to ϕ. Several anode wires are grouped together (4-20 wires per one channel) and fed to a common readout channel, so that the coverage of one channel is almost consistent in η. Three discs are allocated at $|z| = 13, 14$ and 14.5m and they are called station-1, -2 and -3 respectively. The station-1 consists of three-layer chambers(triplet) and others use two-layer chambers(doublet) with structures shown in Figure 3.3.

Their allocation is after the calorimeter as shown in Figure 3.4. Due to the large radiation- and interaction-length of the calorimeter, charged particles that reached at the TGC can be identified as muon. The TGC system covers $1.05 < |\eta| < 2.4$ for trigger and up to $|\eta| = 2.7$ for detection (TGC provides hit information for tracking).

Between the calorimeter and the TGC chambers, there are toroidal magnets. Muons reach at the TGC chamber after being bent by the Lorentz force. As Figure 3.4 shows, the TGC system measures the muon transverse momentum by comparing the detected track trajectory to a virtual track of infinite momentum (which draws a straight line) from the interaction point to the hit position on the station-3. And it makes trigger decision of six-staged based on the momentum.

The trigger decision is made in three steps, as illustrated in Figure 3.5. First, it requires coincidental hits on the station-2 and -3, in the wire and strip channels separately. If the coincidence is satisfied, second coincidental hit with on the station-1 with respect to the hit on the station-3 is searched. If the second coincidence is also satisfied, finally, coincidental hits between the wire and strip channel

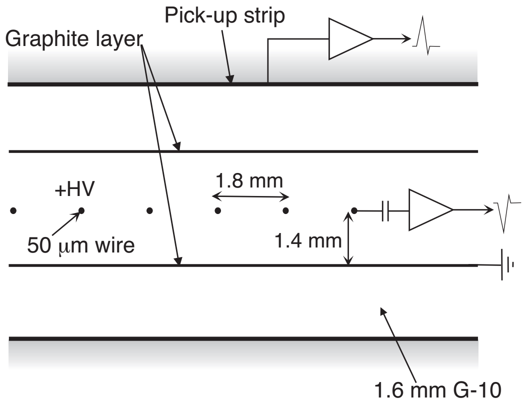

Figure 3.1: The geometry of the wires and strip inside the chamber.

is required.

The first and the second logic are implemented with hardware, mainly with ASICs. They search coincidental hits within some region on station-2 or -1, around the hit on the station-3. Meanwhile, the third logic is implemented on FPGAs so that the P_T requirements can be modified flexibly according to the experimental conditions. The logic receives the hit position on the station-3 and the difference between station-1 and -3. Due to the complexity of the toroidal magnetic field as shown in Figure 2.28, the correlation between muon momentum and expected input is not straightforward. Therefore, the correlation is studied with the Monte Carlo simulation first, and the correlation is prepared as a look-up table (LUT). The LUT is loaded on to the FPGAs on the third trigger logic and the trigger decision is made based on it.

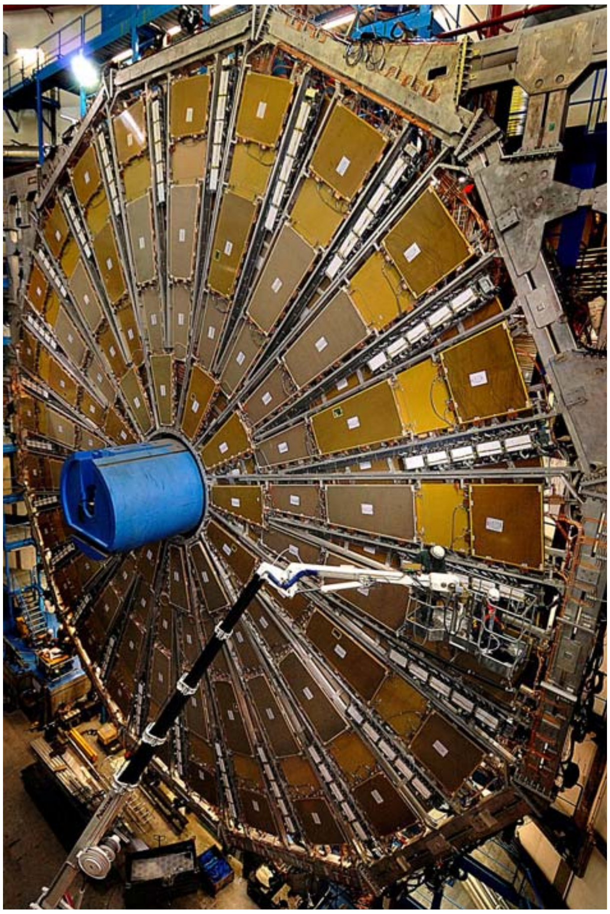

Figure 3.2: A picture of the TGC detector. The gas chambers are aligned radially and form a wheel. The three stations are placed in the both side of the ATLAS detector.

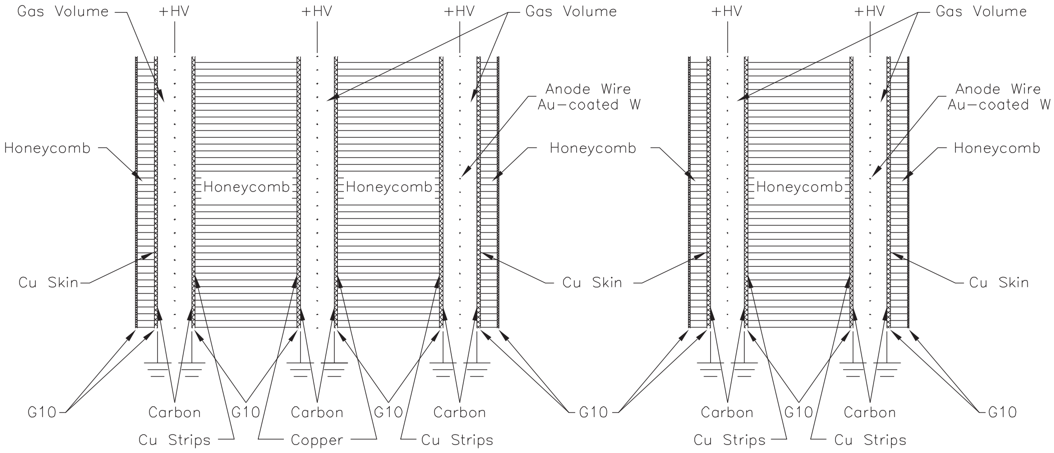

Figure 3.3: The cross section of the triplet(left) and doublet(right) chambers.

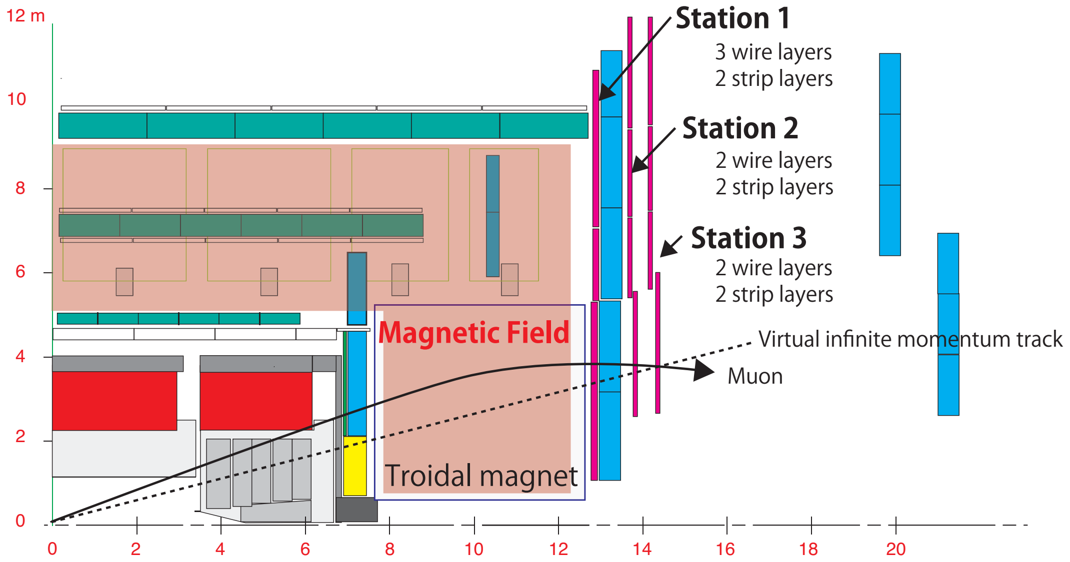

Figure 3.4: The position of the TGC detectors and naming. The three stations of TGC are aligned just after the toroidal magnet. They are called station-1,2,3 from inside. The station-1 consist of triplet chambers, and station-2 and -3 of the doublet. In total TGC has 7 wire and 6 strip layers.

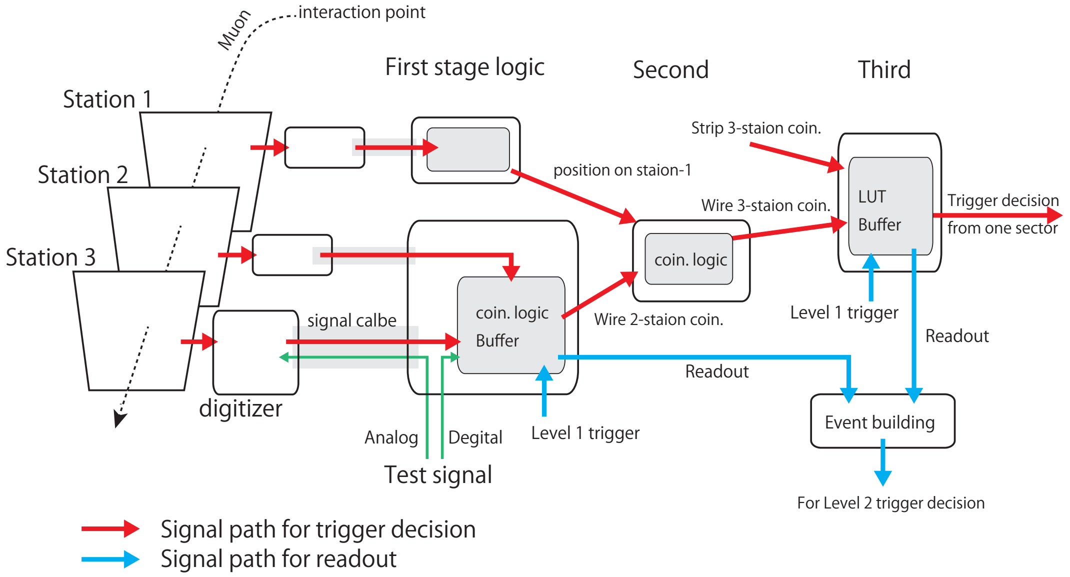

Figure 3.5: Overview of the TGC trigger logic flow. The output from the chambers are immediately digitized and sent to the first stage logic via signal cable. The three logic check the coincidence between station 2-3, station 1-3 and wire-strip successively. In the third stage, a look up table(LUT) is used for fast trigger decision. For the event in which level 1 trigger fires, the hit and trigger decision information is readout from buffer. The system has two types of test pulse functionality to emulate digitized signal input and chamber analog signal.

3.1.2 The calibration scheme for long term running

After the hardware installation of 1200 electronics and 12000 cables, the functionality of all the hardware is needed to be confirmed. It is confirmed step-by-step from downstream to upstream with two types of test signals. The digital part, which has responsibility to all the output of trigger and readout, is established. The one of the test signal can insert digitized signal just in front of the first logic, as shown in Figure 3.5 and it is possible to mimic high energy track signals by inserting appropriate hit pattern on the TGC seven layers. With the test signal, the functionality of the electronics and connection between them is verified by comparing the trigger output and readout hit pattern. The system of this part is synchronized with 40MHz clock from the LHC. With the test signal, the phase of the signal between the electronics is tuned simultaneously. Another test signal emulates the chamber output and inserts the charge signal just before the amplifier as indicated in Figure 3.5, with which the functionality of the amplifier, shaper and discriminator on each chamber is verified. After these electronics establishment, random trigger data taking is periodically done to track down noisy channels with occupancy of $>10^{-5}$ with respect to usual "calm" channels of occupancy less than 10^{-6}. For these channels, the higher threshold of the discriminator is applied or local hot channels are masked off from trigger decision or readout.

These tests established in the commissioning is summarized as a set of daily calibration data taking during stand-by time between physics data taking.

3.1.3 The commissioning with cosmic data taking

After the confirmation of the electronics functionality, the cosmic lay data taking is done. The charged particles in cosmic lays, mainly muons, are useful for the verification of the detector response.

Even after the system establishment with the test signals as summarized in section 3.1.2, two types of improper cable connection may remain. Figure 3.6 shows one cable connection point on a doublet chamber. Two sockets in the picture correspond to two layers (triplet chambers has three sockets), and the hit information of 16 channels of one layer is read out from one socket. One type of improper connections is swapping of the cables between connection points, which results in swapping of channels in the unit of 16 channels. This can be verified from correlation between stations. Figure 3.7 (left) shows an example of the hit position correlation between the station-2 and -3 in a certain region, in which a clear signature of cable swap is seen. The swap in this section is confirmed on site and fixed. Figure 3.7 (right) shows the hit correlation in the same region after the correction.

The other type of the cable swap is wrong connections between layers at the same connection point. This can not be verified by the hit correlation among stations since the physical displacement is relatively small. Instead, this can be seen as correlation between the layers in the same chamber. In a chamber, the channels are aligned with staggered between layers, in order to maximize the position resolution in the trigger logic, as Figure 3.8 shows. Since cosmic lays penetrating chambers are expected to leave hits on the neighboring channels on the two layers(or three layers in the triplet chambers), that is the channel number of the hit on layer 5 or 7 is the same or larger by one compared to that on layer 4 or 6 (the situation is similar in the triplet chambers). Figure 3.9 shows the channel differences (Δ ch) between two layers with proper and improper cable connections. In the former, most entries are seen in -1 and 0, while in the later, mainly in 0 and 1.

With the cosmic data taking, the all the cablings are verified, and more than 70 improper cablings

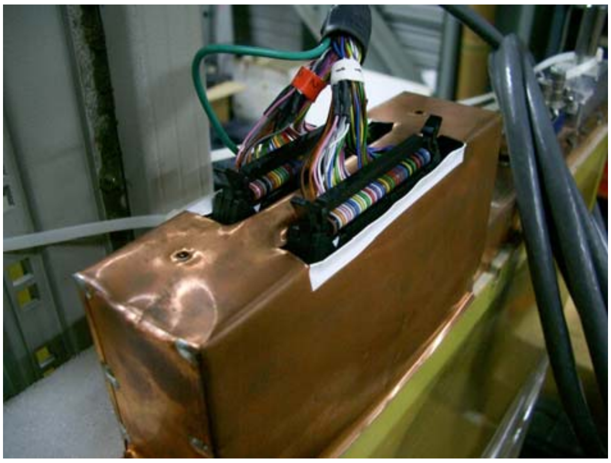

Figure 3.6: The cable connection point on the chamber side. The output from the two(or three) layers are read out from the same point, with the same readout interface. Here improper connection can happen.

(%)	side $\eta > 0$	side $\eta < 0$
layer 4	91.7 ± 0.1	91.2 ± 0.1
layer 5	93.1 ± 0.1	92.4 ± 0.1
layer 6	94.7 ± 0.1	93.9 ± 0.1
layer 7	91.9 ± 0.1	90.3 ± 0.1

Table 3.1: The mean of the chamber efficiency on the each layer, each side. Only statistical uncertainty is taken into account.

are identified and fixed. Only one wrong cabling between layers in one triplet chamber is left due to difficulty of the access, which is found to be small impact.

The detection efficiency of the chambers is evaluated with cosmic data. Since the TGC itself is the trigger detector, the trigger bias for the evaluation is need to be removed. The TGC trigger logic requires at least three layers out of the four in the station-2 and -3 to have hits. The efficiency of a certain layer is evaluated by requiring such hits on the other layers and checking if the layer has a hit. Figure 3.10 shows the efficiency map of the layer 6 in the $\eta < 0$ side, and Table 3.1 summarizes the mean efficiency on the each chamber. Compared to the chambers nominal efficiency of 92% taking into account inactive region of the chambers, these values are quite reasonable. These activities are summarized in the reference [38].

3.1.4 Optimization of the TGC trigger logic based on data

In the TGC trigger performance study, some events, in which the TGC trigger did not fire with respect to high P_T muons that left hits on the chambers, are found. Figure 3.11 (left) shows an illustration of the recorded hit positions on the strip layers by one high P_T muon and no TGC trigger fires for the muon.

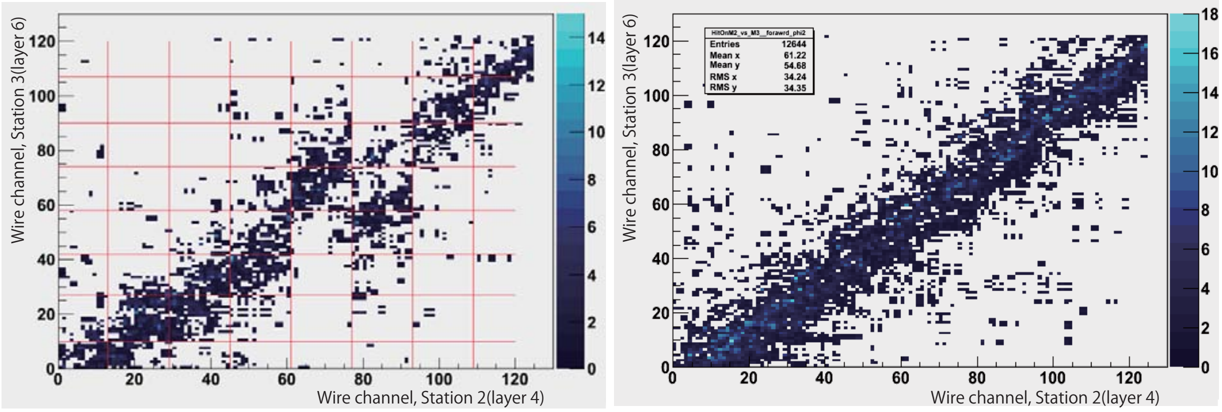

Figure 3.7: Cosmic hit correlation of wire channels between in station 2 and 3. (left) Correlation in the early period of cosmic data taking. The grids correspond to the units of the read out cabling. In the linear correlation, clear discontinuities are seen, which correspond to the unit of digitizer in the station-2. (right) The correlation in the cosmic data taken after fixation of the cable improper connection.

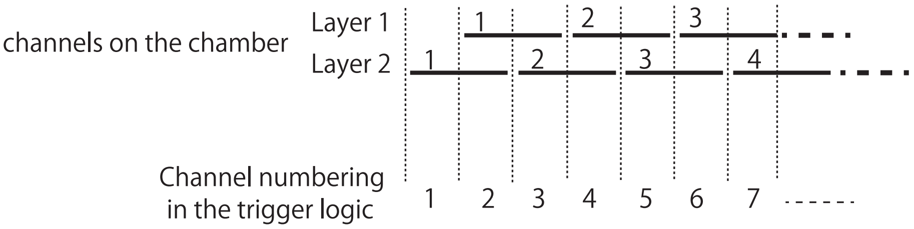

Figure 3.8: In the chamber, the channels in different layers are aligned with staggered each other in order to maximize the resolution, and a half of one physical channel size corresponds to one channel in the trigger logic.

It is discovered that a treatment rule of multiple hits in the TGC trigger logic produces this apparent inefficiency. As mentioned in section 3.1.1, the 3-station coincidence requires coincidence between the first and third station, in addition to the 2-station coincidence. The third trigger logic use the inputs of positions and channel difference Δch in the wire and strip readout, and fires a trigger only if the input is matched to the prepared LUT. The trigger logic treats successive hits as one cluster caused by one charged particle, and select only one hit of them based on some rule called de-clustering. As Figure 3.11(right) shows, the rule always takes the second channel from one side. As the result, the resolution of the channel position, and equivalently, that of Δch is worsen. No cross-talk between channels considered in the Monte Carlo simulation, while, it is not negligible in the strip channels in reality.

In the muon event shown above, the Δch for wire is 8 and for strip is 0 if only the reasonable hits are taken into accout, while it is -2 due to the de-clustering rule. Figure 3.12 shows the LUT for the muon event, and the inout of $\{\Delta ch^{\text{wire}}, \Delta ch^{\text{strip}}\} = \{8, 0\}$ correspinds to a trigger of threshold $P_T = 15$ GeV, while no trigger fires for $\{8, -2\}$.

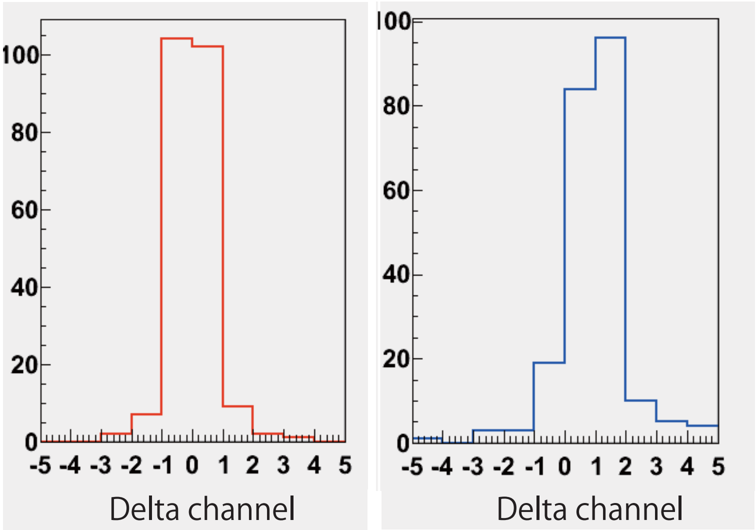

Figure 3.9: The channel distribution obtained in the chamber with proper and improper cable connection in the accumulated cosmic data. (left) In the case of proper connection, Δ ch is expected to to be -1 or 0. (right) In the case of improper connection, Δ ch is expected to to be 1 or 0.

As one fast and straightforward cure, loosening the trigger condition in the strip channel on the LUT is performed. With respect to muons for which the 2-station triggers fire, the gain by loosing the condition on the strip hit from the point of view of the 3-station trigger efficiency is investigated. Muons with $P_T > 10$ GeV are used in the following discussion, whose 3-station trigger efficiency with respect to 2-station trigger is confirmed to reaches at plateau. Figure 3.13 shows the relative efficiency of the 3-station trigger to the that of the 2-station under the various requirements on the strip Δch, out of all 46,500 muons with $P_T > 10$ GeV with the 2-station trigger. In the data, the 3-station trigger fires for 91.0% of them. If condition of the strip is completely removed, the relative efficiency is recovered to 97.9%. Even by loosening the condition by 1 channel (widen the LUT map in the strip channel), it recovers to 94.9%.

In a balance of the trigger efficiency and increase of trigger rate due to the loosening, new LUT with widen the map by 2 channels in the strip by hand is prepared and implemented for data taking. In parallel, the cross-talk in the strip channels is implemented in the Monte Carlo simulation by tuning random cross-talk to the next channels so that the simulation matches to the data.

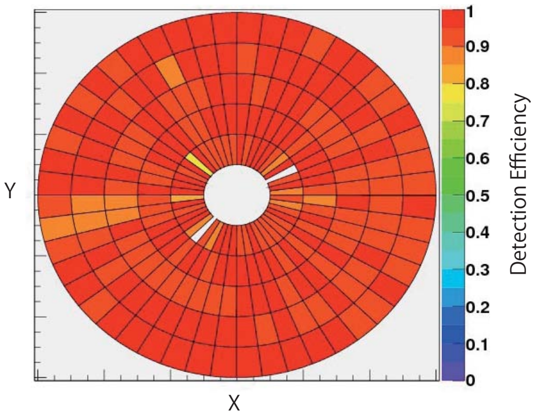

Figure 3.10: The evaluated chamber detection efficiency from cosmic data, in the side where $\eta < 0$, layer 6 on the station 3. The axes are not the scale. Two white chambers are missing due to problems due to applying high voltages.

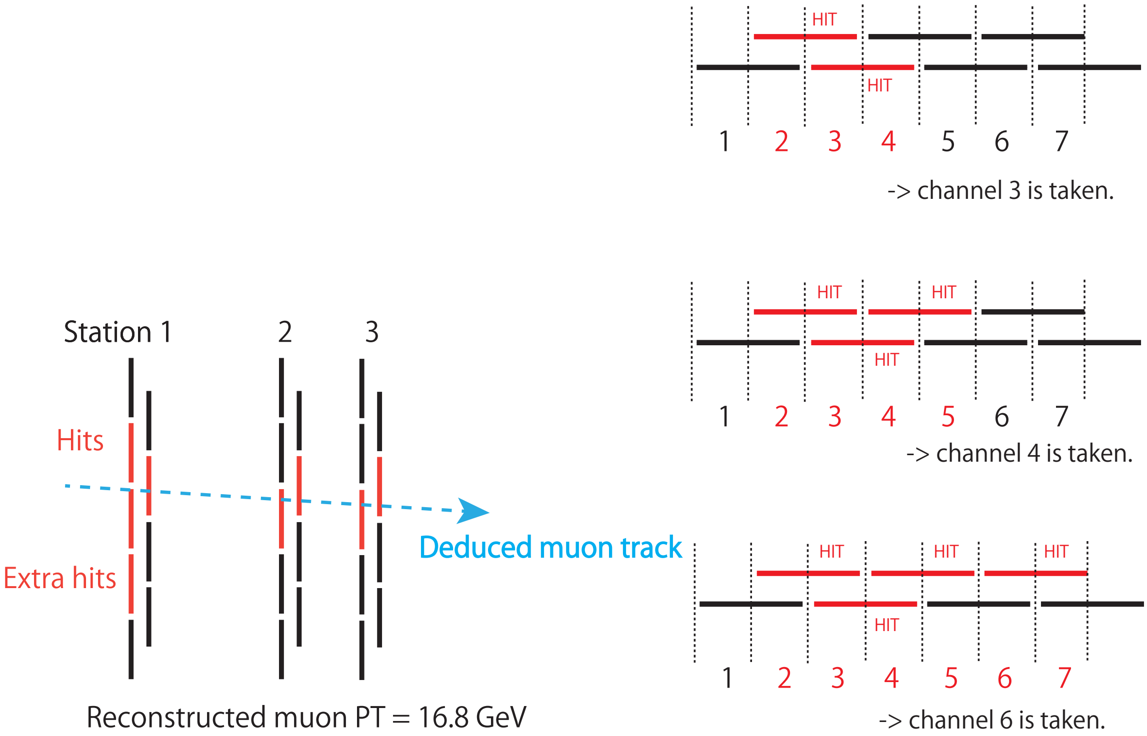

Figure 3.11: (left) An illustration of strip hit positions for one muon passing event, for which any TGC trigger has not fired. In this event, multiple hits on the layer 1 is seen, which preventes the 3-station trigger coincidence. (right) The handling rule of successive hits takes the second channel from one side.

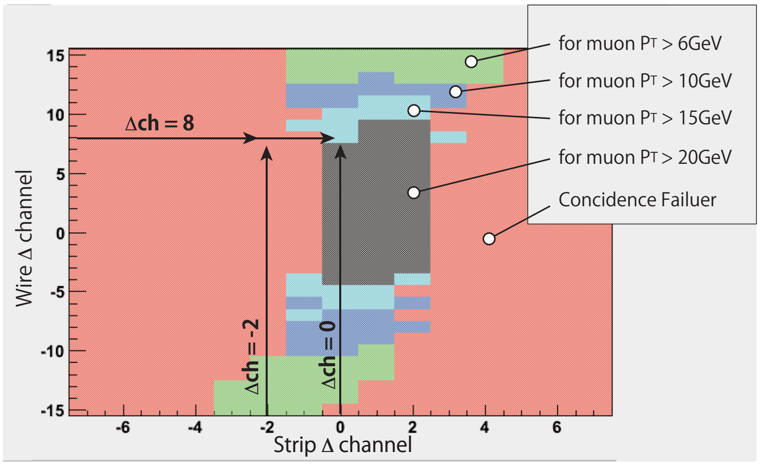

Figure 3.12: The LUT for the event under discussion. The Δch for wire is 8 and that for strip is -2, which result in the coincidence failure. If the extra would not had existed, the Δch for strip is 0 and a 3-station trigger fires.

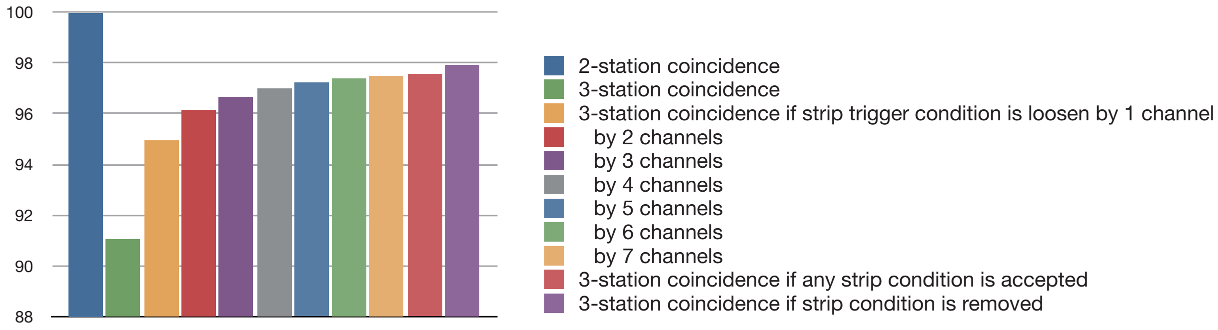

Figure 3.13: The relative efficiency(%) of 3-station trigger logic with each condition to the muons for which the 2-station trigger fired.

3.2 The ATLAS muon detector performance

3.2.1 Evaluation of muon momentum scale and resolutions

The performance of the muon reconstruction is examined in the early phase of data taking of year 2010. The energy scale and resolution of the reconstructed muon in data is compared to the Monte Carlo simulation based on reconstructed Z boson events.

Muon candidates are required to be $P_T > 20$ GeV, $|\eta| < 2.5$, isolation , but without detail requirements on the number of hits on each detectors. The trigger is one that is optimized for muons with $P_T > 13$ GeV seeded by Level 1 muon trigger for ones with $P_T > 10$ GeV.

Figure 3.14 shows reconstructed di-muon invariant mass in data and Monte Carlo simulation. The peak near 90 GeV corresponds to the Z boson events. It is clear that almost no background is expected in this region. The leading contribution is the signal $Z \to \mu\mu$ and, the second contributions is di-boson in which one Z boson decays into a di-muon. Therefore in this study, background can be ignored at the statistics of this stage. In the analysis, only $Z \to \mu\mu$ Monte Carlo simulation is used.

Reconstructed Z boson mass is evaluated by a function F(x) of a Breit-Wigner function(BW) convoluted by the Crystal Ball function(CB),

$$F(x) = N \int \mathrm{d}x' \mathrm{BW}(m_z, \Gamma_Z = 2.4952\mathrm{GeV} : x') \cdot \mathrm{CB}(N = 1, \alpha, n, \bar{x} = m_z, : \sigma; x) \tag{3.1}$$

where m_Z corresponds to the Z mass peak, Γ_Z for the Z width, which is fixed to be 2.4952 GeV in this

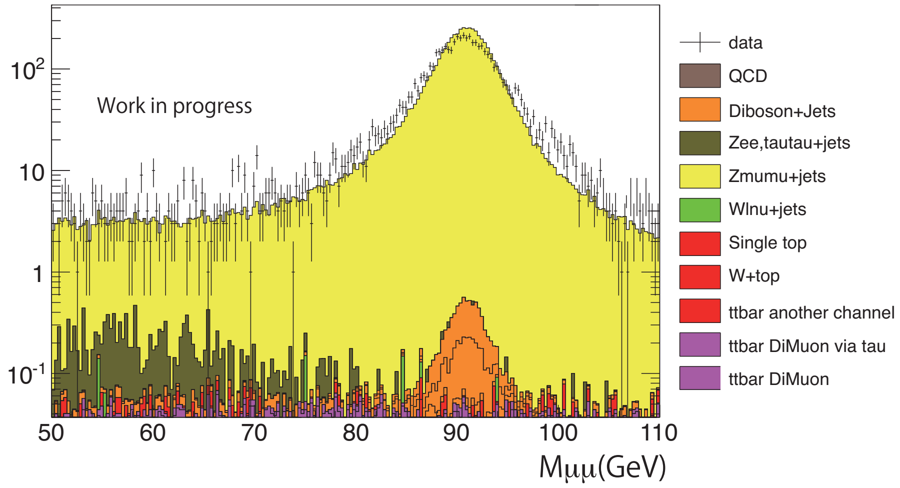

Figure 3.14: Invariant mass distribution of di-muon events in the data in 2010 comparing to the Monte Carlo simulation without any modification based on data. Most of the entries around the Z boson mass peak around 91 GeV is from Drell-Yan(labeled as “Zmumu+jets”) and Di-boson of which one Z boson decays into di-muon.

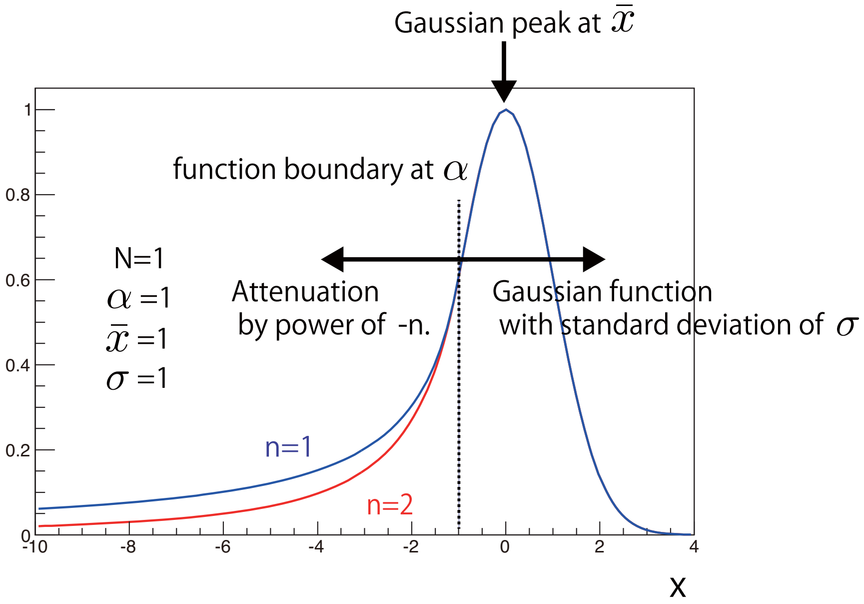

Figure 3.15: An illustration of the Crystal Ball function with $N = 1, \alpha = 1, \bar{x} = 1, \sigma = 1, n = 1$ and 2 . N determines the height, α position of function boundary, $\bar{x}$ Gaussian peak position, σ standard deviation of the Gaussian function and n the attenuation power in the left side region.

function. The CB is defined as

$$\mathrm{CB}(N, \alpha, n, \bar{x}, : \sigma, x) = \begin{cases} N \cdot \exp\left(\frac{(x-\bar{x})^2}{2\sigma^2}\right) & (\text{for}(x-\bar{x})/\sigma > -\alpha) \\ N \cdot A \cdot (B - \frac{x-\bar{x}}{\sigma})^{-n} & (\text{for}(x-\bar{x})/\sigma \leq -\alpha) \end{cases} \tag{3.2}$$

where

$$A = \left(\frac{n}{|\alpha|}\right)^n \cdot \exp\left(-\frac{\alpha^2}{2}\right)$$
$$B = \frac{n}{|\alpha|} - |\alpha|$$

and N determines the height, α position of function boundary, $\bar{x}$ Gaussian peak position, σ standard deviation of the Gaussian function and n the attenuation power in the left side region. Figure 3.15 shows examples of the function and how the parameters work. The CB function is empirically known that the function describes the long tail in the left side of the invariant mass distribution due to final state radiation of the lepton. In the convolution function, m_Z can be regarded as the peak position of the Z mass peak and σ as the resolution of the reconstructed peak.

The detector region is devided into two : barrel where $|\eta| < 1.05$ and endcap where $1.05 < |\eta| < 2.5$, and events are categorized , based on the direction of two muons, into Barrel-Barrel(BB), Barrel-Endcap(BE) and Endcap-Endcap(EE) events.

Figure 3.16 is obtained di-muon invariant mass distribution in the early data for each event category, showing the clear Z mass peak with slightly smeared. Figure 3.17 is the counterpart of the latter

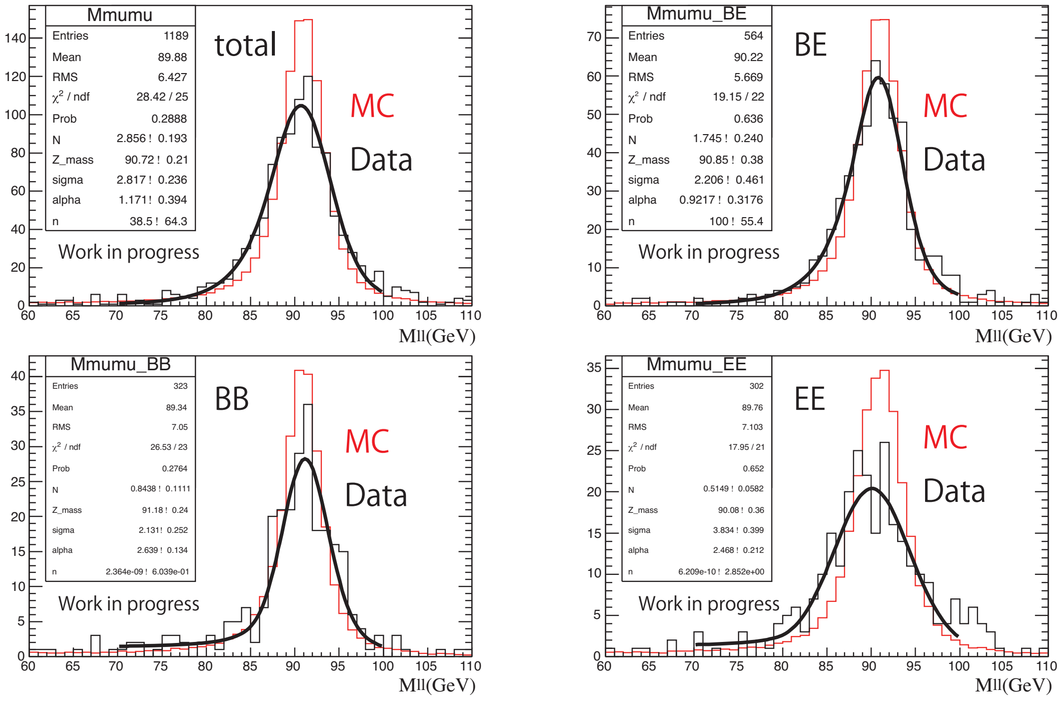

Figure 3.16: Di-muon invariant mass distribution in the early data. Black histogram is data, and red is Monte Carlo simulation scaled with the number of entries of data. (top left) total, (top right) BE, (bottom left) BB and (bottom right) EE events.

data. Table 3.2 summarizes the parameter σ as the results of fitting in the two periods. In BB and EE events, the resolution is improved after the update of the alignment parameter. Although it is not clear in BE event due to low statistics, the improvement is clear in the total.

The Monte Carlo simulation is compared to data by scaling and smearing the muon momentum reconstructed in the simulation. The modification is following a function defined as

$$\frac{1}{P_{T,\text{ modified}}} = \frac{1}{P_{T,\text{ MC}} \times C} Gaus(1, \sigma_{\text{extra}}) \tag{3.3}$$

where the function $Gaus(1, \sigma_{\text{extra}})$ returns one random number following a Gaussian with mean of 1 and standard deviation of σ_{extra}, C corresponds to scale factor and σ_{extra} to the index of worsen resolution.

The m_Z and σ in the fitting function for the simulation is compared to data, by scanning the parameter C and σ_{extra}, as Figure 3.18(left) shows. Comparing the data and scale factor dependence of m_Z with linear approximation, the scale factor C is decided as Table 3.3. It is seen that the scale factors lay close to 1. Also, it is seen that applying the update of the alignment parameter, the improvement of the situation in EE events.

In the σ_{extra} scan, Figure 3.18(right), a quadratic dependence of σ on σ_{extra} is seen. And compared the result to the data, it is clear that non-zero extra smearing is needed. Table 3.4 summarizes the required extra smearing calculated from data and linear approximation of σ dependence on σ_{extra}. First of all, even after updating the alignment parameters, extra smearing seems to be needed. And

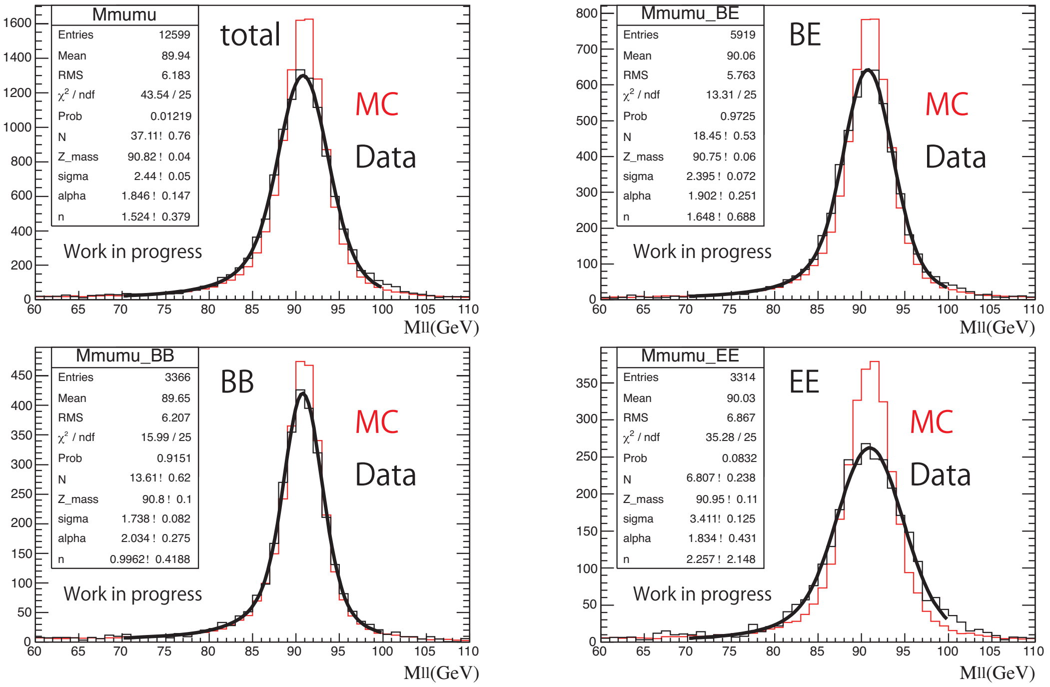

Figure 3.17: Di-muon invariant mass distribution in the later data. Black histogram is data, and red is Monte Carlo simulation scaled with the number of entries of data. (top left) Total, (top right) BE, (bottom left) BB and (bottom right) EE events.

similar to the scale factor *C*, the improved situation in BB and EE events is seen and not clear due to statistics in BE events.

From the study, it is confirmed that the muon detection and its momentum reconstruction are well described in the simulation, and only small scale factor and extra smearing by hand are needed. For the simulation used in the physics analysis in 2011, further improved alignment parameters are applied and updated scale factors and extra smearing derived in the similar way are applied.

σ(GeV)	the early data (3.1 pb) (3.4 pb)	the latter data (41 pb)
BB	2.13 ± 0.25	1.74 ± 0.08
BE	2.21 ± 0.46	2.40 ± 0.07
EE	3.83 ± 0.40	0.34 ± 0.13
Total	2.82 ± 0.24	2.44 ± 0.05

Table 3.2: Obtained muon momentum resolution in the early and latter data in 2010, in each type of events categorized based on the muon direction.

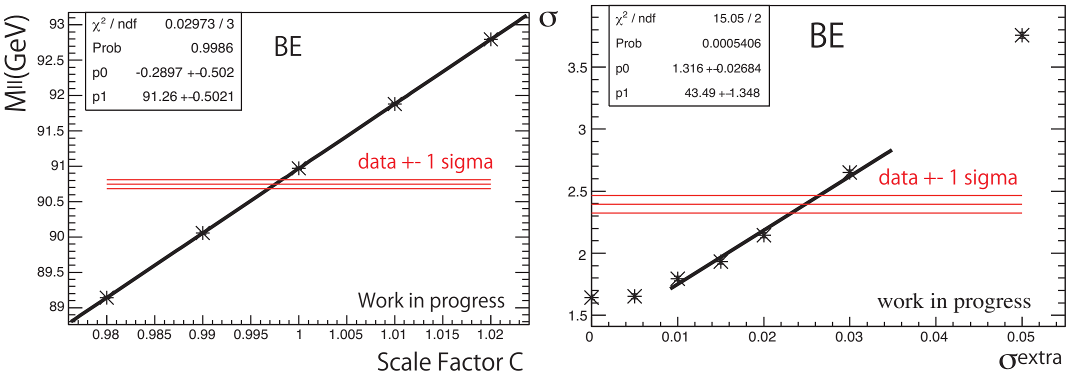

Figure 3.18: The scan of scale factor C(left) and extra smearing(σ_{extra}) in the BE region. The horizontal liens corresponds to the M_{ll} and σ in the later period data and its standard deviation(±1σ).

Scale factor C	Total	BB	EE	EB
The early period	0.997 ± 0.002	1.003 ± 0.003	0.990 ± 0.004	0.999 ± 0.004
The later period	0.9985 ±0.0005	0.9997 ± 0.0007	0.9997 ± 0.0012	0.9976 ± 0.0006

Table 3.3: Derived scale factors to be applied on the muon momentum in the Monte Carlo simulation in 2010, in each type of events categorized based on the muon direction. The scale factor for “Total” is the one derived without the region distinction.

σ_{extra}	Total	BB	EE	EB
The early period	0.034 ± 0.005	0.023 ± 0.005	0.047 ± 0.005	0.020 ± 0.011
The later period	0.025 ± 0.001	0.015 ± 0.002	0.040 ± 0.002	0.025 ± 0.002

Table 3.4: Derived extra searing to be applied on the muon momentum in the Monte Carlo simulation in 2010, in each type of events categorized based on the muon direction. The numbers for “Total” is the one derived without the region distinction.

3.2.2 Muon trigger efficiency

The data for the $\mu\mu$ and $e\mu$ channels is taken with the muon trigger system and it is unavoidable to understand its efficiency and to tune the Monte Carlo simulation if needed.

The muon trigger efficiency is evaluated with tag-and-probe method, which is described in section 2.4.2, in the Z boson resonance($Z \to \mu\mu$). The condition on tag- and prob-muon and their relation are summarized in Table 3.5. The background contribution is estimated by Monte Carlo simulation and it is found to contribute less than 1 %. It is subtracted from the efficiency calculation.

tag muon	isolated reconstructed muon with $P_T > 20$ GeV trigger matching : ΔR between muon and trigger < 0.2.
probe muon	isolated reconstructed muon with $P_T > 20$ GeV
invariant mass	$\lvert m_{ll} - m_Z \rvert < 10$ GeV
charge	opposite charge
opening angle	$\Delta\phi > 1.5$

Table 3.5: The requirements of the tag and probe muons for muon trigger efficiency estimation.

The trigger efficiency in data of 1.04 fb^{-1} is evaluated by dividing the data taking period into four as Table 3.6 shows. Between the periods, the LHC accelerator condition is improved in order to deliver higher luminosity, and also the ATLAS detector maintenance is performed. Therefore it is important to verify the stability of the trigger efficiency, and if some problems are seen, investigate them so that they are under control.

period B,D,E	208 pb
period F	121 pb
period G	464 pb
period H	237 pb

Table 3.6: The definition of data period which is used in the muon trigger efficiency evaluation.

The muon trigger efficiency is found to be stable throughout the periods excepts two problems. The Figure 3.19(left) shows the trigger efficiency map in η-ϕ space during the period F. Some holes in $\phi = [-2 : -1]$ are regions where trigger chambers are not implemented due to the feet of the ATLAS detector, and another hole in $\eta = 0, \phi = 2.5$ is due to missing chambers due to the inner detector cabling. Low trigger efficiency beyond $|\eta| = 2.4$ is due to coverage of the muon trigger system.

The one problem is found in period G. Figure 3.19(right) is the efficiency map in the period. Compared to that in period F as shown in Figure 3.19(bottom), clear drop in $\eta = [0.8 - 1.05]$ is seen. The cause is found to be an ad-hoc trigger rate limiter implemented during the commissioning period. As the instantaneous luminosity delivered from the LHC is increased, the trigger rate reaches at the limit(1 kHz) in the region, and trigger signals are suppressed. The limit is immediately removed.

The other problem is found in the period H. Figure 3.20 shows the trigger efficiency comparison between period B-G and H. An efficiency drop is seen in the region $(\eta, \phi) = ([-0.2 : 1], [-2 : -3])$. The cause is found to be a frequent drop-out of the RPC readout system from the ATLAS data

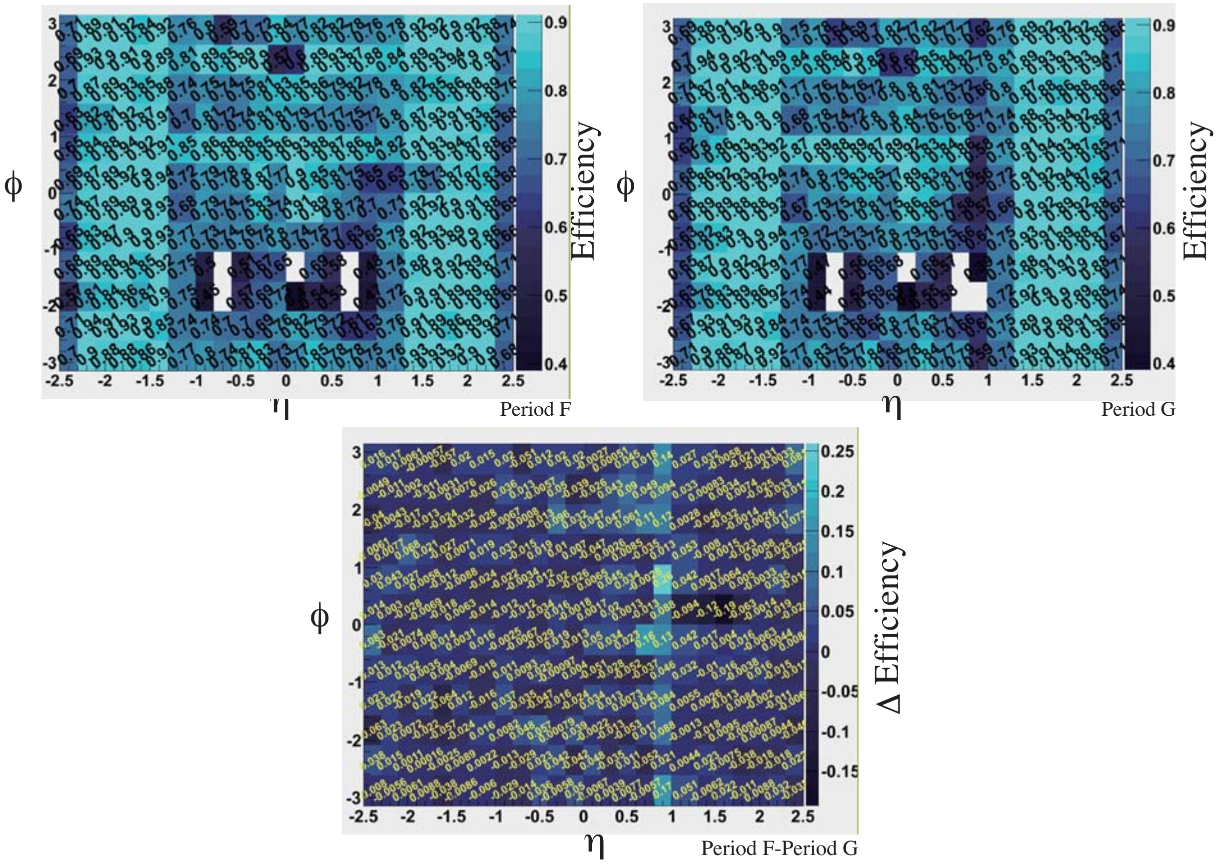

Figure 3.19: (Top left) Muon trigger efficiency map in the $\eta-\phi$ space during the period F. (Top Right) The trigger efficiency during the period G. (Bottom) The figure shows the difference between the two period and the clear drop is seen around $\eta \sim 0.8 - 1.05$.

acquisition system, which caused inefficiency of the level 2 trigger due to lack of information from level 1.

Since these efficiency drops are understood, all the data are used for the physics analysis and the efficiency throughout the periods are evaluated as Figure 3.21(left). The systematic uncertainty is evaluated by varying the condition in the tag-and-probe method as Table 3.7 and the total with the statistical uncertainty is shown in Figure 3.21(right). These values are used in section 2.5.1.

3.2.3 Muon isolation efficiency

The efficiency of muon identification is also estimated with tag-and-probe method, which is also used for the estimation for electron in section 2.4.2. The probe muon is also the combined muon as defined in this section but without the isolation requirements. Figure 3.22 shows the result as a function of η and P_T of muons, minimum opening angle ΔR between the muon and jets, and the number of vertices. No clear dependence is seen, and the scale factor is prepared as a constant and it is 1.0008 ± 0.0003(stat.) ± 0.0003(syst). For the systematic uncertainties, the same contributions as

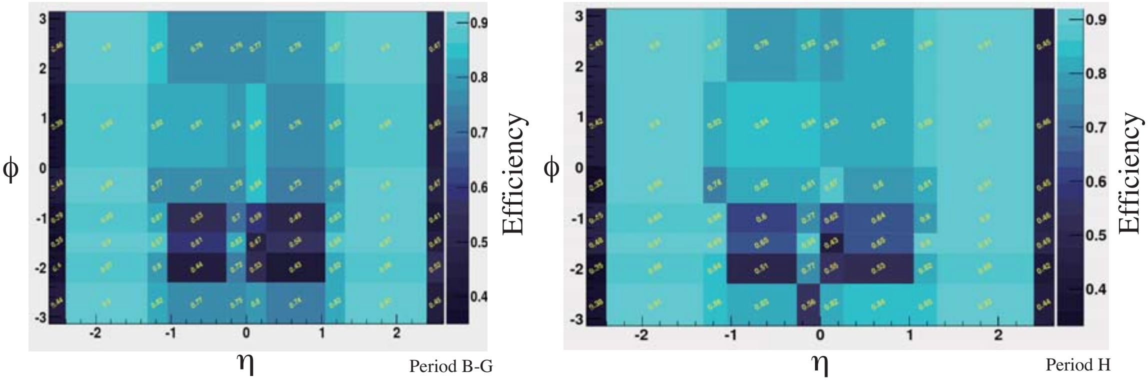

Period B-G

Period H

Figure 3.20: Trigger efficiency map for period B-G(left) and period H(right). Efficiency drop at the bin of $\{\eta, \phi\} \sim \{[-0.2 : 1], [-2 : -3]\}$ is seen in the later period.

Z boson mass window	use 8 or 12 GeV instead of 10 GeV.
tag muon isolation	remove isolation requirement
background estimation	increased and decreased by 100%
trigger matching radius ΔR	use 0.1 and 0.5 instead of 0.2

Table 3.7: The systematic uncertainties that are taken into account in the muon trigger efficiency evaluation.

the muon trigger efficiency estimation are taken into account.

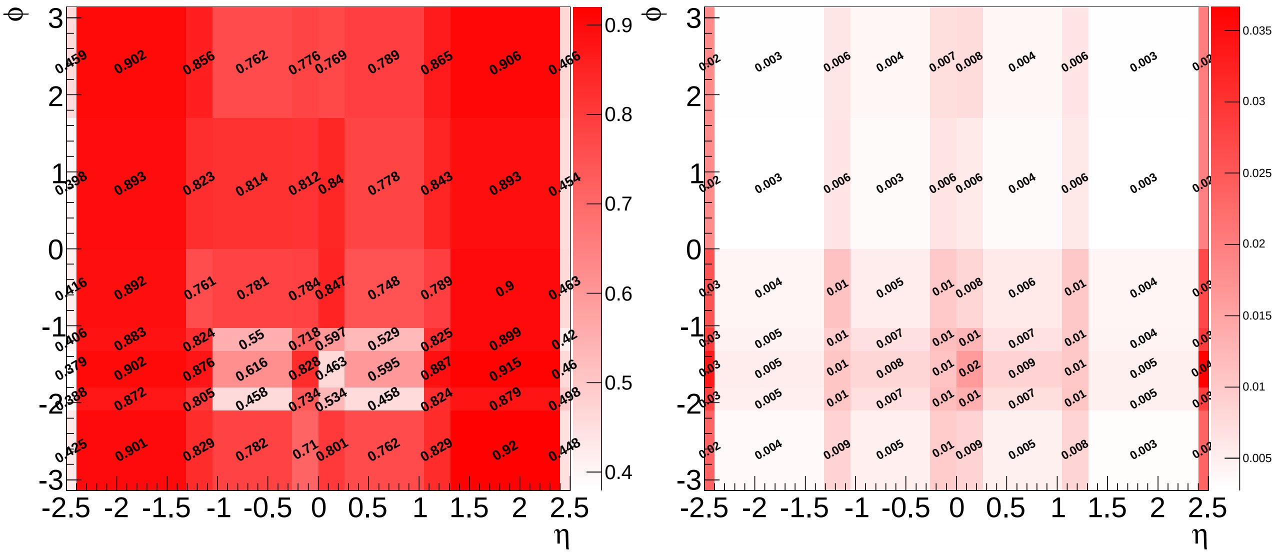

Figure 3.21: The muon trigger efficiency (left) and its uncertainty(right) throughout the data taking period.

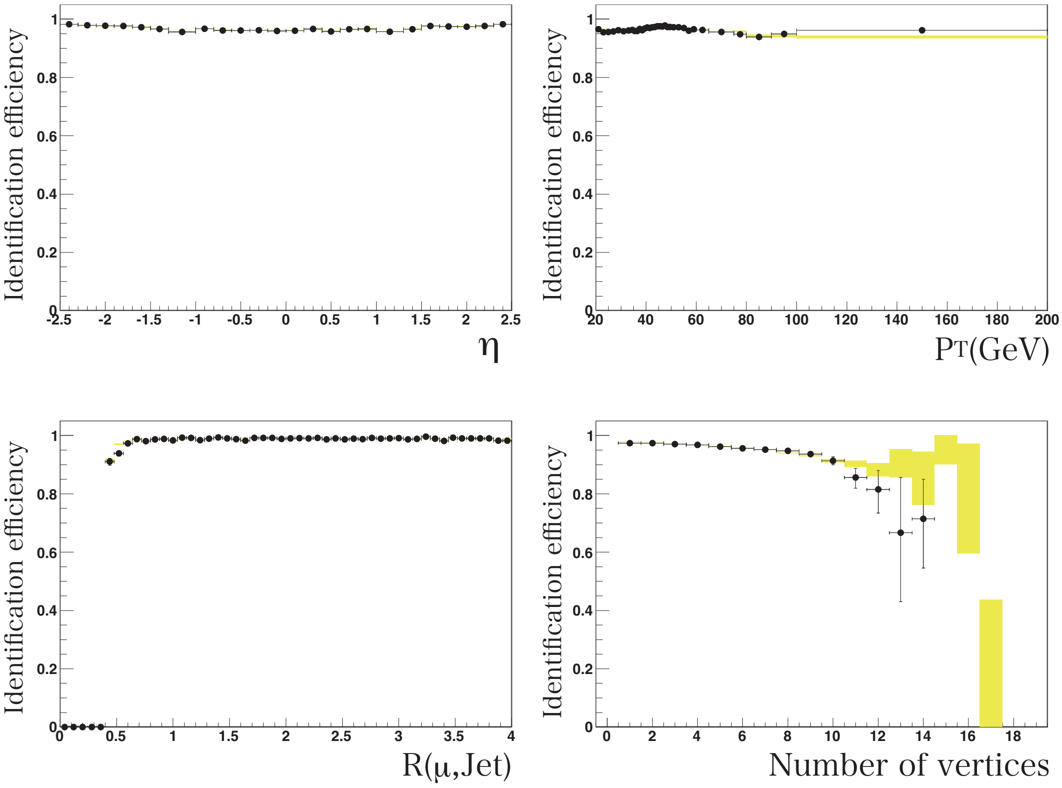

Figure 3.22: Muon identification efficiency as functions of (top left) η, (top right) P_T, (bottom left) minimum opening angle ΔR between the muon and jets, and (bottom right) the number of vertices. Dots stands for data and colored(yellow) histogram is the MC simulation.

Chapter 4

Measurement of *W* Boson Polarization in Top Quark Decay with $t\bar{t}$ Di-lepton Mode

The analysis measures the *W* boson polarization in the top quark decay via the distribution of charged lepton emission angle θ^* on the *W* boson rest frame. The measurement is done with the top quark pair production event decaying into di-lepton final state.

The analysis has mainly two difficulties. The one is signal-to-noise ratio (S/N). The cross section of the top quark pair is 10^{-9} times smaller than that of the total inelastic scattering. The other is the neutrinos momenta. In the di-lepton channel, at which the analysis targetes, there are two neutrinos and six parameters are unknown, while only the observable are missing energy in x and y directions of the system of the two neutrinos.

Concerning the S/N, selecting the di-lepton channel for the analysis improves the situation which is discussed in section 4.1. Furthermore, it reaches at reasonable level by applying event selection based on the characteristics of the signal and background, which is discussed in section 4.2. Concerning the neutrinos momenta, events are reconstructed by assuming some kinematical condition. The reconstruction procedure is discussed in section 4.3. The *W* boson polarization is extracted from the reconstructed $\cos\theta^*$ distribution. Including the translation of the relation into the parameter of the effective Lagrangian, is discussed in the section 4.4.

4.1 Data and basic event selection

The analysis used data of 1.04 fb^{-1} of proton-proton collisions with 7 TeV center of mass energy accumulated with the single electron and muon triggers as described in section 2.5. Every event is required to pass following basic data-quality criteria in order to reject events not coming from collisions.

- the primary vertex consists of more than four tracks so that the vertex is well-defined.
- no badly-reconstructed jet.
- events which have two muons with opening angle grater than 3.1 radian is rejected.

Every event is also required to have two tight leptons with the opposite charge. The kinematical requirements on the leptons are $E_T > 25$ GeV for electrons and $p_T > 20$ GeV for muons as described in the section 2.4.2 and 2.4.3. The threshold of the energies are defined so that the efficiency of the lepton triggers are stable for such charged leptons. After the quality requirements and di-lepton requirement, the number of events were

- ee channel : 1.9×10^5 events , S/N $\sim 2 \times 10^{-3}$
- $\mu\mu$ channel : 4.0×10^5 events , S/N $\sim 2 \times 10^{-3}$
- $e\mu$ channel : 3.1×10^3 events , S/N ~ 1

Compared to the S/N = 10^{-9} as of the cross section, the situation is drastically improved : 10^6 times larger in the di-electron and di-muon channels and 10^9 in the $e\mu$ channel. This is because the event which created two high energy charged leptons are limited. Especially the background level in $e\mu$ is quite small since the SM process that produces the two leptons with different flavor is limited.

4.2 Event Selection and Background Estimation

4.2.1 Event Selection

The target channel is di-lepton channel of the top quark pair : $t\bar{t} \rightarrow W^+bW^-\bar{b} \rightarrow l^+\bar{\nu}bl^-\nu\bar{b}$. The event leaves following signatures on the ATLAS detector;

- Two charged leptons (e, μ) isolated from other particles.
- At least two jets from b-quarks.
- Large missing E_T due to two neutrinos that escape the detector.

As to the lepton isolation, isolated lepton is called *tight* lepton and non-isolated *loose* as defined in the section 2.4.2(electron) and 2.4.3 (muon) quantitatively. Charged leptons from real weak bosons are called *true* leptonm and others *fake*, which may be charged leptons in semi-leptonic decays of hadrons or mis-identified hadrons. The channel is furthermore categorized into ee, $\mu\mu$ and $e\mu$ channels from the point of view of the analysis.

Focusing on the two tight leptons source, the background in this analysis is the following.

- *Drell-Yan* process (in general it contains virtual photon γ^* but label as “Z+jets” in what follows) decaying into ee and $\mu\mu$
- Drell-Yan decaying into $e\mu$ via tau leptons : $Z/\gamma^* \rightarrow \tau\tau \rightarrow l\nu_l\nu_\tau l\nu_l\nu_\tau (l = e, \mu)$
- Single top quark associated with one W boson : $tW \rightarrow bWW \rightarrow bl\nu l\nu$
- Di-boson WW, WZ and ZZ decaying into final states with two charged leptons.
- *Fake* in which one or both leptons are fake.

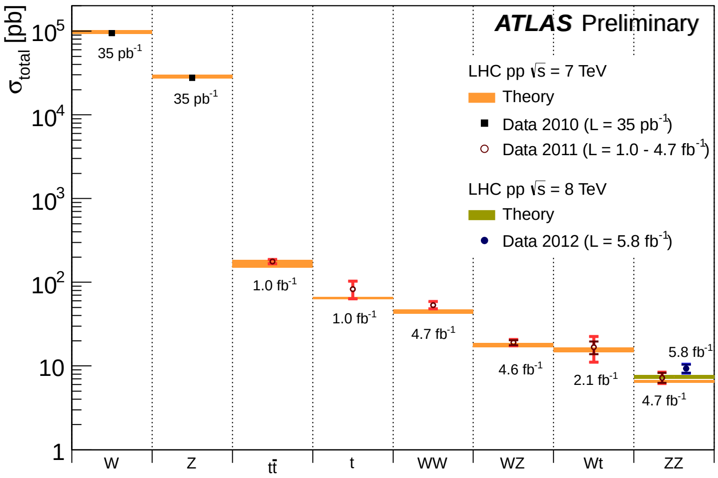

Figure 4.1: The theoretical and measured cross section.

Figure 4.1 shows the cross section of these background. In this analysis, contribution from Drell-Yan in $e\mu$ channel, tW and di-boson is estimated with the Monte Carlo simulation. Meanwhile, Drell-Yan in ee and $\mu\mu$ channel, and fake are estimated based on data, which is discussed in the following section 4.2.2 and 4.2.3 respectively.

4.2.2 Drell-Yan background estimation

In the event selection which is discussed in the section 4.2.4, missing E_T is used which is quite effective to reduce the Drell-Yan background in ee and $\mu\mu$ that has no source of missing E_T intrinsically. However, the amount of the Drell-Yan background is enormous and its “apparent” missing E_T must be evaluated precisely. The missing E_T distribution is smeared due to the resolution of the detector, especially energy resolution of the calorimeters, which may depends on the actual detector condition and is difficult to describe in simulation precisely. Therefore the contribution from the Drell-Yan background is estimated by data-driven way.

The method defines the region where $|m_{ll} - m_Z| < 10$ GeV, $E_{\mathrm{T}}^{\mathrm{miss}} > 40$ GeV and the number of jets > 2 as a control region(CR) as Figure 4.2 shows. The regions is not used in the physics analysis, as discussed in section 4.2.4. It extracts a scale factor(SF) that makes the number of entries in data and Monte-Carlo simulation to be equal in the CR, and applies the SF to the Drell-Yan Monte-Carlo simulation in the signal region(SR) :

$$\mathrm{DY(SR)} = \mathrm{SF} \times \mathrm{DY_{MC}(SR)} \tag{4.1}$$

$$= \frac{\mathrm{DATA(CR)} - \mathrm{NonDY_{MC}(CR)}}{\mathrm{DY_{MC}(CR)}} \times \mathrm{DY_{MC}(SR)} \tag{4.2}$$

where

- DATA(CR) : the number of data in the control region.

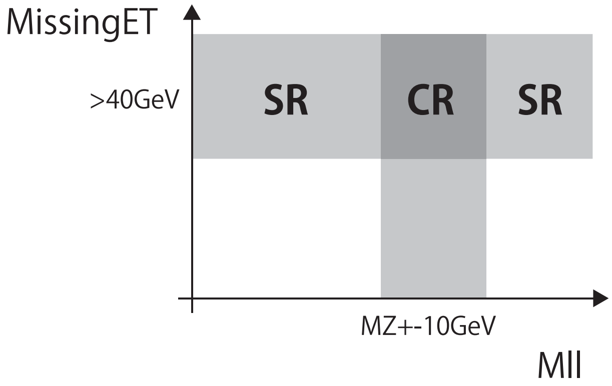

Figure 4.2: The definition of the Drell-Yan control region(CR) with respect to the signal region(SR).

- $\mathrm{NonDY_{MC}}$(CR) : estimated number of non Drell-Yan events in the control region.
- $\mathrm{DY_{MC}}$(CR) : estimated number of the Drell-Yan events in the control region.
- $\mathrm{DY_{MC}}$(SR) : estimated number of the Drell-Yan events in the signal region.

and the values and calculated scale factors are summarized in the Table 4.1. The uncertainties of the scale factors were estimated from the statistical fluctuation of data, which was dominant, and variation of it when the definition of control region changed from $E_{\mathrm{T}}^{\mathrm{miss}} > 40$ GeV to $E_{\mathrm{T}}^{\mathrm{miss}} > 30$ GeV, which is found to be negligible. Figure 4.3 shows the M_{ll} distribution in the signal region with the scale factor applied.

		DY	Physics Background Sources (NonDY)					
Channel	Data(CR)	MC(CR)	$t\bar{t}$	$Z \to \tau\tau$	Single Top + W	Di-boson	Fake	SF
ee	164	62	46	0.0	2.4	4.4	0	1.8 ± 0.2
$\mu\mu$	296	180	86	0.0	5.0	6.8	0	1.1 ± 0.1

Table 4.1: The number of data and estimation in the Drell-Yan background control region. From the numbers the scale factors (SF) for the Drell-Yan background in the signal region are derived.

4.2.3 Fake background estimation

In order to estimate the contribution from the fake leptons, the probability that fake leptons pass the isolation criteria, so-called fake rate, in needed. In general, the possibility depends on the detector condition and pile-up, and it is not difficult to simulate. Therefore, the fake background has to be estimated by a data-driven way.

The number of events which pass the event selection of “two tight leptons” N_{TT} consists of the followings :

- N_{rr} : Both leptons are real leptons.

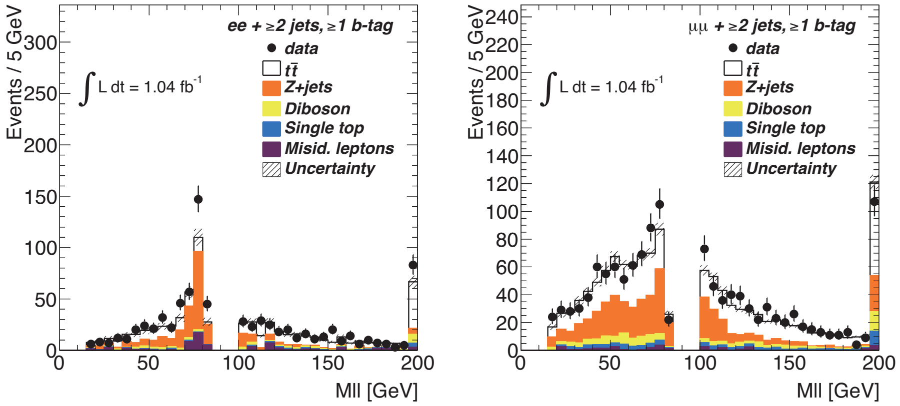

Figure 4.3: M_{ll} distribution in the signal region with derived scale factor applied, in di-electron and di-muon channels.

- N_{rf}, N_{fr} : One of the lepton is real and the other is fake.
- N_{ff} : Both leptons are fake.

In the second category, the distinction of N_{rf} and N_{fr} are important for $e\mu$ channel ; for example, the first index is for electron and the other for muon. Their contribution to N_{TT} depends on the efficiency of isolation r , that is the possibility of true leptons passing the isolation criterion, and the fake rate f ;

$$N_{TT} = r_1 r_2 N_{rr} + f_1 r_2 N_{fr} + r_1 f_2 N_{rf} + f_1 f_2 N_{ff} \tag{4.3}$$

where the suffix 1 and 2 mean that the efficiency r and fake rate f is for the first and second lepton respectively.

Similarly the number of events in which one of the lepton is loose (N_{LT}, N_{TL}) and both (N_{LL}) are also written by N_{rr}, N_{rf}, N_{fr} and N_{ff}. The relation can be summarized in the matrix equation;

$$\begin{pmatrix} N_{TT} \\ N_{TL} \\ N_{LT} \\ N_{LL} \end{pmatrix} = \begin{pmatrix} r_1 r_2 & r_1 f_2 & f_1 r_2 & f_1 f_2 \\ r_1(1-r_2) & r_1(1-f_2) & f_1(1-r_2) & f_1(1-f_2) \\ (1-r_1)r_2 & (1-r_1)f_2 & (1-f_1)r_2 & (1-f_1)f_2 \\ (1-r_1)(1-r_2) & (1-r_1)(1-f_2) & (1-f_1)(1-r_2) & (1-f_1)(1-f_2) \end{pmatrix} \begin{pmatrix} N_{rr} \\ N_{rf} \\ N_{fr} \\ N_{ff} \end{pmatrix} \tag{4.4}$$

The amount of the fake contribution to N_{TT} are the last three terms in equation (4.3), and each component can be expressed by N_{TT}, N_{TL}, N_{LT} and N_{LL} that are all observable :

$$\begin{aligned} N^{tt}_{\text{fake}} =& r_1 f_2 N_{rf} + f_1 r_2 N_{fr} + f_1 f_2 N_{ff} \\ =& \ \alpha r_1 f_2 [(f_1 - 1)(1 - r_2) N^{TT} + (1 - f_1) r_2 N^{TL} + f_1 (1 - r_2) N^{LT} - f_1 r_2 N^{LL}] \\ +& \ \alpha f_1 r_2 [(r_1 - 1)(1 - f_2) N^{TT} + (1 - r_1) f_2 N^{TL} + r_1 (1 - f_2) N^{LT} - r_1 f_2 N^{LL}] \\ +& \ \alpha f_1 f_2 [(1 - r_1)(1 - r_2) N^{TT} + (r_1 - 1) r_2 N^{TL} + r_1 (r_2 - 1) N^{LT} - r_1 r_2 N^{LL}] \end{aligned} \tag{4.5}$$

where $\alpha = 1/(r_1 - f_1)(r_2 - f_2)$. Figures 4.4 and 4.5 show the fake rate f estimated from di-jet events, and isolation efficiency r from Drell-Yan events, as functions of η and p_T. Finally, every event

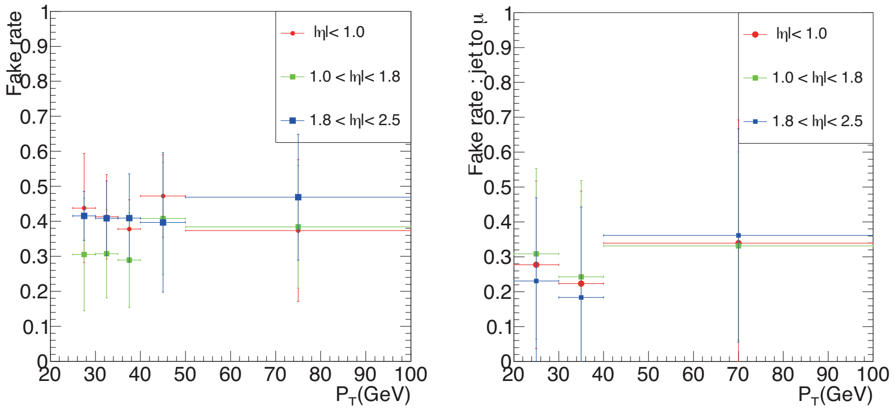

Figure 4.4: Fake rate of jets(loose lepton from jet) as isolated electrons(left) and muons(right) .

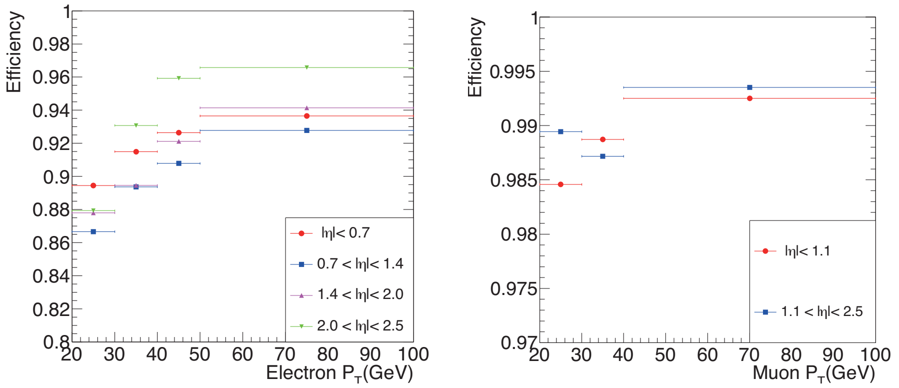

Figure 4.5: Lepton efficiency to pass isolation criteria for electrons(left) and muons(right).

with two leptons, regardless of their isolation, has a weight as equation (4.5) gives to express fake contribution.

4.2.4 Event selection criteria

The background contribution is quite similar in ee and $\mu\mu$ channels which have the same flavor lepton. While, they are different to the $e\mu$ channel, in which the flavor of the charge lepton is different.

The ee and $\mu\mu$ channel have large background of Drell-Yan as Figure 4.6 shows. This background is relatively easy to deal with since the invariant mass of the di-lepton is to be around the Z boson mass. From the reason, $|m_{ll} - m_Z| > 10$ GeV is required. Furthermore, the Drell-Yan events do not have sources of missing E_T intrinsically, as Figure 4.7 shows, and $E_{\mathrm{T}}^{\mathrm{miss}} > 40$ GeV is required.

The $e\mu$ channel has also Drell-Yan background : ones decaying into the $e\mu$ final state via τ pairs ($Z/\gamma^* \to \tau\tau \to e\nu\nu\mu\nu\nu$). The background is less energetic compared to the signal, and significant fraction of the energy is given to neutrinos, which escape the detector. Here, the scalar sum of the

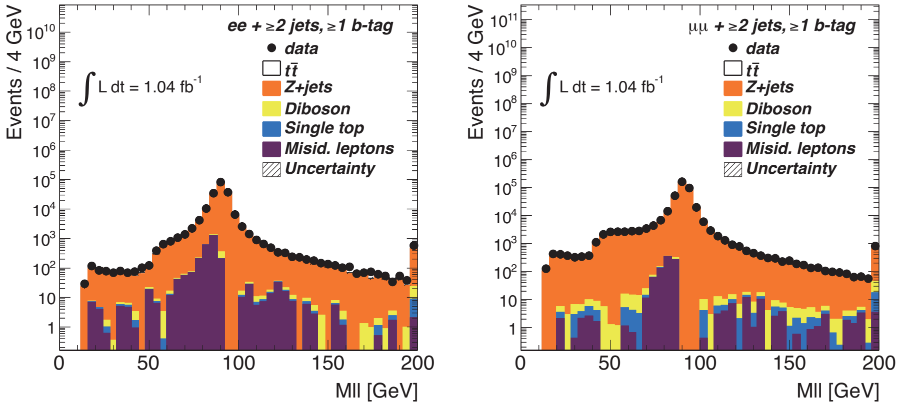

Figure 4.6: Di-lepton invariant mass M_{ll} distributions in each channel after basic selection and di-lepton requirements. In order to remove background from Drell-Yan(Z+jets), selection criteria of $|M_{ll} - m_z| > 10$ GeV is required in the *ee* and $\mu\mu$ channels.

	ee	$\mu\mu$	$e\mu$
di-lepton invariant mass m_{ll}	$\lvert m_{ll} - m_Z \rvert > 10$ GeV		-
	$m_{ll} > 15$ GeV		
E_T^{miss}	> 40 GeV		-
H_T	-	-	> 130 GeV
The number of jets	≥ 2		
The number of *b*-tagged jets	≥ 1		

Table 4.2: The event selection in this analysis.

charged lepton and jet P_T is defined as H_T, $H_T = \sum_{\text{charged leptons}} |P_T| + \sum_{jets} |P_T|$, and $H_T > 130$ GeV is required. Figure 4.8 shows the H_T distribution.

As to the low-mass region of m_{ll}, is expected to have large contribution from Drell-Yan such as J/Ψ and Υ, while small entries of the signal. Therefore, $m_{ll} > 15$ GeV is required.

The characteristics of jets can be used for further selections. The signal has two *b*-quarks from the top quark decays. Events are required to have at least two jets and at least one of them must be *b*-tagged.

Table 4.2 summarize the event selection and Table 4.3 summarizes the number of events passing the selection criteria, and expectation for each process including systematic uncertainties which is listed in section 4.4.1. Figures 4.9 and 4.10-4.19 show the number of b-tagged jets after all the selection but the one "at least one *b*-tagged jet", and the kinematical distributions of leptons and jets after all the event selection.

The cross section of $t\bar{t}$ event, $\sigma_{t\bar{t}}$, can be calculated from the relation

$$N_{\text{data}} - N_{\text{BG}} = \mathcal{A}\sigma_{t\bar{t}} \int \mathrm{d}t\mathcal{L} \tag{4.6}$$

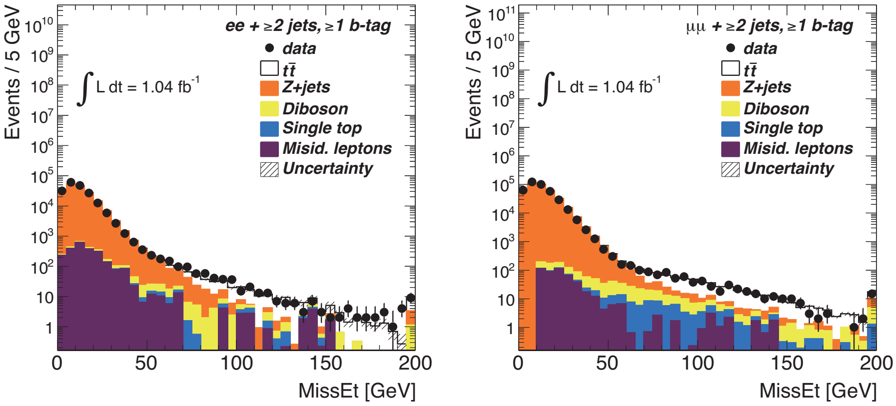

Figure 4.7: Missing E_T distributions in ee and $\mu\mu$ channels after basic selection and di-lepton requirements. In addition to the Z mass cut in Figure 4.6, $E_{\mathrm{T}}^{\mathrm{miss}} > 40$ GeV is required to reduced the Drell-Yan background.

where N_{data} is the number of data passing the event selection, N_{BG} is the estimated background events passing the selection, $\mathcal{A}$ is acceptance of the selection with respect to $t\bar{t}$ signal and $\int \mathrm{d}t\mathcal{L} = 1.04\ \mathrm{fb}^{-1}$ is the integrated luminosity. The acceptances in each channel can be calculated from the Table 4.3 as

$$\mathcal{A} = \frac{N_{t\bar{t}}^{MC}}{\sigma_{t\bar{t},\mathrm{SM}} \times 1.04\mathrm{fb}^{-1}} \tag{4.7}$$

where $N_{t\bar{t}}$ is the number of Monte Carlo $t\bar{t}$ events passing the selection and $\sigma_{t\bar{t},\mathrm{SM}}$ is the theoretical cross section of the $t\bar{t}$ event in the Standard Model, 164.6 pb. The results are also summarized in the Table 4.3. These numbers agree with the Standard Model expectation.

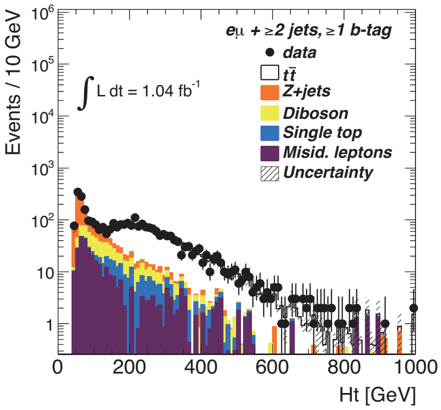

Figure 4.8: H_T distribution in $e\mu$ channel after basic selection and di-lepton requirements. In order to reduce $Z \rightarrow \tau\tau \rightarrow e\mu\nu_e\nu_\mu\nu_\tau\nu_\tau$ background, $H_T > 130$ GeV is required.

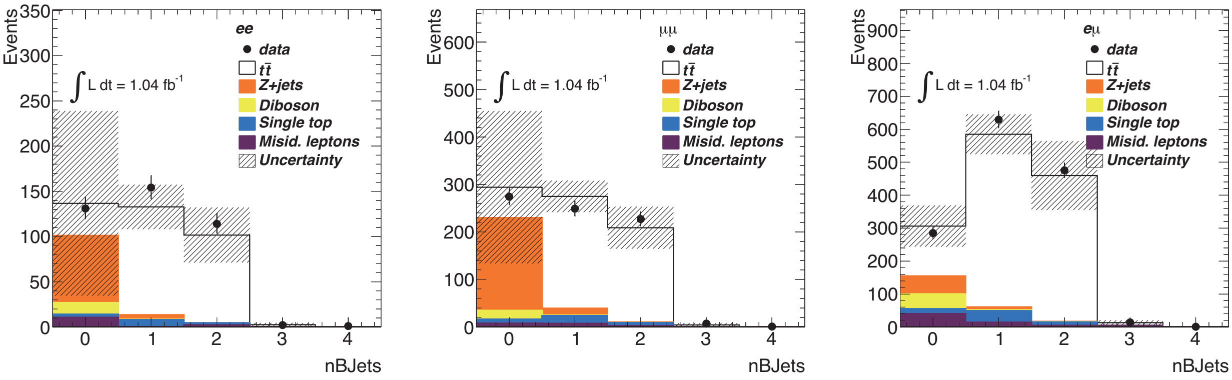

Figure 4.9: The number of b-tagged jets after all the event selections but the requirement “at least one b-tagged jet” .

	ee	$\mu\mu$	$e\mu$
$t\bar{t}$ signal	218.6 ± 37.4	437.7 ± 54.4	975.1 ± 120.3
Z(ee,$\mu\mu$)	4.9 ± 9.5	13.7 ± 10.0	-
Z($\tau\tau$)	0 ± 0	2.3 ± 1.3	10.0 ± 4.9
single top	9.8 ± 2.1	23.0 ± 3.7	45.3 ± 7.1
di-boson	0.5 ± 0.3	1.1 ± 0.4	3.1 ± 0.9
fake	3.2 ± 1.6	10.3 ± 5.2	23.3 ± 11.7
prediction	237.0 ± 38.7	488.1 ± 55.7	1056.8 ± 121.2
data	271	484	1119
Acceptance (%)	0.128	0.256	0.570
Measured cross section (pb) (syst.+stat.)	191 ± 42	163 ± 25	175 ± 25

Table 4.3: The numbers of events passing the event selection criteria. The uncertainties are statistical and systematic which is discussed in section 4.4.1. The acceptance is defined with respect to the total top quark pair production and does includes the branching ratio of the top quark pair to each channel. The uncertainty of the cross section includes the systematic uncertainty which is discussed in detail in section 4.4.1.

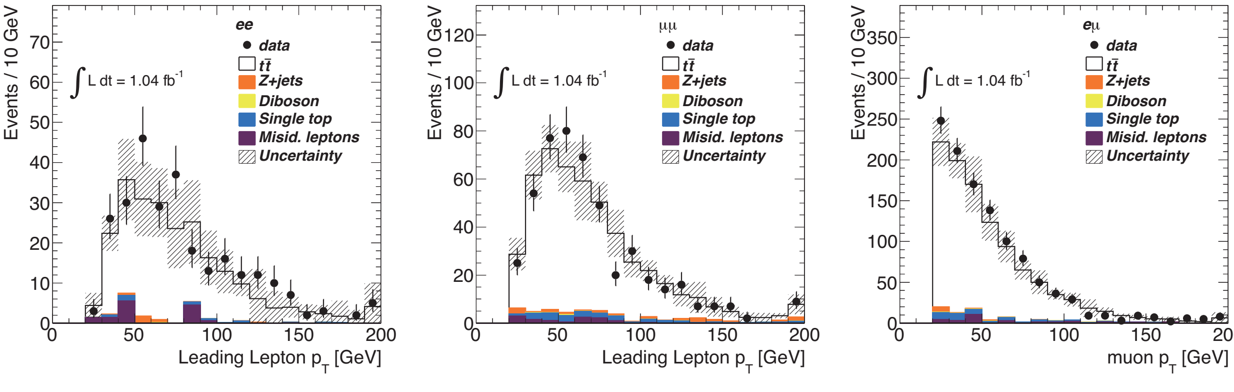

Figure 4.10: p_T distribution of the first leading(*ee*, $\mu\mu$ channels) and muon($e\mu$ channel) after all the event selections.

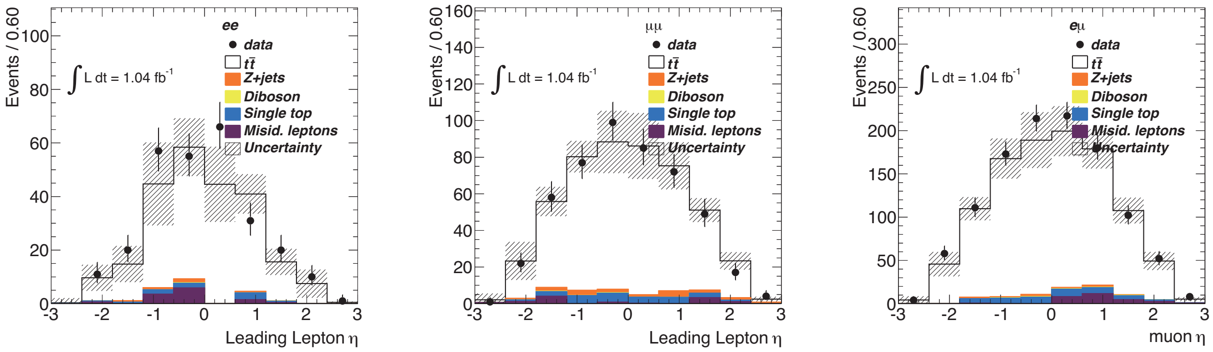

Figure 4.11: η distribution of the first leading(ee, $\mu\mu$ channels) and muon($e\mu$ channel) after all the event selections.

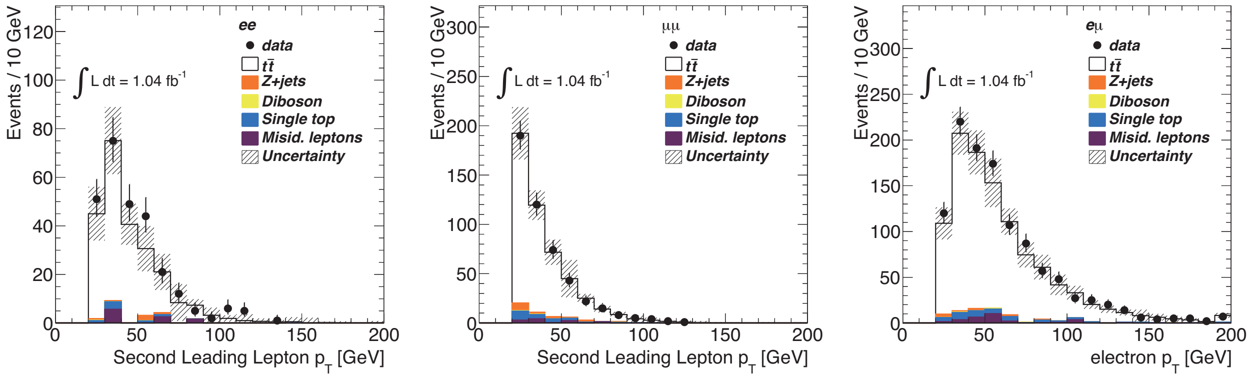

Figure 4.12: p_T distribution of the second leading(ee, $\mu\mu$ channels) and electron($e\mu$ channel) after all the event selections.

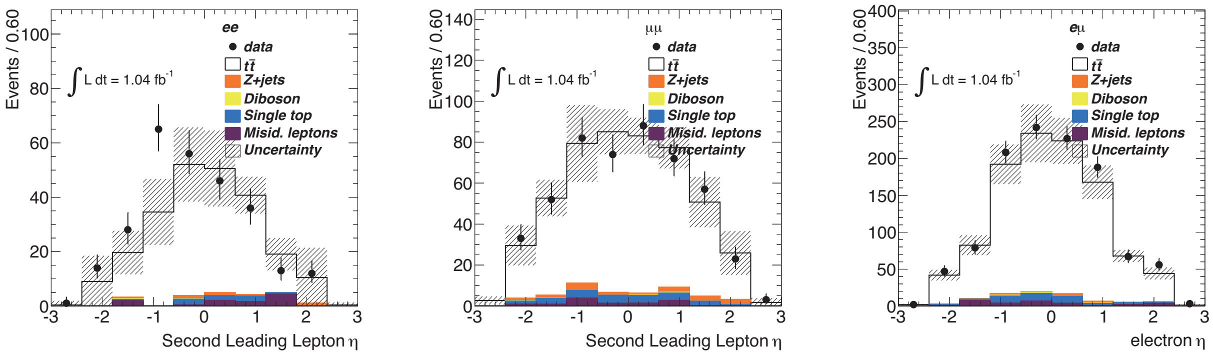

Figure 4.13: η distribution of the second leading(ee, $\mu\mu$ channels) and electron($e\mu$ channel) after all the event selections.

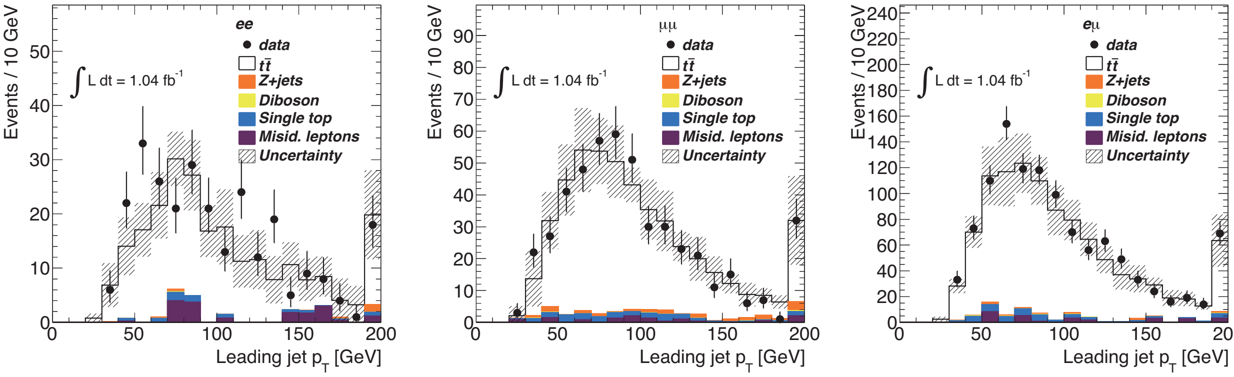

Figure 4.14: p_T distribution of the first leading jet after all the event selections.

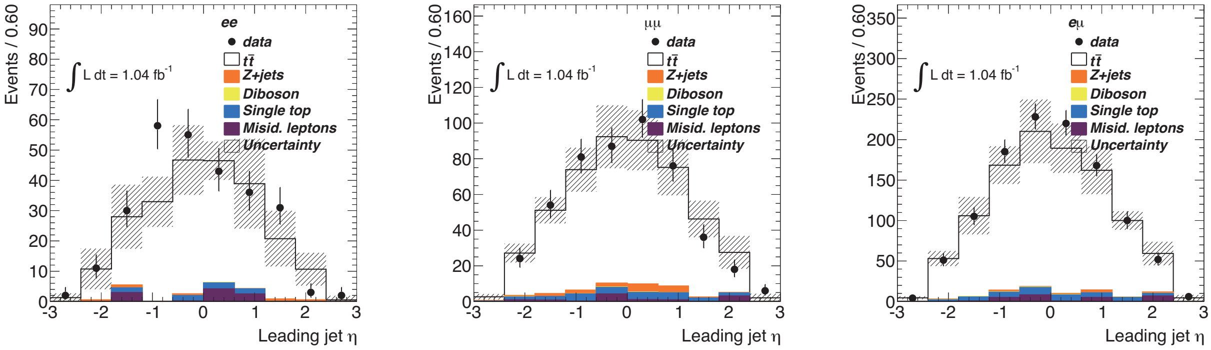

Figure 4.15: η distribution of the first leading jet after all the event selections.

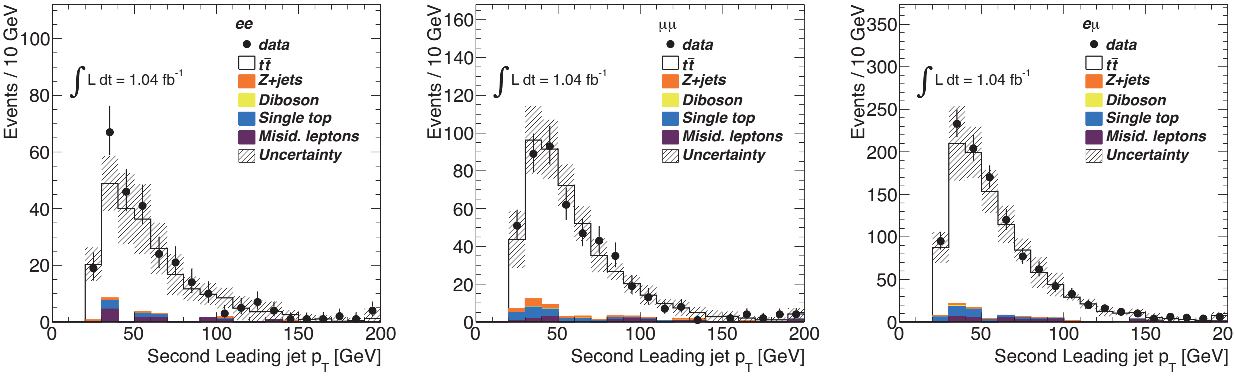

Figure 4.16: p_T distribution of the second leading jet after all the event selections.

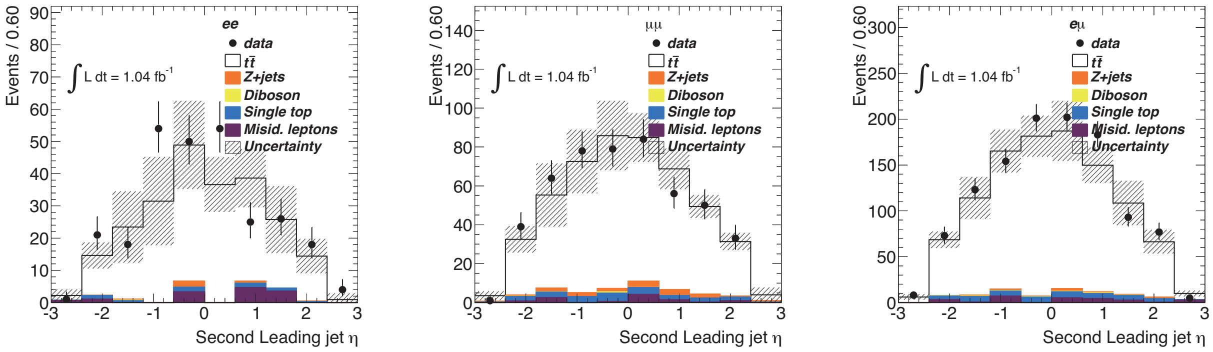

Figure 4.17: η distribution of the second leading jet after all the event selections.

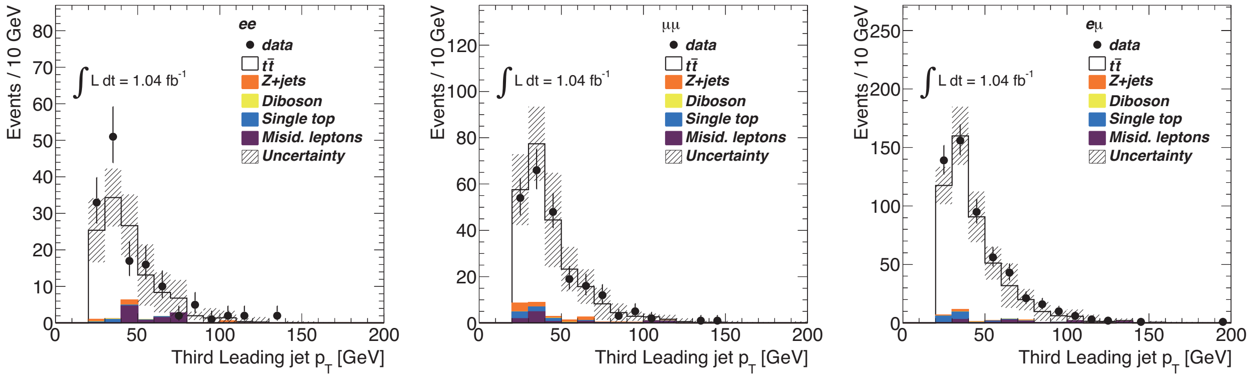

Figure 4.18: p_T distribution of the third leading jet after all the event selections.

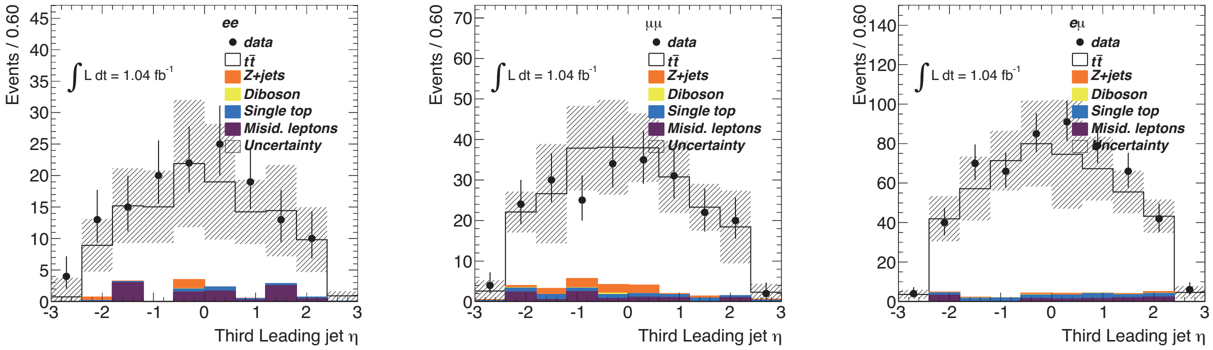

Figure 4.19: η distribution of the third leading jet after all the event selections.

4.3 Event Reconstruction

In the next step, two top quarks in the selected events are fully reconstructed. Here, two jets must be assigned to b- and $\bar{b}$-quark jets, momenta of the two neutrinos in the decay must be reconstructed. In this analysis, one procedure is proposed and it is investigated how it works. Once the two top quark decay chains are reconstructed, charged lepton emission angle θ^* in each decay is calculated by boosting back the objects momenta to the W boson rest frame.

4.3.1 The top quark pair reconstruction method

All the event passing through the event selection have at least two jets of which at least one is b-tagged, and two charged leptons with opposite charge each other. Expecting that two b-quarks in a top quark pair decay are observed as two jets, two reconstructed jets are chosen from ones in the event. The selection criteria is P_T of the jets, in priority to b-tagged jets. If there are two or more b-tagged jets, the two b-tagged jets with highest P_T are used. If there is only one b-tagged jet, the one and the non-b-tagged jet with highest P_T are used.

The assignment of the two jets to b^+- and b^--quark jets is considered by the invariant mass of the top quark pair. In the proton-proton collision in 7 TeV center of mass energy, the pair of partons in the hard interaction may have more energy than that needed for producing just two top quarks. Figure 4.20 (left) shows the invariant mass of created top quark pair system distribution at the truth level in the Monte Carlo simulation. The distribution has entries from the mass threshold $2m_t \sim 350$ GeV, and its tail reaches ~ 1000 GeV. The produced top quarks are boosted back-to-back using the left energy, and as the result, the emission direction of a b-quark and a charged lepton from the same top quark decay $t \to Wb \to l\nu b$ tend to be close. Therefore, the invariant mass of the charged leptons and jets with correct combination tends to be smaller than that of the wrong combination :

$$m_{\ell,\bar{b}} + m_{\bar{\ell},b} < m_{\ell,b} + m_{\bar{\ell},\bar{b}} \tag{4.8}$$

where $m_{\ell(\bar{\ell}),\bar{b}(b)}$ is the invariant mass of the two objects.

Figure 4.20 (right) shows the $\Delta m \equiv m_{\ell,\bar{b}} + m_{\bar{\ell},b} - (m_{\ell,b} + m_{\bar{\ell},\bar{b}})$ distribution with correct combination in the Monte Carlo simulation. Conversely, the combination is determined so that Δm to be negative.

The momenta of the two neutrinos are reconstructed by the relations based on the energy conservation in the top and W boson decays as equation (4.9) and (4.10) and momentum conservations on the transverse plane as equation (4.11).

$$m_t^2 = (p_t + p_{W^+})^2 \qquad m_W^2 = (p_{l^+} + p_\nu)^2 \tag{4.9}$$

$$m_t^2 = (p_{\bar{t}} + p_{W^-})^2 \qquad m_W^2 = (p_{l^-} + p_{\bar{\nu}})^2 \tag{4.10}$$

$$E_{\mathrm{x}}^{\mathrm{miss}} = p_{\nu,x} + p_{\nu_{\bar{\nu}},x} \qquad E_{\mathrm{y}}^{\mathrm{miss}} = p_{\nu,y} + p_{\bar{\nu},y} \tag{4.11}$$

where p is four momentum of the index particle, and neutrino momenta $p_{\nu,x(y,z)}$, $p_{\bar{\nu},x(y,z)}$ are the unknown variables. In general, these equations have four solutions [1]. If the equations have any solutions

---

[1] This can be understood qualitatively from mathematical point of view. The solution of two equations (4.9) draws an ellipse in the $p_{\nu,x}, p_{\nu,y}, p_{\nu,z}$ space, and ones of equations (4.10) in the $p_{\nu,\bar{x}}, p_{\nu,\bar{y}}, p_{\nu,\bar{z}}$ space. The equations (4.11) unite the two space into four dimensional space, for example $p_{\nu,x}, p_{\nu,y}, p_{\nu,z}, p_{\nu,\bar{x}}$. The solutions are the overlap points of the two ellipse in the space, which are four in general.

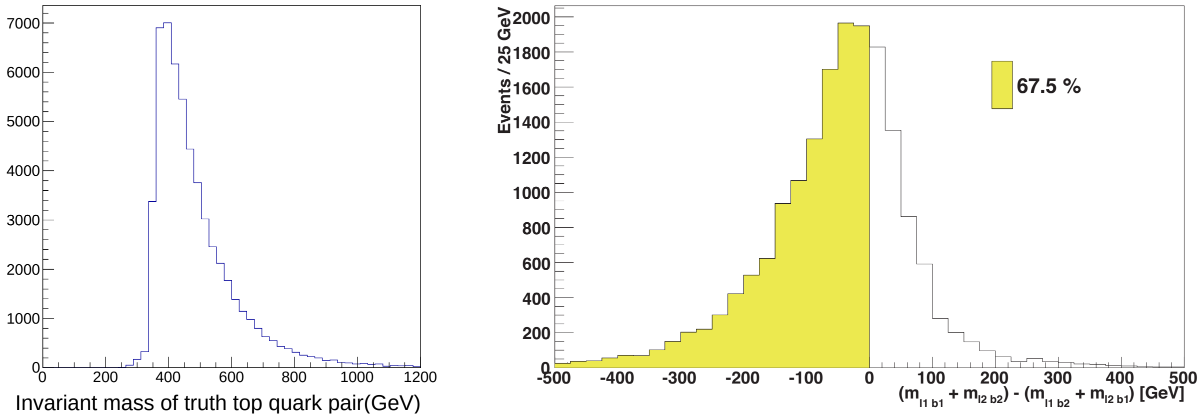

Figure 4.20: (left) The distribution of invariant mass of the truth top quark pair system in the Monte Carlo simulation. (right) M_{lb} distribution. 67.5 % of all events have negative M_{lb} with the correct combination of jets and leptons.

with condition of $m_t = 172.5$ GeV and $m_W = 80.2$ GeV, the one that gave the smallest inner product of neutrinos, $p_{\nu,T} \cdot p_{\bar{\nu},T}$, is chosen. In case of no solution, m_t is reduce to 157.5GeV and then increased to 187.5 GeV by 1.5 GeV steps until any solution is given. If this prescription does not help, the jet-lepton assignment determined based on Δm is swapped with the same trial including mass scan if needed. The events are thrown away if no solution is given, which account for 25% of the selected top quark pair signal.

4.3.2 The behavior of the reconstruction method

The resolution of $\cos\theta^*$ reconstructed with the method described above can be distorted by intrinsic reasons, the detector resolution and preferences of the procedure. An intrinsic reason is the fact that the b-quarks are not observed directly but as jets, and jet energy scale is tuned so that they restore energies of not quarks but truth jets. That is, the input of b-quark kinematics is intrinsically smeared in this analysis. It is natural that the resolution of the reconstructed objects propagated to the reconstructed $\cos\theta^*$. Concerning the effect of the procedure, the rule of the lepton-jet pair determination and relative attempt of the top quark pair reconstruction can affect to the reconstructed $\cos\theta^*$.

These effects are related to each other and difficult to evaluate separately. Instead, in this analysis, they are checked with the Monte Carlo simulation by modifying the reconstruction condition one by one starting from input of fully truth information. Table 4.4 summarizes the prepared sets of conditions and Figure 4.21 shows the $\cos\theta^*_{\text{recon}}$ distribution and $\Delta\cos\theta^* = \cos\theta^*_{\text{truth}} - \cos\theta^*_{\text{recon}}$ distribution in each set.

The ultimate information is the momenta of the particles produced at the interaction point. The information can be accessible in the MC simulation. With this truth information the $\cos\theta^*$ is fully restored. This corresponds to the set A in the table.

The effect of the hadronization

In the set B, the truth quark momenta are replaced by the ones of the truth jets. Their difference is that the truth jets contain the hadronization effect and their momenta are smeared compared to the ones of the truth quark, which results in the smearing of the reconstructed $\cos\theta$ resolution.

The detector resolution effects : jets and charged leptons

The set C uses reconstructed charged lepton momentum instead of the truth momentum. On top of that, the set D uses reconstructed jets which associated with the truth b- and $\bar{b}$-quarks. These replacements reflect the detector resolution, which is found to be small impact on the resolution of the reconstructed $\cos\theta^*$ compared to the hadronization effects above.

The jets assignment to b- and $\bar{b}$-quarks

In the set E , assignment of the jets to the b- and $\bar{b}$-quarks is determined based on the invariant mass with the charged lepton as described in the section 4.3.1.

Selection of the two jets

The set F chooses two reconstructed jets based on the b-tagging and P_T as described in the section 4.3.1.

The reconstruction of the neutrino momentum

All the sets above reconstruct the two top quark decays with truth neutrino momenta. Set G and H reconstruct neutrinos momenta by solving the simultaneous equations (4.9), (4.10) and (4.11) with the input of the truth missing E_T (the vector sum of the transverse momenta of the two truth neutrinos) and reconstructed missing E_T, respectively. The $\Delta\cos\theta^*$ distribution of the set G has worse resolution compared to the set F. This is because the neutrino momentum reconstruction procedure introduces the variety of the reconstructed top quark mass up to ±15 GeV and also allows the pair of the lepton-jet pairs to change. On the other hand, the difference between the results with truth (set G) and reconstructed missing E_T (set H) is almost negligible. This is because the top quark decay chain $t \to Wb \to \ell\nu b$ on the top quark rest frame is fully constrained once the top quark and the W boson masses and the momenta of the bottom quark and the charged lepton are given. The missing E_T is used only for the check if the given two lepton-jet pairs can explain the missing E_T when they are regarded as the two top quark decay products.

	momentum			ℓ-b combination	Missing E_T	resolution	
	b	ℓ	ν			mean	σ
A	truth quark	truth	truth	truth	-	-	
B	truth jet	truth	truth	truth	-	0.00	0.04
C	truth jet	recon	truth	truth	-	0.00	0.05
D	truth-associated reconstructed jet	recon	truth	truth	-	0.00	0.04
E	truth-associated reconstructed jet	recon	truth	invariant mass	-	0.00	0.04
F	reconstructed jet	recon	truth	invariant mass	-	0.03	0.35
G	reconstructed jet	recon	recon	invariant mass	truth E_T	0.11	0.36
H	reconstructed jet	recon	recon	invariant mass	measured E_T	0.11	0.36

Table 4.4: Prepared sets of conditions. For momenta of b-quark, the input can be truth quark, truth jets or reconstructed jets. For the momenta of the charged lepton ℓ, truth or reconstructed momentum can be the input. For the momenta of neutrino, truth or calculated ones in the reconstruction procedure can be used. For the combination of charged leptons and b-quarks, the correct combination can be determined by relaying on the truth information of input if b-quark, which means “truth” in this category. In the reconstruction of neutrino momentum, missing E_T is one of the input. Here, truth missing E_T which is the vector sum of the neutrinos momenta and reconstructed missing E_T are tested. The column “resolution” summarizes the means and standard deviations (σ) of the resolution distribution in Figure 4.21(right).

The breakdown of the reconstructed $\cos\theta^*$ is also checked from the point of view of the jet assignment. The reconstructed events can be categorized based on whether the two jets are selection and whether they are assigned to the correct quarks. Table 4.5 shows the categories. Also their fraction of the total reconstructed events and the resolution are summarized. The desirable situation is type (i) in which the two of the appropriate jets are chosen and assigned to b- and $\bar{b}$-quarks correctly. The type (v) reconstructed $\cos\theta^*$ distribution with the best resolution as Figure 4.22 shows. On the other hand, the type (ii) where two appropriate jets are chosen but they are assigned to wrong b- and $\bar{b}$-quarks, which is found to give the worst resolution. It is worth mentioning that, regardless of whether the appropriate jet is assigned to one top quark side, the other top quark can be reconstructed correctly if the appropriate jet is assigned to the b (or $\bar{b}$) quark. The $\bar{b}$ quark side of the type (iii) and b quark side of the type (iv) in the table corresponds to the case and their mean and standard deviation of the resolution is almost the same as the type(i) as Figure 4.22 shows. One the other hand, the resolution

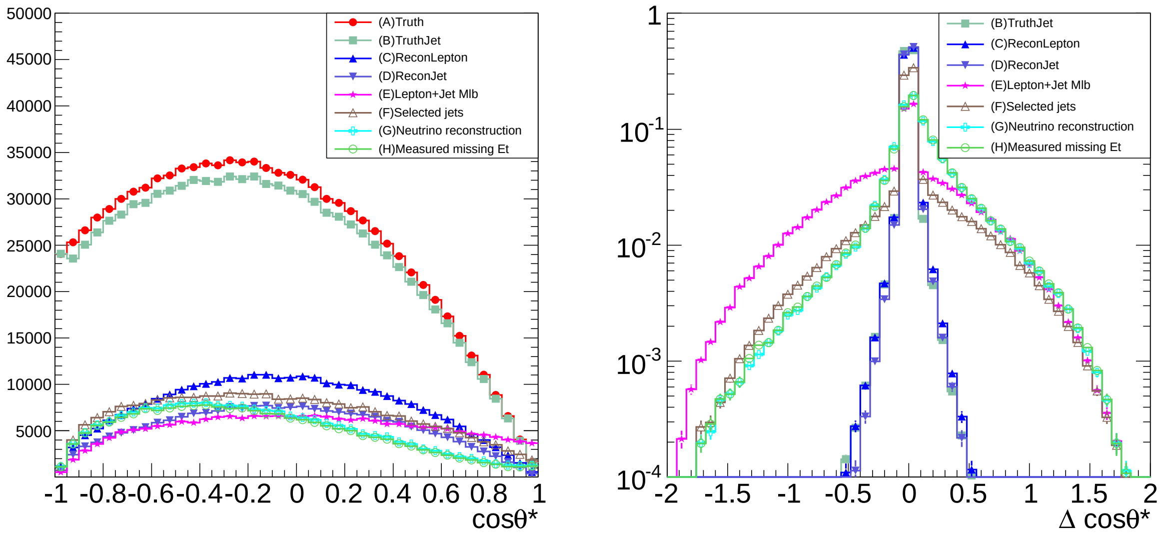

Figure 4.21: (left) The reconstructed $\cos\theta^*$ distribution with various sets of input which is summarized in Table 4.4. The Vertical axis is in arbitrary unit. (right) The difference between $\cos\theta^*$ reconstructed with each set of input in Table 4.4 and truth $\cos\theta^*$. The histograms are normalized to one.

of the wrongly-reconstructed side in the type (iii) and (iv) is the same as that of the reconstructed $\cos\theta^*$ with wrong jets in the case (v).

	two jets selection based on P_T and b-tagging	jet assignment to b,$\bar{b}$-quarks	fraction		resolution	
					mean	σ
(i)	both jets are appropriate	correct combination	63%		0.08	0.20
(ii)		wrong combination	15%		0.28	0.59
(iii)	at least one jet is not appropriate	jet assigned to $\bar{b}$-quark is correct	6%	$\bar{b}$ side	0.08	0.24
				b side	0.07	0.57
(iv)		jet assigned to b-quark is correct	6%	$\bar{b}$ side	0.07	0.59
				b side	0.07	0.23
(v)		either assigned jet is not correct	9%		0.11	0.58

Table 4.5: Summary of the mean and standard deviation σ of the $\cos\theta^*$ resolution. Column "resolution" shows the means and standard deviations (σ) of resolution distributions in Figure 4.22.

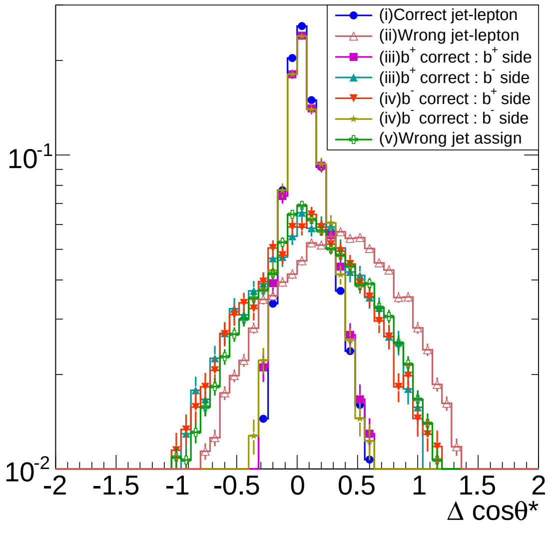

Figure 4.22: The $\cos\theta^*$ resolution distribution ($\Delta\cos\theta^* = \cos\theta^*_{\text{obtained}} - \cos\theta^*_{\text{truth}}$) of events in each categories in Table 4.5. Their means and standard deviations are summarized in the table.

4.3.3 Reconstructed top quark pair and $\cos\theta^*$

The top quark pair reconstruction method is applied onto the data. Table 4.6 shows the number of events after the reconstruction. Because the reconstruction procedure requires that the selected two jets, two charged leptons and missing E_T to have enough energy and appropriate kinematics to reconstruct two top quark system, the reconstruction procedure works also as an effective event selection and as the result, the signal-to-noise ratio is improved.

Event reconstruction	di-electron	di-muon	emu
ttbar signal	159.2 ± 27.5	319.8 ± 42.3	745.7 ± 100.4
Z(ee,$\mu\mu$)	0.7 ± 2.0	1.6 ± 4.2	-
Z($\tau\tau$)	0.0 ± 0.0	1.4 ± 1.3	4.7 ± 3.1
single top	5.0 ± 1.3	10.8 ± 2.4	24.8 ± 5.3
di-boson	0.2 ± 0.3	0.6 ± 0.3	1.3 ± 0.5
fake	4.3 ± 2.2	6.9 ± 3.5	18.6 ± 9.3
S/N	16	15	15
prediction	169.4 ± 27.7	341.1 ± 42.7	795.2 ± 101.0
data	191	354	836

Table 4.6: The Number of events after the event reconstruction in each channel. The uncertainties contain the statistical and the systematic ones which is discussed in section 4.4.1.

Figure 4.23 and 4.24 are the anti-neutrino and neutrino kinematics reconstructed by solving the simultaneous equations (4.9), (4.10), (4.11). Figure 4.27 shows the top quark mass with which the simultaneous equations have solved. Figure 4.25 and 4.26 are the reconstructed top quark kinematics. Finally, Figure 4.28 is the reconstructed $\cos\theta^*$ distributions.

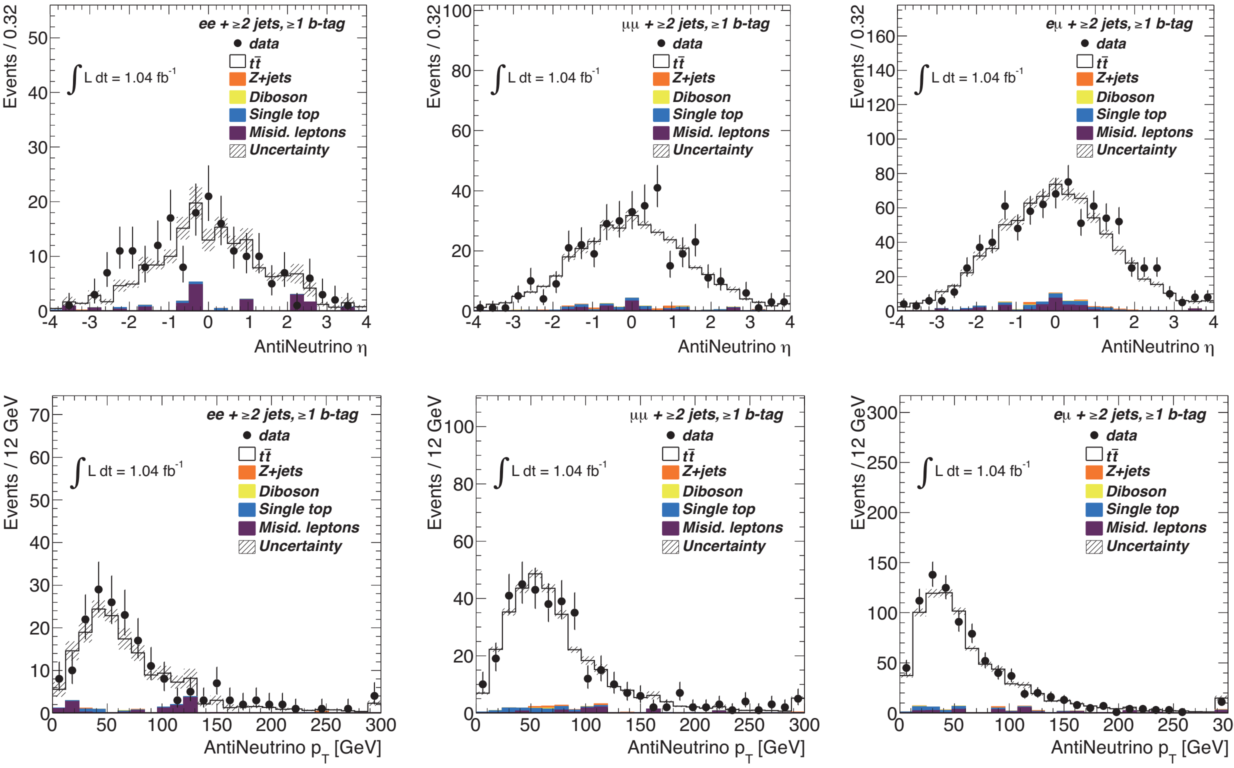

Figure 4.23: Reconstructed anti-neutrino η(top) and P_T(bottom) distributions in each channel. The MC simulation of the top quark pair is produced with the W boson polarization of F_L, F_0 and F_R in the SM. Only statistical uncertainty of the MC samples are shown in the figure.

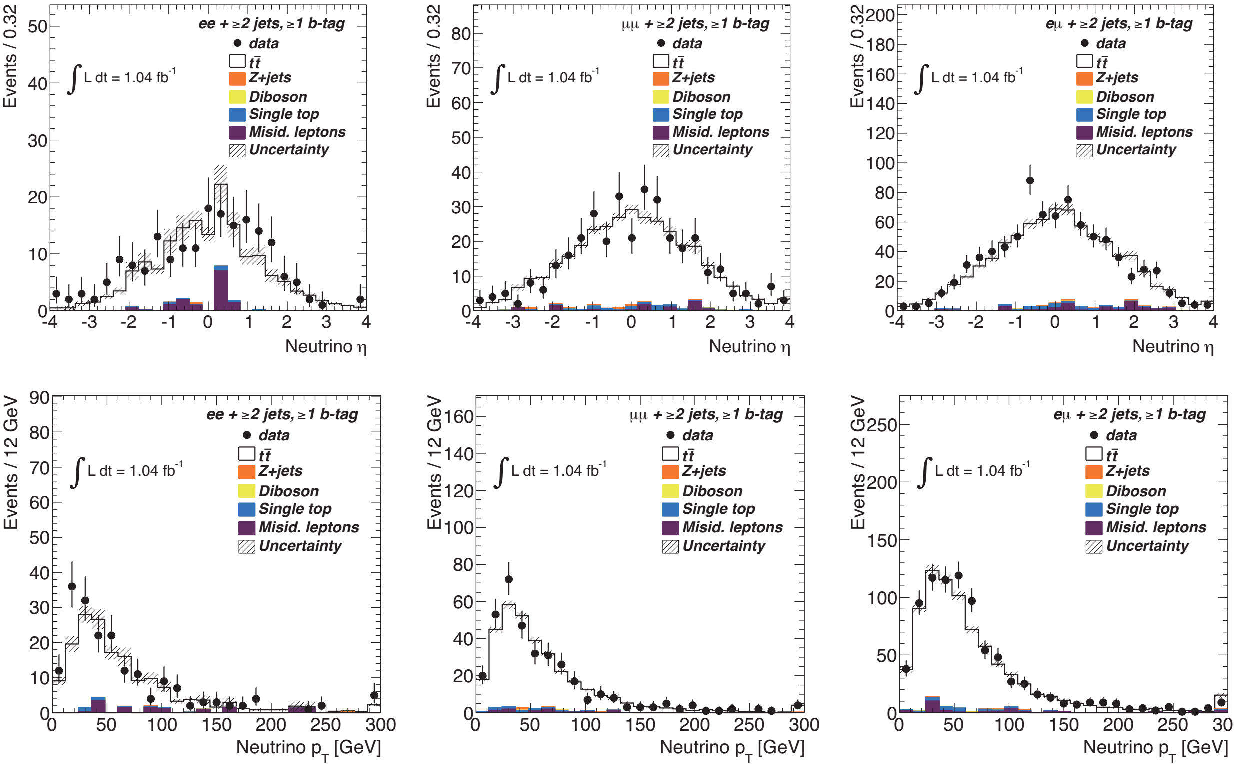

Figure 4.24: Reconstructed neutrino η(top) and P_T(bottom) distributions in each channel. The MC simulation of the top quark pair is produced with the W boson polarization of F_L, F_0 and F_R in the SM. Only statistical uncertainty of the MC samples are shown in the figure.

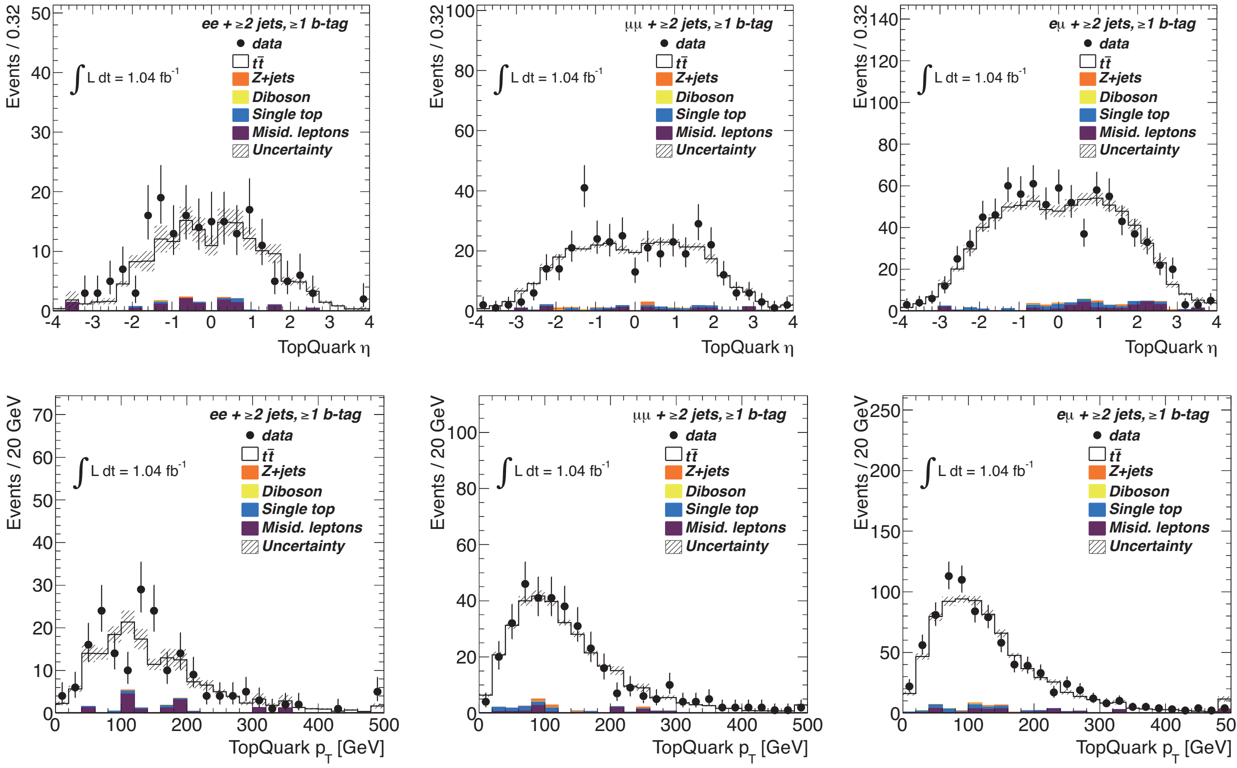

Figure 4.25: Reconstructed top quark η(top) and P_T(bottom) distributions in each channel. The MC simulation of the top quark pair is produced with the W boson polarization of F_L, F_0 and F_R in the SM. Only statistical uncertainty of the MC samples are shown in the figure.

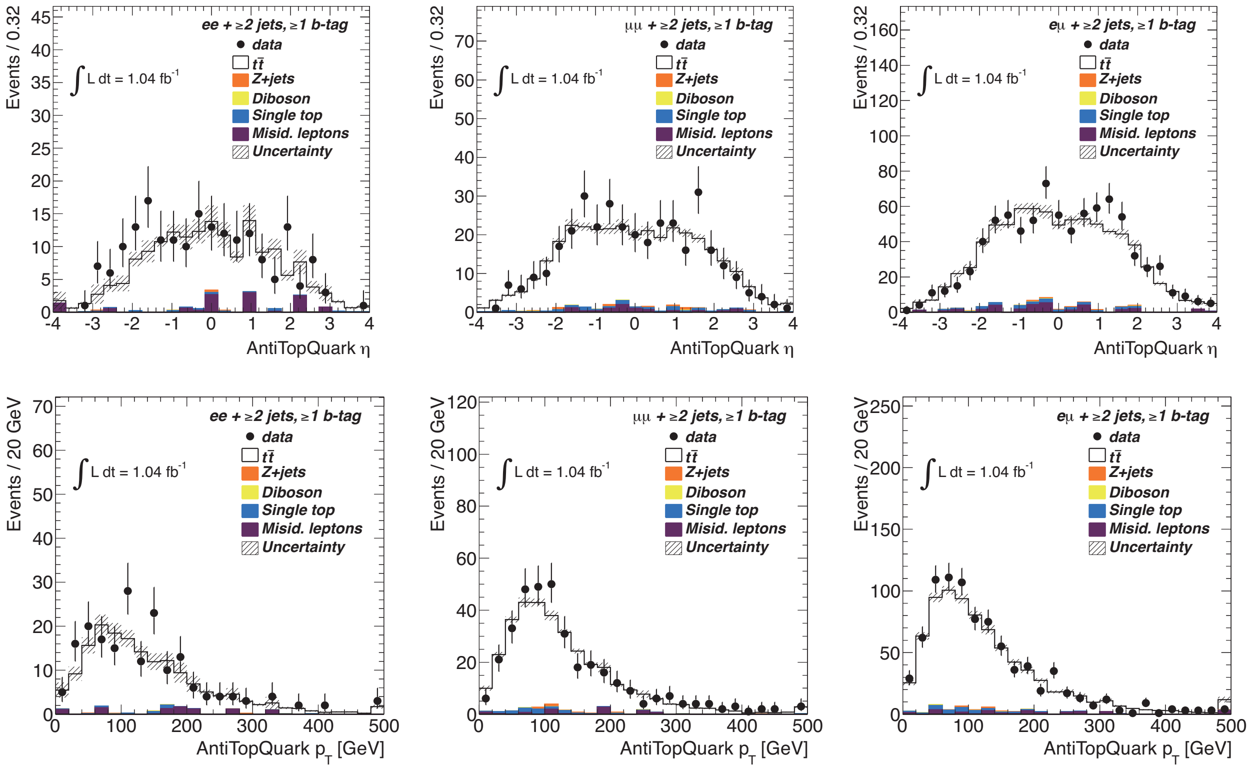

Figure 4.26: Reconstructed anti-top quark η(top) and P_T(bottom) distributions in each channel. The MC simulation of the top quark pair is produced with the W boson polarization of F_L, F_0 and F_R in the SM. Only statistical uncertainty of the MC samples are shown in the figure.

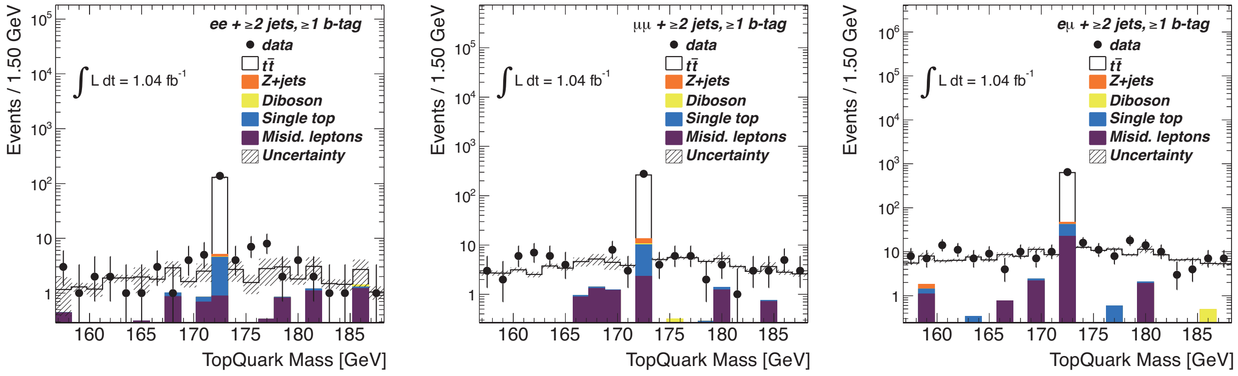

Figure 4.27: Reconstructed top quark mass distributions in each channel. The MC simulation of the top quark pair is produced with the W boson polarization of F_L, F_0 and F_R in the SM. Only statistical uncertainty of the MC samples are shown in the figure. The peak at 172.5 GeV means the solution is found at the first trial with input top quark mass of 172.5 GeV in the most events.

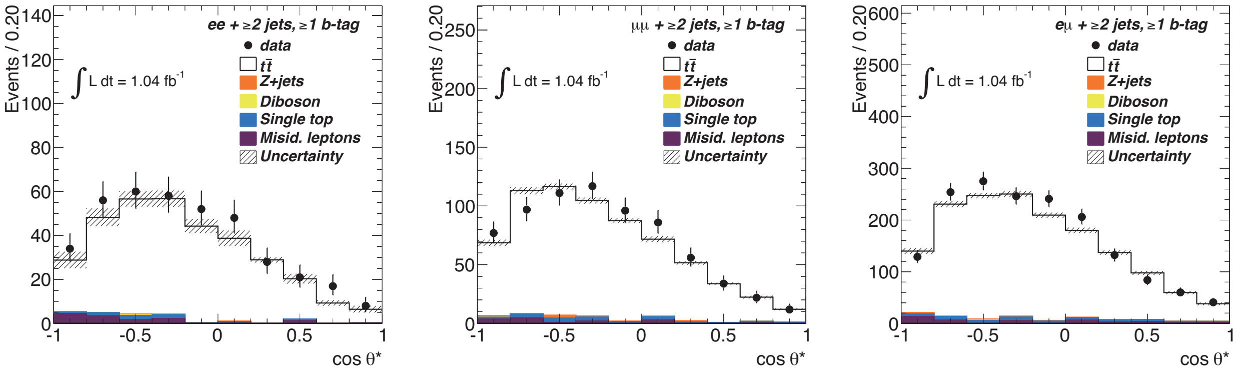

Figure 4.28: Reconstructed $\cos\theta^*$ distributions in each channel. The MC simulation of the top quark pair is produced with the W boson polarization of F_L, F_0 and F_R in the SM. Only statistical uncertainty of the MC samples are shown in the figure.

4.4 *W* Boson Polarization Measurement and its Physics Interpretation

From obtained $\cos\theta^*$ distribution, W boson polarization was measured. For this purpose, three $\cos\theta^*$ distributions in the top quark pair decay with W bosons fully polarized to left-, right-handed and longitudinal directions were prepared with MC simulation. Figure 4.29 shows the templates in each channel. Although the distribution is slightly distorted compared to the original shape of Figure 1.7 (right) due to resolution of the measurement and tendency of the reconstruction as shown in section 4.3.2, they still kept their characteristics so that they can be distinguished each other. Also the background distributions estimated at section 4.3.3 from each process is combined into one “background” distribution in each channel.

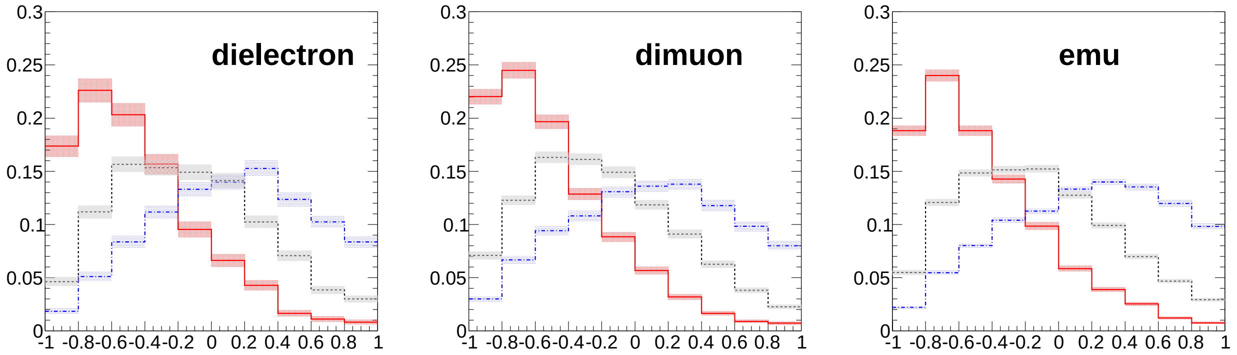

Figure 4.29: The templates shape in each channels. The red, gray and blue histograms represent left handed, longitudinal and right handed W boson polarization. The shadows stand for their statistical uncertainties.

The number of entries from each W boson helicity is extracted by the fit of the $\cos\theta^*$ distribution with four templates. The fit is performed based on the maximization of the likelihood defined as

$$L = \prod_{\mathrm{bin}=1}^{N_{\mathrm{bins}}} \mathrm{Poisson}(n_{bin}^{\mathrm{data}}; n_{bin}^{\mathrm{template}}) \times \exp\left(\frac{-(n_{BG}^{\mathrm{template}} - \bar{n}_{BG})^2}{2\sigma_{BG}^2}\right) \tag{4.12}$$

where

- n_{bin}^{data} : the number of entries in the *bin* in data.
- $n_{bin}^{\mathrm{template}} \equiv n_{0,bin}^{\mathrm{template}} + n_{\mathrm{L},bin}^{\mathrm{template}} + n_{\mathrm{R},bin}^{\mathrm{template}} + n_{\mathrm{BG},bin}^{\mathrm{template}}$
- $n_{\mathrm{L,0,R,BG}}^{\mathrm{template}}$: the number of entries in the bin i from each W boson helicity $L, 0$ and R, and BG=”background” component.
- $\bar{n}_{BG}$ and σ_{BG}: the expected background and its uncertainty as estimated at section 4.3.3.

The first part of the likelihood evaluates the possibility bin by bin postulating the Poisson distribution of data, and sums them up. The latter part is the constraint of the background to be around the expectation, which works as a *priori*.

The W boson polarization is calculated from the obtained entries with compensating the efficiency of the channel and helicity.

$$F_{\mathrm{hel}} = \frac{N_{\mathrm{hel}}}{\sum N_{\mathrm{hel}}}, \quad N_{\mathrm{hel}} = \frac{n_{\mathrm{hel}}}{\epsilon_{\mathrm{hel}}} = \frac{\sum_{i-\mathrm{bins}} n_{\mathrm{hel},i}}{\epsilon_{\mathrm{hel}}} \tag{4.13}$$

where the suffix “hel” is three types of helicity $L, 0, R$ of the W boson, and $\epsilon_{\mathrm{helicity}}$ is the event selection and reconstruction efficiency of each helicity in the channel.

The statistical uncertainty, or the covariant matrix $V_{i,j}$ of the measurement of n_i is estimated in the MINUIT from the second derivative as

$$V_{i,j}^{-1} = \left.\frac{\partial^2 \log L}{\partial n_i \partial n_j}\right|_{\boldsymbol{n}=\mathrm{measured}} \qquad (i = L, 0, R) \tag{4.14}$$

and V are the covariant matrix of F_i and n_i. The errors are propagated into the ones of F_i by

$$U_{I,J}^2 = \sum_{i}^{L,0,R} \sum_{j}^{L,0,R} V_{i,j} \Big(\frac{\partial F_I}{\partial n_i} \frac{\partial F_J}{\partial n_j} \Big)_{\boldsymbol{n}=\{n_0,n_L,n_R\}=\mathrm{measured}} \qquad (I, J = 0, L, R) \tag{4.15}$$

where $U_{I,J}$ is the covariant matrix of $\{F_I\}(I = 0, L, R)$.

The linearity and error estimation are verified by an ensemble test, before the fittings are performed to the data. The measurements have performed on 10,000 sets of $\cos\theta^*$ distributions made by fluctuating the histogram of nominal template entries bin-by-bin assuming the Poisson distribution assuming statistics of 1.04 fb^{-1}. Figure 4.30, 4.31, 4.32 show the pull distributions with respect to the input of the SM top quark pair. The pull is defined, for the measurement of some variable X, as

$$\mathrm{pull} = \frac{X_{\mathrm{measured}} - X_{\mathrm{center\ value}}}{\Delta X} \tag{4.16}$$

where ΔX is uncertainty on the measured value and the distribution is a Gaussian function with mean of 0 and standard deviation of 1, because errors are estimated so. From the figure, it is proven that the error is estimated appropriately. The linearity of the measurement are also verified by performing the analysis on the $\cos\theta^*$ distributions obtained from Monte Carlo simulation of various combination of fraction F_0, F_L, F_R.

- Figure 4.33 shows the linearity for the various combination of F_L, F_R with $F_0 = 0.7$.
- Figure 4.34 shows the linearity for the various combination of F_0, F_R with $F_L = 0.3$.
- Figure 4.35 shows the linearity for the various combination of F_0, F_L with $F_R = 0.0$.

In each case, linearity of the analysis is proven.

Figure 4.36 shows the results of the fit to the data, and Table 4.7 summarizes measured W boson polarization fluctuation in each channel. For a cross check of the analysis, the measurement by fixing $F_R = 0$ is performed. Table 4.8 shows the result. Here, the statistical uncertainties of F_L and F_R are identical in each channel, since $1 = F_L + F_R$ under the condition of $F_R = 0$. In the results, no strange tendency is seen.

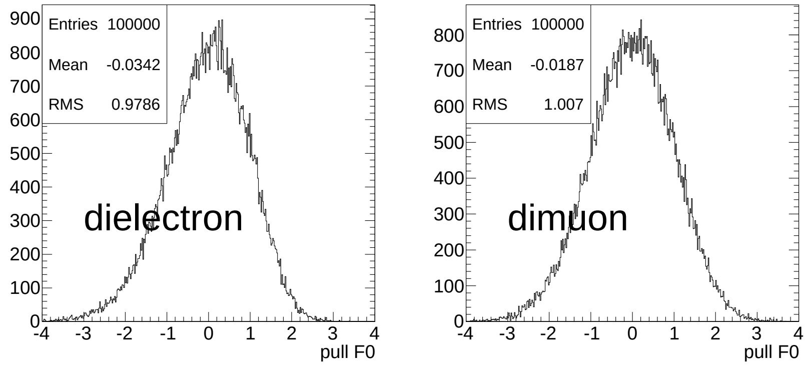

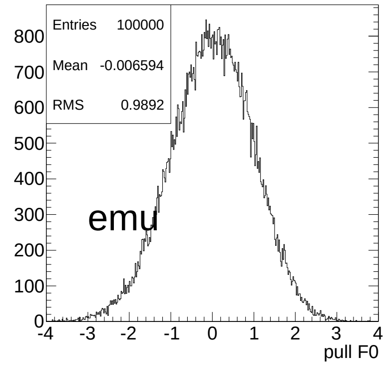

Figure 4.30: The pull distribution of F_0 in each channel with the input of the SM top quark pair production.

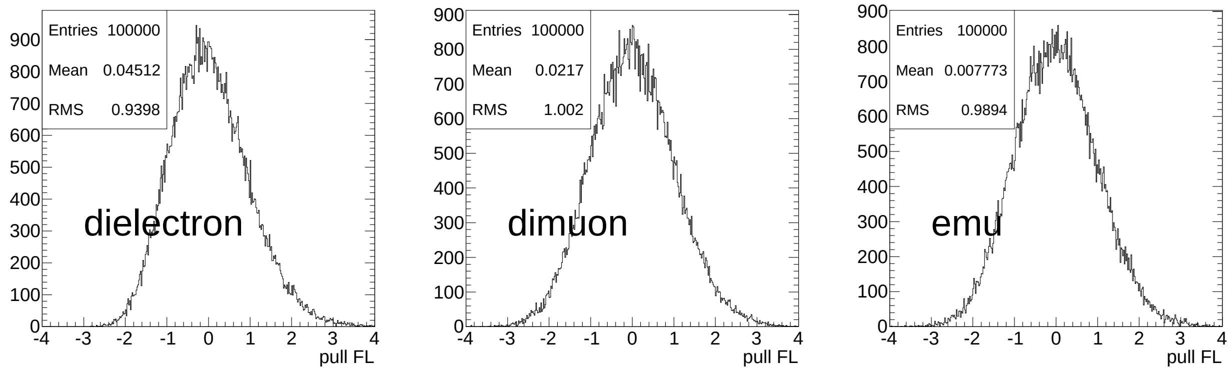

Figure 4.31: The pull distribution of F_L in each channel. with the input of the SM top quark pair production.

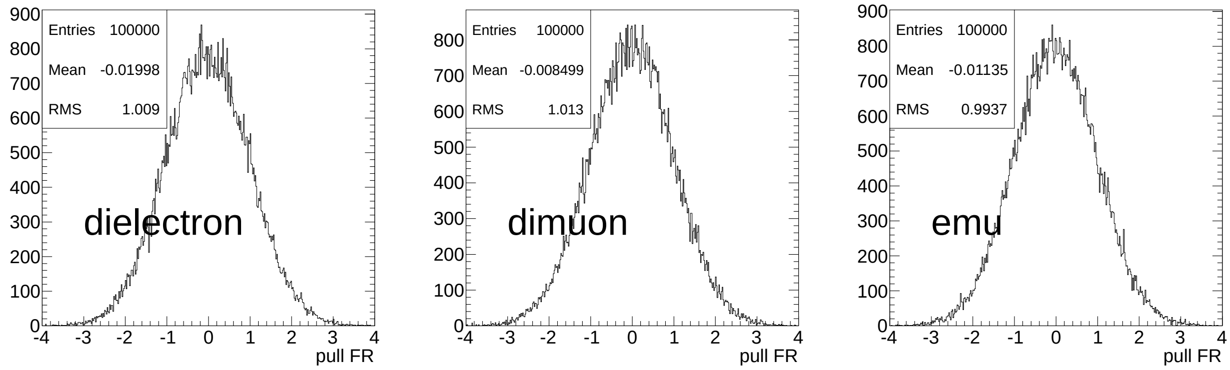

Figure 4.32: The pull distribution of F_R in each channel with the input of the SM top quark pair production.

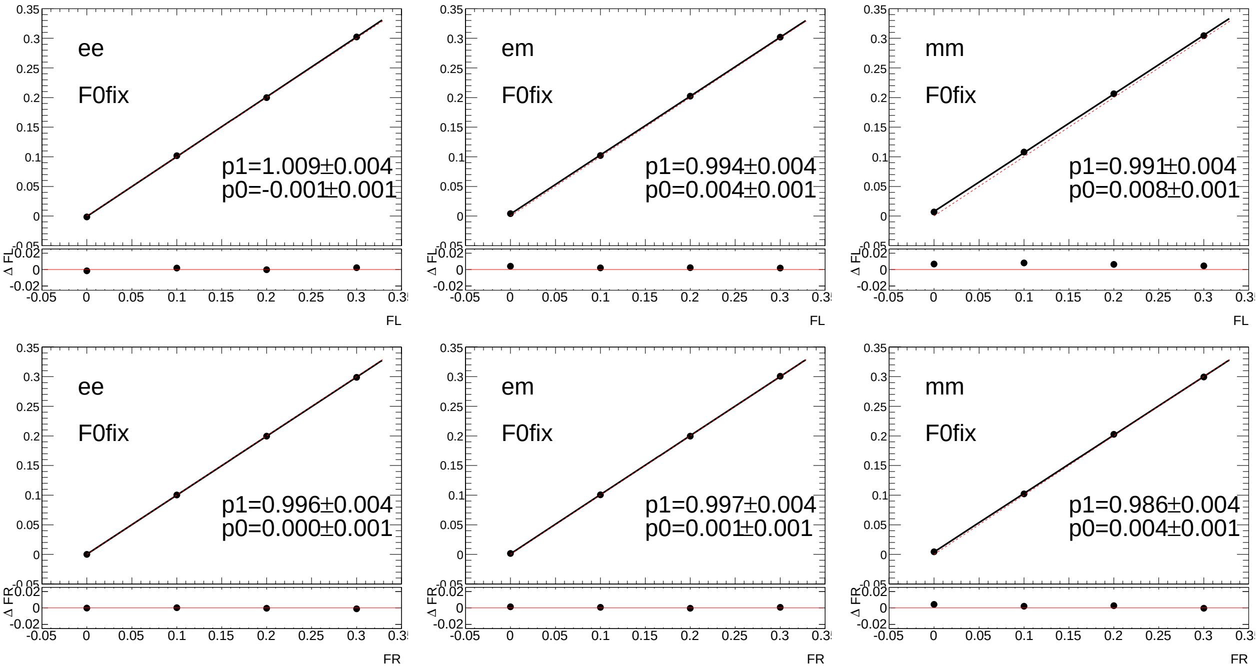

Figure 4.33: The linearlity of the F_L (top) and F_R (bottom) when $F_0 = 0.7$. Horizontal axes are the values of the input Monte Carlo sample and vertical axes are measured F_L and F_R.

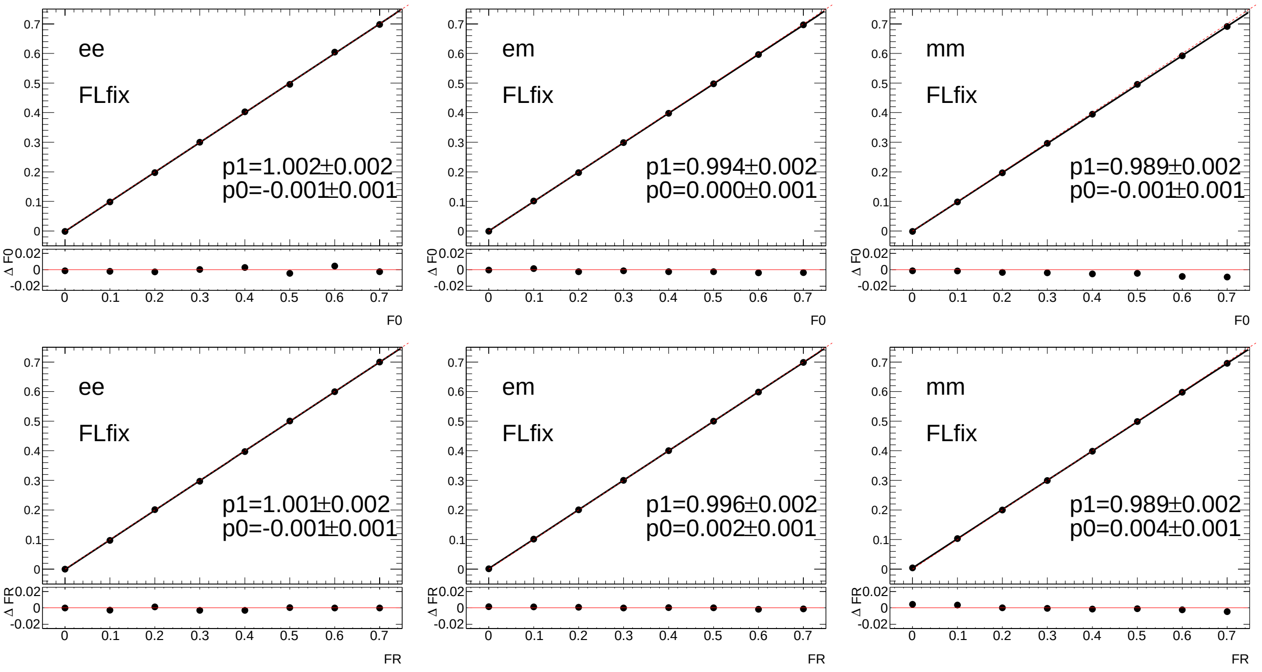

Figure 4.34: The linearlity of the F_0 (top) and F_R (bottom) when $F_L = 0.3$. Horizontal axes are the values of the input Monte Carlo sample and vertical axes are measured F_0 and F_R.

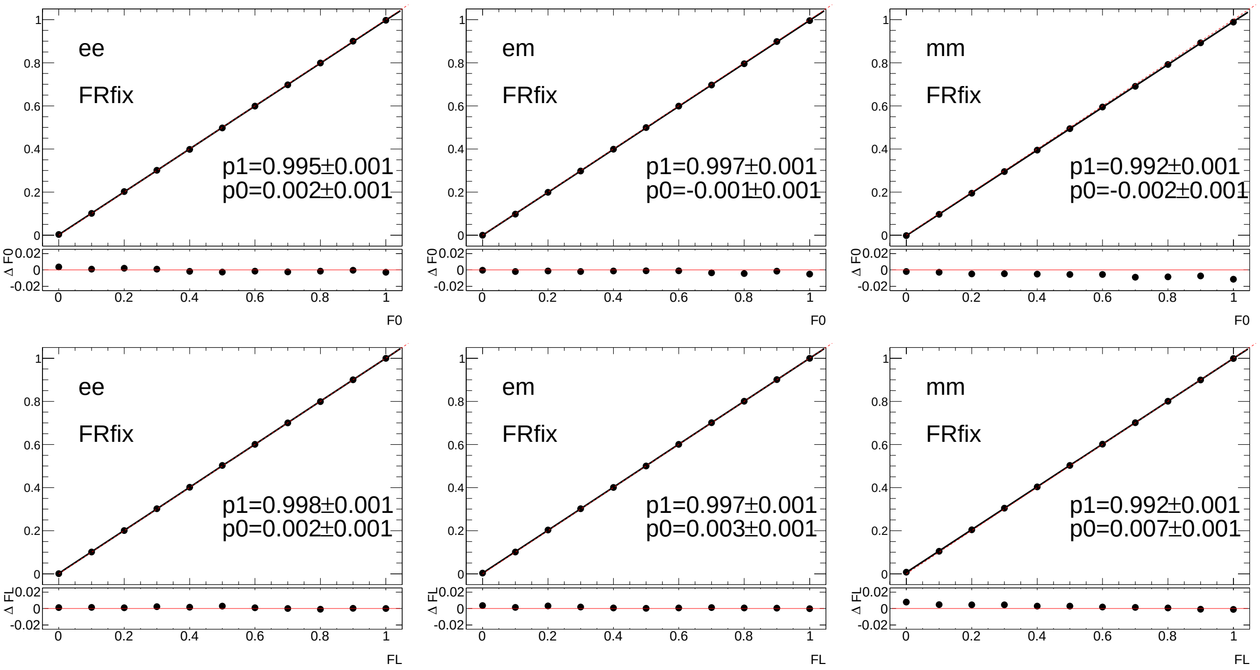

Figure 4.35: The linearity of the F_0 (top) and F_L (bottom) when $F_R = 0$. Horizontal axes are the values of the input Monte Carlo sample and vertical axes are measured F_0 and F_L.

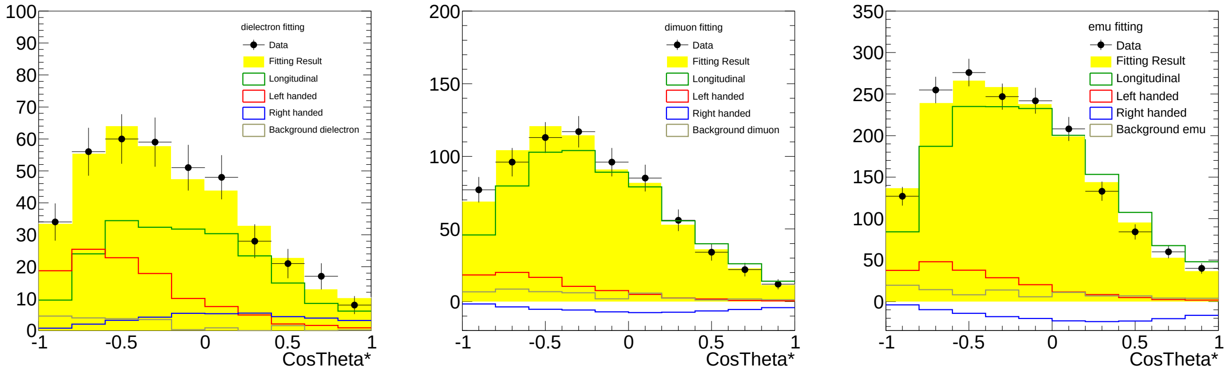

Figure 4.36: The result of the template fitting in each channel. In each, the yellow filled histogram is the sum of the three signals and the background, which are shown without stacking.

(stat only)	F_0	F_L	F_R
ee	0.566 ± 0.073	0.337 ± 0.042	0.097 ± 0.088
$\mu\mu$	0.620 ± 0.099	0.360 ± 0.043	0.020 ± 0.073
$e\mu$	0.896 ± 0.098	0.198 ± 0.068	-0.094 ± 0.066

Table 4.7: The result of the W boson polarization measurement in each channel. Statistical error only.

(stat only)	F_0	F_L
ee	0.634 ± 0.106	0.366 ± 0.106
$\mu\mu$	0.778 ± 0.070	0.222 ± 0.070
$e\mu$	0.704 ± 0.050	0.296 ± 0.050

Table 4.8: The result of the W boson polarization measurement with $F_R = 0$ fixed in the fitting ,in each channel. Statistical error only. The statistical errors of F_L and F_0 are identical in each channel since they are fully correlated $F_L + F_0 = 1$ under the condition of $F_R = 0$.

4.4.1 Evaluation of Systematic Uncertainties

The uncertainties of the polarization measurement due to the understanding of the detector performance and the description of physics process by simulation are taken into account as systematic uncertainties. The $\cos\theta^*$ distributions with various input sets are prepared, and the difference of the result of the W boson polarization fraction measurement between the nominal input set and each of them. The detail of the uncertainty sources and their effects to the $\cos\theta^*$ distribution are summarized below.

- Systematic uncertainties on the signal modeling

  PDF uncertainty

  As mentioned in section 2.3, CTEQ66 which is the PDF set used in this analysis, has 22 parameters with uncertainties. Also the differences among other PDF called MWST2008nlo68cl [41] and NNPDF20 [42], which use different functions to describe the PDF distributions, are taken into account.

  Monte Carlo generators

  The nominal input set uses the MC@NLO Monte Carlo generator. The uncertainty of the MC generator is estimated by comparing the results with the MC@NLO to that with the other generator named PowHeg [43]. Both of them based on the next-to-leading order (NLO) calculation but uses different way of the elimination of the overlap with parton shower calculation : MC@NLO produces partons in the angular-odering and it is tuned to only Herwig parton shower, while the PowHeg generator produces the hardest partons first and can be interfaced to any parton shower algorithm. In both simulations, Herwig parton shower algorithm is used in this uncertainty estimation.

  parton shower

  As the uncertainty from the parton shower modeling, the difference between HERWIG and PYTHIA samples generated by POWHEG generator is taken into account. Figure 4.37 shows the $\cos\theta^*$ distributions.

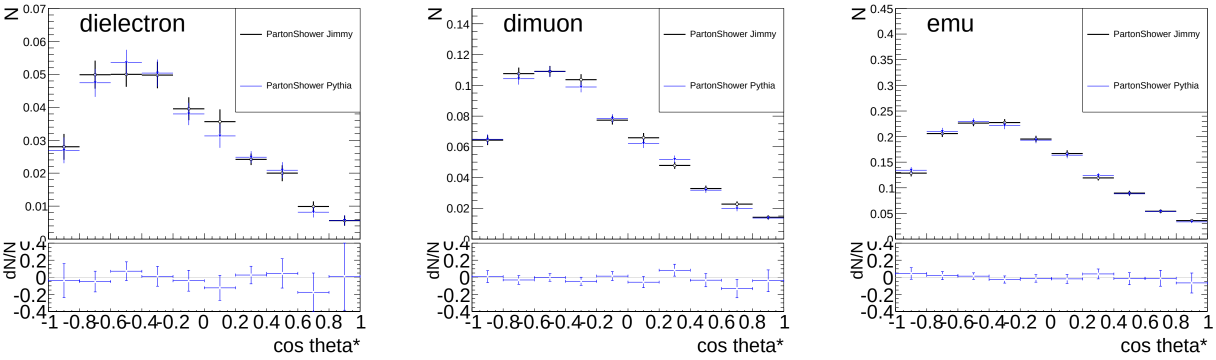

Figure 4.37: The nominal and modified $\cos\theta^*$ distribution by parton shower uncertainty. The histograms are normalized to 1 pb^{-1}.

ISR/FSR

The uncertainties of the gluon radiation from the initial state radiation (ISR) and final state radiation(FSR) is estimated by comparing a nominal Monte Carlo simulation with nominal setting to ones with increased(up)/decreased(down) ISR/FSR within the Perugia soft/hard tunes variations [44]. The tunes for the FSR and hadronization are done based on the results from the LEP experiment and ISR from the Tevatron experiments. The set of samples are ISR-up, ISR-down, FSR-up, FSR-down, both-up and both-down, in total six samples. Here, AcerMC Monte Carlo generator is used. Figure 4.38, 4.39 and 4.40 show the $\cos\theta^*$ distributions by modifying ISR, FSR and both, respectively.

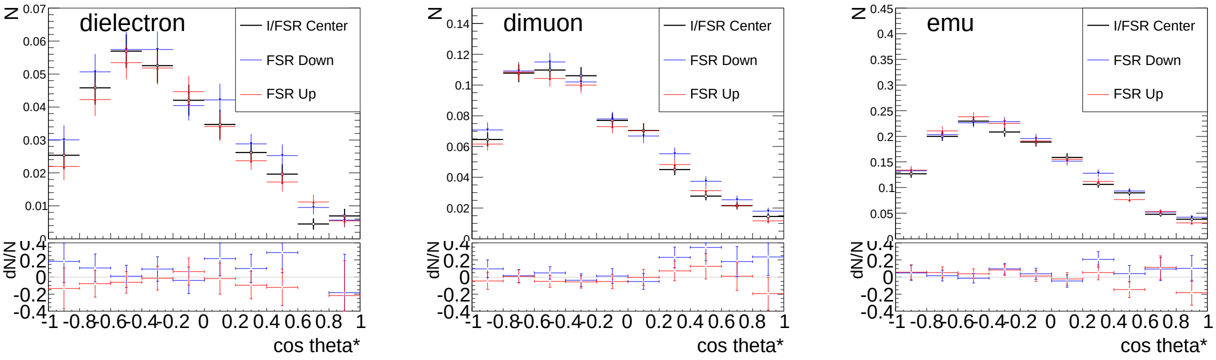

Figure 4.38: The nominal and modified $\cos\theta^*$ distribution by final state radiation uncertainty. The histograms are normalized to 1 pb^{-1}.

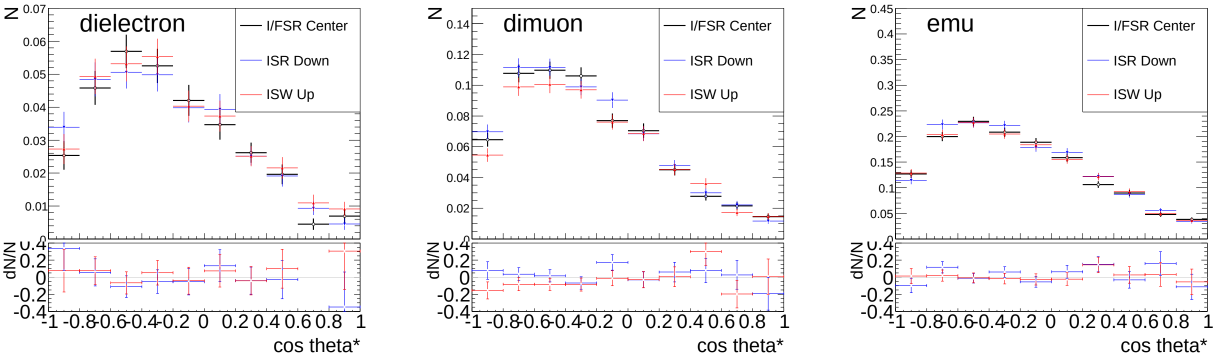

Figure 4.39: The nominal and modified $\cos\theta^*$ distribution by initial state radiation uncertainty. The histograms are normalized to 1 pb^{-1}.

The top quark mass

The nominal Monte Carlo simulation is produced with top quark mass of 172.5 GeV. The uncertainty comes from the assumption of the mass is evaluated by performing analysis on Monte Carlo simulated samples with top quark mass of 167.5, 170, 172.5(Nominal),

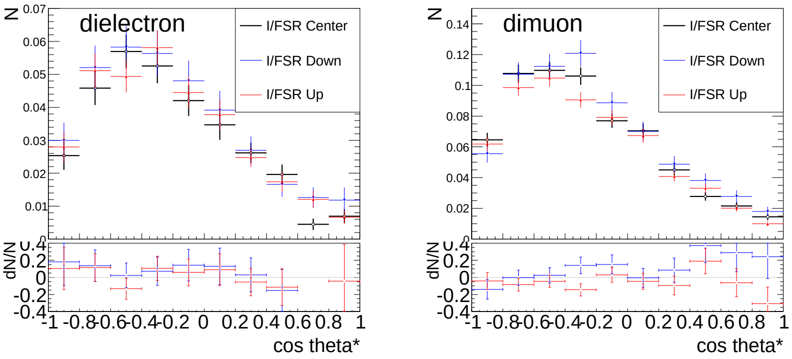

Figure 4.40: The nominal and modified $\cos\theta^*$ distribution by initial and final state radiation uncertainty.The histograms are normalized to 1 pb^{-1}.

175.0 and 175.5 GeV. Figure 4.41 shows the $\cos\theta^*$ distributions. From the results, the mass dependence is extracted by linear function fitting, and the uncertainty corresponding to the top quark mass uncertainty of 0.9 GeV is accounted for.

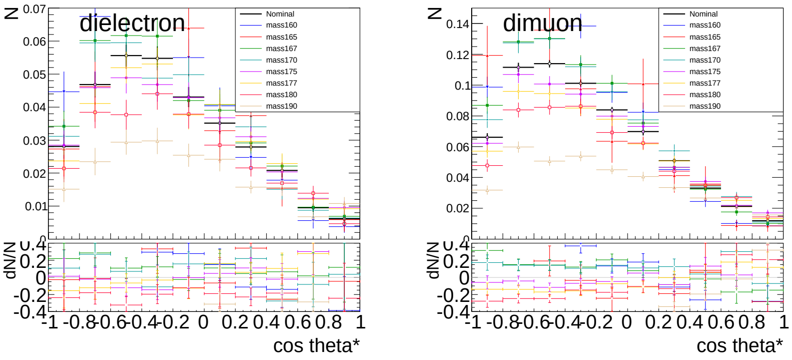

Figure 4.41: The nominal and modified $\cos\theta^*$ distribution by top quark mass uncertainty. The histograms are normalized to 1 pb^{-1}.

Theoretical cross section estimation on the backgrounds

The uncertainty of the theoretical cross section on the backgrounds has the effect on the number of the expected background in the fitting function. The cross section of the single top quark production associated with one W boson is expected to be $15.74^{+1.06}_{-1.08}$pb [45]. The uncertainty of the theoretical cross section of the di-boson is estimated as ±5% [46]. For Drell-Yan background, the treatment is different by the channels. In $e\mu$ channel, the background $Z \to \tau\tau \to e\nu\nu\mu\nu\nu$ is estimated with the Monte Carlo simulation assuming the cross section of theoretical prediction. The uncertainty on the ratio of the theoretical cross sections between one with n-partons and $n+1$ partons, that is $\sigma(Z+n+1 \text{ partons})/\sigma(Z+n \text{ partons})$ is estimated to be ±24 % [47]. The uncertainty is estimated by increasing and decreasing the Drell-Yan background by +24% (-24%) successively from $Z + 0$ to $Z + 5$ partons. In ee and $\mu\mu$ channels, the background is estimated from data. The uncertainty from the estimation is evaluated by changing the scale factor applied onto the Monte Carlo simulation as discussed in section 4.2.2 and summarized in Table 4.1 and performing the same as the single top background estimation above.

The uncertainties from these items are estimated by performing the analysis on the Monte Carlo simulated sample where the cross section of the single top quark background is increased and decreased by their uncertainties while the number of background expectation in the fitting is fixed. The maximum deviation from the nominal result is taken into account, in each background component.

- Systematic uncertainties from detector modeling.

Jet energy scale

In addition to the jet energy scale uncertainties summarized in section 2.4.5, uncertainty due to the number of pile-up events is added depending on the region of the η and jet P_T.

- $|\eta| < 2.1$, $p_T < 50$ GeV : 5 %
- $|\eta| < 2.1$, $50 < p_T < 100$ GeV : 2%
- $2.1 < |\eta|$, $p_T < 50$ GeV : 7 %
- $2.1 < |\eta|$, $50 < p_T < 100$ GeV : 3%.

For b-tagged jets, in addition to the uncertainties described above, 2.5% uncertainty is added. These uncertainties are added in quadrature. Figure 4.42 and 4.43 show the $\cos\theta^*$ distributions.

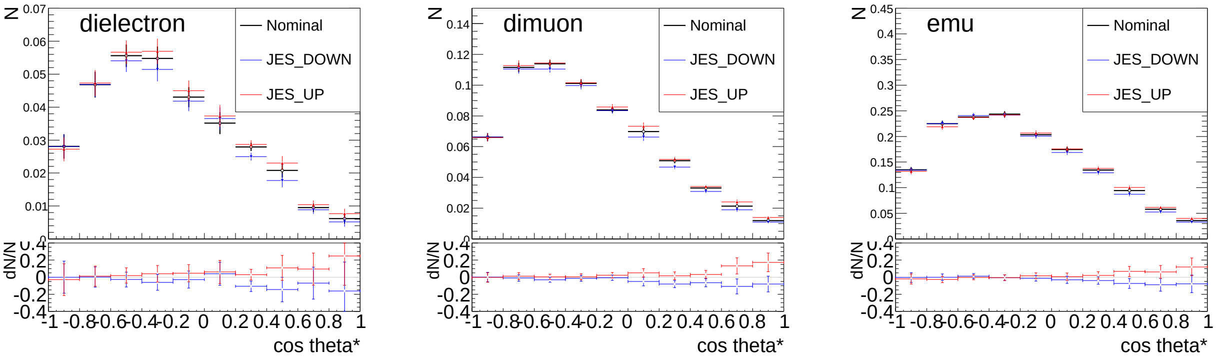

Figure 4.42: The nominal and modified $\cos\theta^*$ distribution by jet energy scale uncertainty. The histograms are normalized to 1 pb^{-1}.

Jet energy resolution

The uncertainty due to the jet energy resolution is estimated by smearing momenta of jets in Monte Carlo simulation by the uncertainty discussed in section 2.4.5. Figure 4.44 shows the $\cos\theta^*$ distributions.

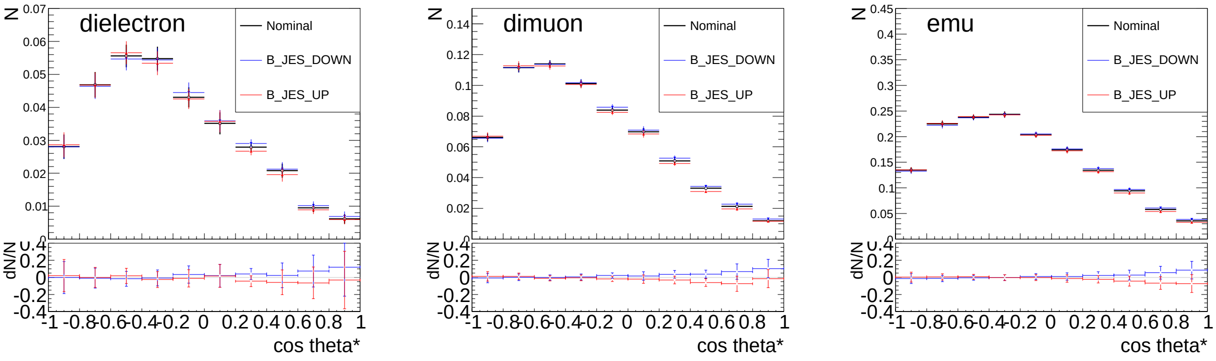

Figure 4.43: The nominal and modified $\cos\theta^{*}$ distribution by b-quark jet energy scale factor uncertainty. The histograms are normalized to 1 pb^{-1}.

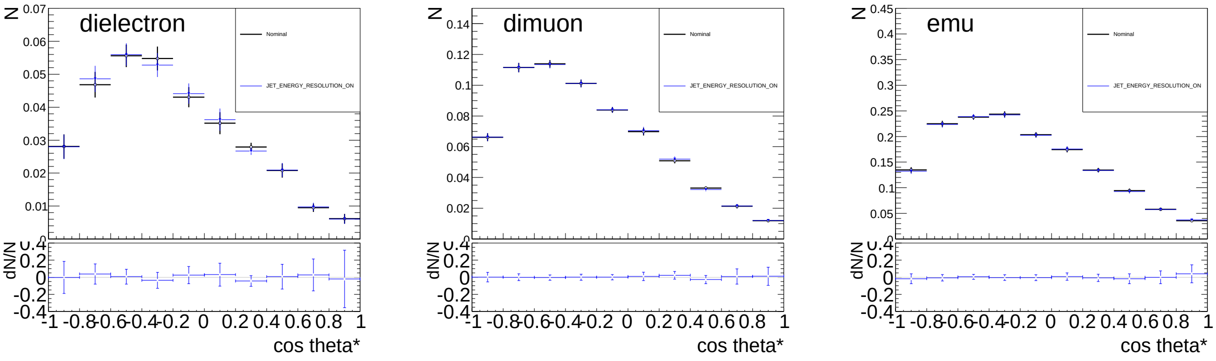

Figure 4.44: The nominal and modified $\cos\theta^{*}$ distribution by b-quark jet energy resolution uncertainty. The histograms are normalized to 1 pb^{-1}.

Jet reconstruction efficiency

The uncertainty due to the jet reconstruction efficiency is estimated by removing reconstructed jets randomly from Monte Carlo simulation samples based on the uncertainty of the efficiency.

Lepton measurement

As the uncertainty from the understanding of the energy scale and the resolution of the charged leptons, the scale factors, which is applied onto the Monte Carlo simulation in order to compensate the difference between the data and produced simulation as discussed in section 2.4.2(electron) and 2.4.2(muon), are shifted by their uncertainties.

Trigger efficiency

The uncertainty from the trigger efficiency discussed in section 2.5.1 is estimated by shifting the scale factor by its uncertainty.

***b*-tagging scale factors**

Uncertainties due to the b-tagging efficiency and the fake rate are estimated by varying the scale factors applied on the Monte Carlo simulation by their uncertainties as discussed in section 2.4.6. They are added in quadrature. Figure 4.45 and 4.46 show the $\cos\theta^*$ distributions for uncertainties of b-tagging efficiency and fake rate respectively. It is worth mentioning that the number of events that pass the selection and reconstruction criteria is effected much by the uncertainty but it does not change the shape of the $\cos\theta^*$ distribution. Therefore, the uncertainty on the W boson polarization measurement due to the b-tagging uncertainty is small.

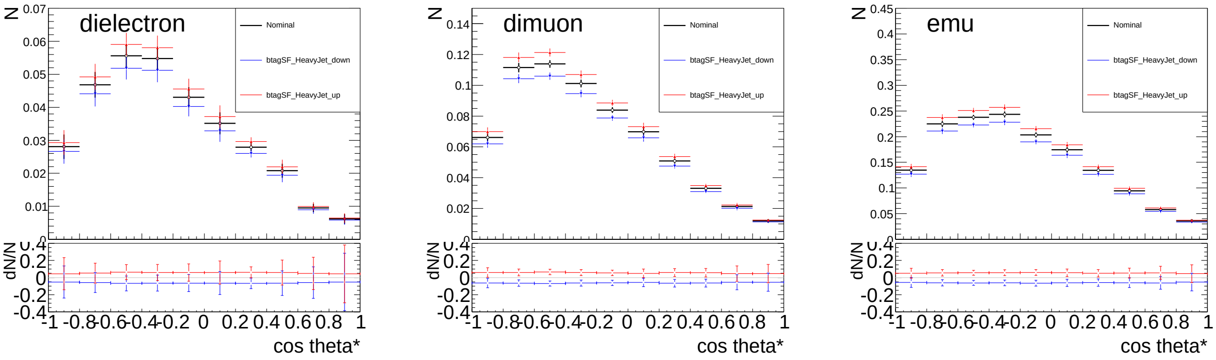

Figure 4.45: The nominal and modified $\cos\theta^*$ distribution by b-tagging scale factor uncertainty. The histograms are normalized to 1 pb^{-1}.

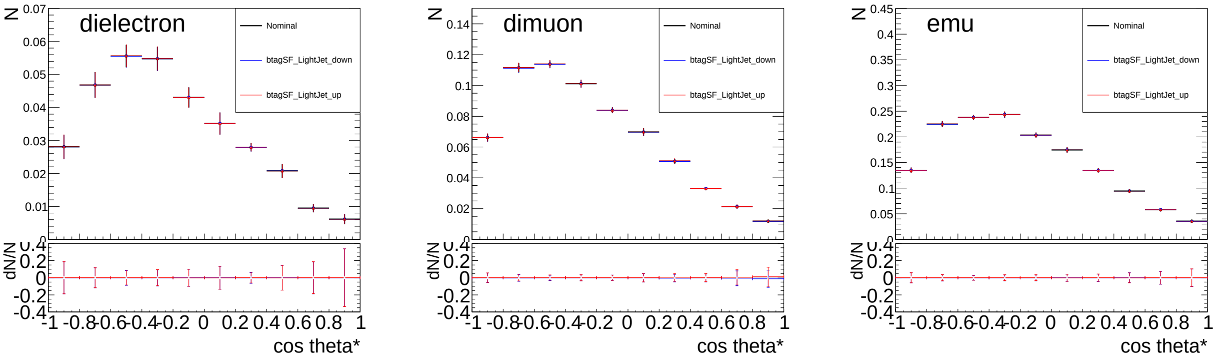

Figure 4.46: The nominal and modified $\cos\theta^*$ distribution by b-tagging fake rate scale factor uncertainty. The histograms are normalized to 1 pb^{-1}.

Fake background estimation

The uncertainty from the estimation of fake background is estimated by changing the scale factor by ±50 % conservatively.

Color re-connection

The uncertainty due to the color re-connection modeling in the hadronization process is estimated as the difference between the color re-connection on and off in the Monte Carlo simulation. In practical, the comparison between ACERMC using Perugia2010 tune [44] with and without color re-connection, and A-Pro and ACR-Pro tunes [48], [49]. The larger deviation is taken into account as the systematic uncertainty. Figure 4.47 and 4.48 show the $\cos\theta^{*}$ distributions for the former and the latter.

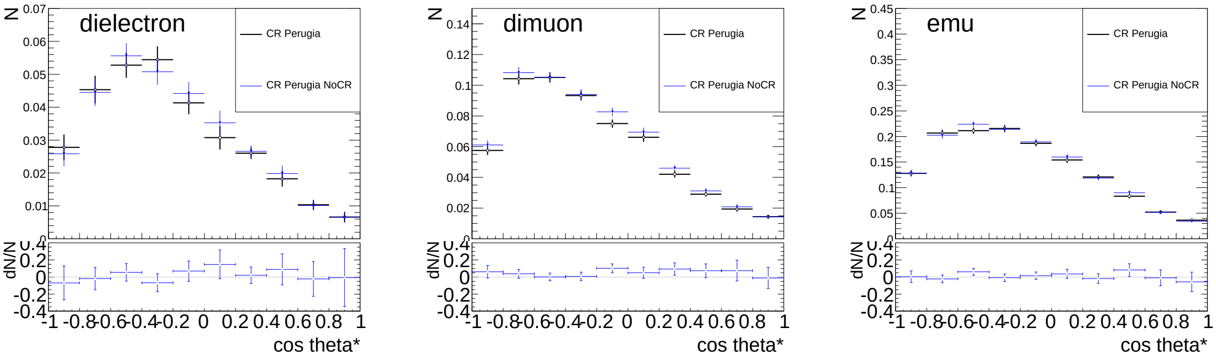

Figure 4.47: The nominal and modified $\cos\theta^{*}$ distribution by color re-connection uncertainty, comparing ACERMC with Perugia2010 with and without color re-connection. The histograms are normalized to 1 pb^{-1}.

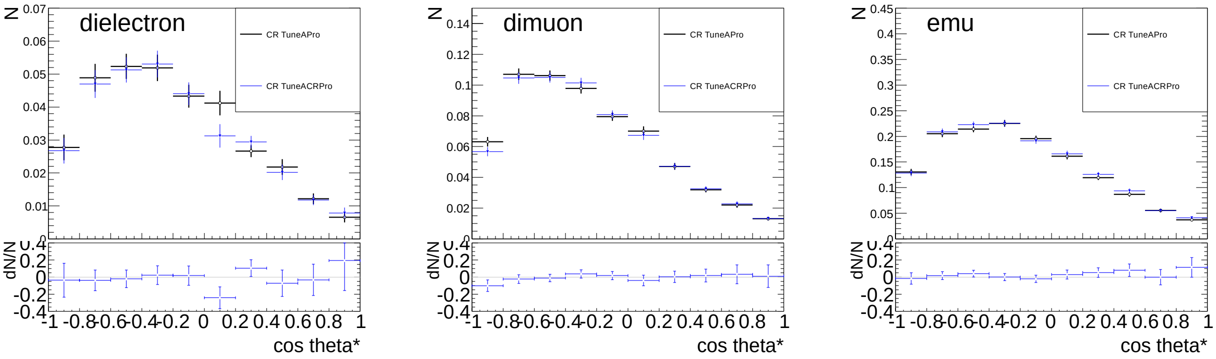

Figure 4.48: The nominal and modified $\cos\theta^{*}$ distribution by color re-connection uncertainty, comparing and A-Pro and ACR-Pro tunes. The histograms are normalized to 1 pb^{-1}.

Missing E_T measurement

In the missing E_T measurement, 10% uncertainty on the cell-out term in the missing E_T calculation of equation (2.21) is added as an uncertainty from the pile-up effect.

LAr detector hole

As discussed in the section 2.3, the problem of the LAr hole is emulated in the Monte Carlo simulation by removing reconstructed jets and electrons in the region randomly with the ratio of data accumulated period with and without the hole. The uncertainty of the way of the hole modeling is estimated by changing the threshold of jets $P_T = 20$ GeV by ± 4 GeV.

Statistics of the templates

The uncertainty arises from statistics of the templates is estimated by performing the fitting by replacing the templates. The alternative templates are prepared by fluctuating the entries in each bin assuming the Poisson distribution. 5,000 sets of the template for the signals and backgrounds are used, and the standard deviation of the measurement results is taken into account as the uncertainty.

data luminosity

The integrated luminosity of the data used in this analysis has the uncertainty of 3.7%. In this analysis, the amount of background estimated from Monte Carlo simulation is scaled to the integrated luminosity based on the theoretical cross section calculation, and in the fitting, the expected number of background are used as a priori in the likelihood (equation (4.12)). The uncertainty is estimated by increasing and decreasing the background entries by the luminosity uncertainty, and performing analysis on it with the number of expected background in the likelihood function fixed.

	ee			$\mu\mu$			$e\mu$		
	F_0	F_L	F_R	F_0	F_L	F_R	F_0	F_L	F_R
Signal MC	0.157	0.099	0.065	0.131	0.069	0.080	0.050	0.040	0.022
TopMass	0.001	0.011	0.009	0.008	0.008	0.016	0.006	0.006	0.012
I/FSR	0.175	0.112	0.069	0.114	0.092	0.087	0.062	0.033	0.042
Background	0.010	0.006	0.005	0.004	0.002	0.003	0.004	0.004	0.001
Fake estimation	0.042	0.048	0.006	0.017	0.015	0.002	0.039	0.026	0.013
Luminosity	0.011	0.009	0.005	0.007	0.004	0.004	0.006	0.005	0.002
LAr	0.011	0.004	0.007	0.007	0.003	0.003	0.001	0.000	0.001
Lepton SF	0.010	0.007	0.004	0.007	0.005	0.004	0.005	0.003	0.002
Lepton momentum	0.021	0.008	0.014	0.008	0.004	0.005	0.007	0.003	0.004
JES	0.032	0.038	0.048	0.054	0.028	0.059	0.029	0.023	0.036
JER	0.048	0.022	0.036	0.047	0.022	0.026	0.027	0.014	0.014
b-tag	0.014	0.006	0.008	0.005	0.006	0.005	0.003	0.001	0.002
Template MC stat.	0.049	0.071	0.027	0.041	0.064	0.028	0.031	0.043	0.017
PDF	0.010	0.008	0.004	0.007	0.004	0.005	0.007	0.004	0.003
Syst Sum	0.253	0.179	0.118	0.194	0.137	0.139	0.104	0.078	0.066
Stat	0.182	0.118	0.092	0.162	0.088	0.092	0.098	0.068	0.039

Table 4.9: Systematic and statistical uncertainties in each channels of the di-lepton channel.

The Table 4.9 summarize the systematic uncertainties, and they are added in quadrature. The measurement result of the W boson polarization in each channel is

$$\begin{aligned} ee \text{ channel :} F_0 &= 0.484 \pm 0.182(\text{stat.}) \pm 0.253(\text{syst.}) & (4.17)\\ F_L &= 0.429 \pm 0.118(\text{stat.}) \pm 0.179(\text{syst.}) & (4.18)\\ F_R &= 0.087 \pm 0.092(\text{stat.}) \pm 0.118(\text{syst.}) & (4.19)\\ \mu\mu \text{ channel :} F_0 &= 0.927 \pm 0.162(\text{stat.}) \pm 0.194(\text{syst.}) & (4.20)\\ F_L &= 0.169 \pm 0.088(\text{stat.}) \pm 0.137(\text{syst.}) & (4.21)\\ F_R &= -0.096 \pm 0.088(\text{stat.}) \pm 0.137(\text{syst.}) & (4.22)\\ e\mu \text{ channel :} F_0 &= 0.896 \pm 0.098(\text{stat.}) \pm 0.104(\text{syst.}) & (4.23)\\ F_L &= 0.198 \pm 0.068(\text{stat.}) \pm 0.078(\text{syst.}) & (4.24)\\ F_R &= -0.094 \pm 0.039(\text{stat.}) \pm 0.066(\text{syst.}) & (4.25) \end{aligned}$$

In the same way, the uncertainty of $F_R = 0$ fixed measurement is estimated and summarized in the Table 4.10. As statistical uncertainty, the systematic uncertainties of F_L and F_0 are fully correlated under the constraint of $1 = F_L + F_0$. In total, the measurement with $F_R = 0$ fixed measurements are

$$\begin{aligned} ee \text{ channel :} F_0 &= 0.634 \pm 0.106(\text{stat.}) \pm 0.149(\text{syst.}) & (4.26)\\ F_L &= 0.366 \pm 0.106(\text{stat.}) \pm 0.149(\text{syst.}) & (4.27)\\ \mu\mu \text{ channel :} F_0 &= 0.778 \pm 0.070(\text{stat.}) \pm 0.122(\text{syst.}) & (4.28)\\ F_L &= 0.222 \pm 0.070(\text{stat.}) \pm 0.122(\text{syst.}) & (4.29)\\ e\mu \text{ channel :} F_0 &= 0.704 \pm 0.050(\text{stat.}) \pm 0.090(\text{syst.}) & (4.30)\\ F_L &= 0.296 \pm 0.050(\text{stat.}) \pm 0.090(\text{syst.}) & (4.31) \end{aligned}$$

and no deviation from the Standard Model is seen neither.

4.4.2 Combination of the Results with BLUE method.

These results were combined, taking into account their uncertainties, by a mathematical method, so called *Best Unbiased Linear Estimator*(BLUE) [50] [51]. The method gives a combination of the results linearly so that combined variance is minimized. Suppose that one performs n times measurements of some quantities X and Y, and obtains sets of results $x_1, x_2, ..., x_n = x_i$ and y_i with $2n \times 2n$ covariant matrix E, the combined results x and y by the method are

$$\begin{pmatrix} x \\ y \end{pmatrix} = \begin{pmatrix} \omega_1^x & \cdots & \omega_{2n}^x \\ \omega_1^y & \cdots & \omega_{2n}^y \end{pmatrix} \begin{pmatrix} x_1 \\ \vdots \\ x_n \\ y_1 \\ \vdots \\ y_n \end{pmatrix} \tag{4.32}$$

	ee F_0 , F_L	$\mu\mu$ F_0 , F_L	$e\mu$ F_0 , F_L
Signal MC	0.061	0.056	0.043
TopMass	0.019	0.017	0.018
I/FSR	0.088	0.088	0.047
Background	0.003	0.002	0.004
Fake	0.055	0.014	0.012
Luminosity	0.009	0.001	0.004
LAr	0.002	0.001	0.001
Lepton SF	0.005	0.003	0.002
Lepton momentum	0.008	0.003	0.005
JES	0.071	0.048	0.054
JER	0.014	0.005	0.007
b-tag	0.002	0.006	0.002
Template MC stat.	0.032	0.032	0.023
PDF	0.005	0.006	0.003
Syst Sum	0.149	0.122	0.090
Stat	0.106	0.070	0.050

Table 4.10: Systematic and statistical uncertainties in each channels of the di-lepton channel in F_R fixing measurement

where the set of ω_i is constant weights and satisfy $\sum_i^{2n} \omega_i^x = 1$ and $\sum_i^{2n} \omega_i^y = 1$. The method determines the weights so that combined covariance

$$\sigma^2_{x(y)} = \begin{pmatrix} \omega_1^{x(y)} & \dots & \omega_{2n}^{x(y)} \end{pmatrix} E \begin{pmatrix} \omega_1^{x(y)} \\ \dots \\ \omega_{2n}^{x(y)} \end{pmatrix} \tag{4.33}$$

is minimized.

The combined results are unbiased as long as the measurement results are unbiased. The word “best” in the method name stands for the fact that the method gives the results with the smallest covariance in the methods that perform the liner combination and are unbiased.

In the combination, the correlation of the systematic uncertainties need to be taken into account. Generally speaking, measurements with the same instruments and/or methods are affected by the same systematic uncertainties. These correlation information are set into covariant matrix E as discussed in section 4.4.3.

The quantities x and y corresponds to two of the fraction F_L, F_0, F_R in this analysis. This time, F_L and F_0 are adapted. The n times measurements correspond to measurements in different channels and method. The covariant matrix E is discussed below.

4.4.3 Combination of the di-lepton channels

The measurements results are put into the matrix :

$$\begin{pmatrix} F_0^{ee} \\ F_0^{e\mu} \\ F_0^{\mu\mu} \\ F_L^{ee} \\ F_L^{e\mu} \\ F_L^{\mu\mu} \end{pmatrix} \tag{4.34}$$

and covariant matrix E is

$$E = \begin{pmatrix} \rho(F_0^{ee}, F_0^{ee}) & \rho(F_0^{ee}, F_0^{e\mu}) & \rho(F_0^{ee}, F_0^{\mu\mu}) & \rho(F_0^{ee}, F_L^{ee}) & \rho(F_0^{ee}, F_L^{e\mu}) & \rho(F_0^{ee}, F_L^{\mu\mu}) \\ \rho(F_0^{e\mu}, F_0^{ee}) & \rho(F_0^{e\mu}, F_0^{e\mu}) & \rho(F_0^{e\mu}, F_0^{\mu\mu}) & \rho(F_0^{e\mu}, F_L^{ee}) & \rho(F_0^{e\mu}, F_L^{e\mu}) & \rho(F_0^{e\mu}, F_L^{\mu\mu}) \\ \rho(F_0^{\mu\mu}, F_0^{ee}) & \rho(F_0^{\mu\mu}, F_0^{e\mu}) & \rho(F_0^{\mu\mu}, F_0^{\mu\mu}) & \rho(F_0^{\mu\mu}, F_L^{ee}) & \rho(F_0^{\mu\mu}, F_L^{e\mu}) & \rho(F_0^{\mu\mu}, F_L^{\mu\mu}) \\ \rho(F_L^{ee}, F_0^{ee}) & \rho(F_L^{ee}, F_0^{e\mu}) & \rho(F_L^{ee}, F_0^{\mu\mu}) & \rho(F_L^{ee}, F_L^{ee}) & \rho(F_L^{ee}, F_L^{e\mu}) & \rho(F_L^{ee}, F_L^{\mu\mu}) \\ \rho(F_L^{e\mu}, F_0^{ee}) & \rho(F_L^{e\mu}, F_0^{e\mu}) & \rho(F_L^{e\mu}, F_0^{\mu\mu}) & \rho(F_L^{e\mu}, F_L^{ee}) & \rho(F_L^{e\mu}, F_L^{e\mu}) & \rho(F_L^{e\mu}, F_L^{\mu\mu}) \\ \rho(F_L^{\mu\mu}, F_0^{ee}) & \rho(F_L^{\mu\mu}, F_0^{e\mu}) & \rho(F_L^{\mu\mu}, F_0^{\mu\mu}) & \rho(F_L^{\mu\mu}, F_L^{ee}) & \rho(F_L^{\mu\mu}, F_L^{e\mu}) & \rho(F_L^{\mu\mu}, F_L^{\mu\mu}) \end{pmatrix} \tag{4.35}$$

where ρ means the correlation between two parameters.

The measurements of F_L, F_0 and F_R in one channel are correlated each other. This is evaluated as the covariance of measurements results on pseudo samples. The pseudo samples are $\cos\theta^*$ made by fluctuating, with Poisson statistics, the entry of each bin of the nominal distribution with data of 1.04 fb^{-1}. The figure 4.49, 4.50 and 4.51 show the result in each channel and the Table 4.11 summarize the correlation.

	ee channel	$\mu\mu$ channel	$e\mu$ channel
corr(F_0, F_L)	-0.90	-0.89	-0.95
corr(F_0, F_R)	-0.86	-0.90	-0.85
corr(F_L, F_R)	0.56	0.62	0.65

Table 4.11: The correlation between the two out of the three fraction values in each channel.

From the statistical point of view, the measurements in the three channels $ee, \mu\mu$ and $e\mu$ are independent since their event selections are completely exclusive each other by requiring two leptons of specific flavors.

As to the systematic uncertainties, following correlations are set.

type A

Uncertainty sources which does not care about the channels such as jet energy scale are treated as fully correlated. In this case, the covariant matrix is

$$A = \begin{pmatrix} 1 & 1 & 1 & -1 & -1 & -1 \\ 1 & 1 & 1 & -1 & -1 & -1 \\ 1 & 1 & 1 & -1 & -1 & -1 \\ -1 & -1 & -1 & 1 & 1 & 1 \\ -1 & -1 & -1 & 1 & 1 & 1 \\ -1 & -1 & -1 & 1 & 1 & 1 \end{pmatrix}. \tag{4.36}$$

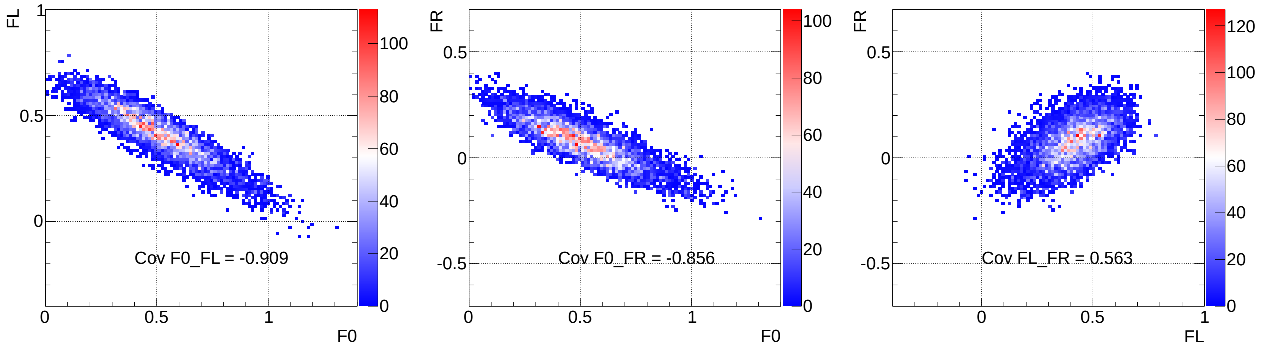

Figure 4.49: Distribution of the measurements on ensemble pseudo data set in di-electron channel.

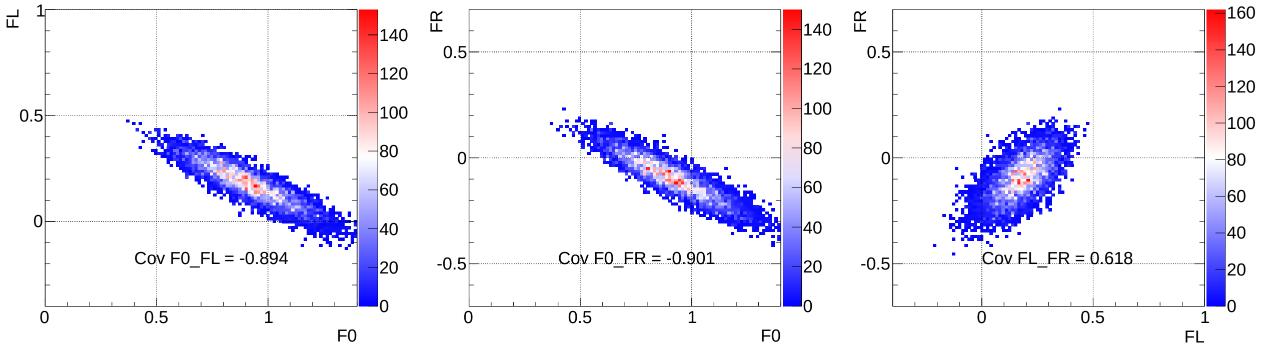

Figure 4.50: Distribution of the measurements on ensemble pseudo data set in di-muon channel

The component of 1 means correlation between the same quantity F_L or F_0 among the channels are correlated and the ones of -1 reflects the anti-correlation between the quantities.

type B

The uncertainty that cares lepton flavor is treated so that it reflect the fact. In this case, the covariant matrix is

$$B = \begin{pmatrix} 1 & 1 & 0 & -1 & -1 & 0 \\ 1 & 1 & 1 & -1 & -1 & -1 \\ 0 & 1 & 1 & 0 & -1 & -1 \\ -1 & -1 & 0 & 1 & 1 & 0 \\ -1 & -1 & -1 & 1 & 1 & 1 \\ 0 & -1 & -1 & 0 & 1 & 1 \end{pmatrix}. \tag{4.37}$$

This is the same as type A but with some components of 0, which is the consequence of no correlation between ee and $\mu\mu$ channels concerning the uncertainties from leptons.

type C

The uncertainty due to lack of templates' statistics is treated fully uncorrelated. In this case, the

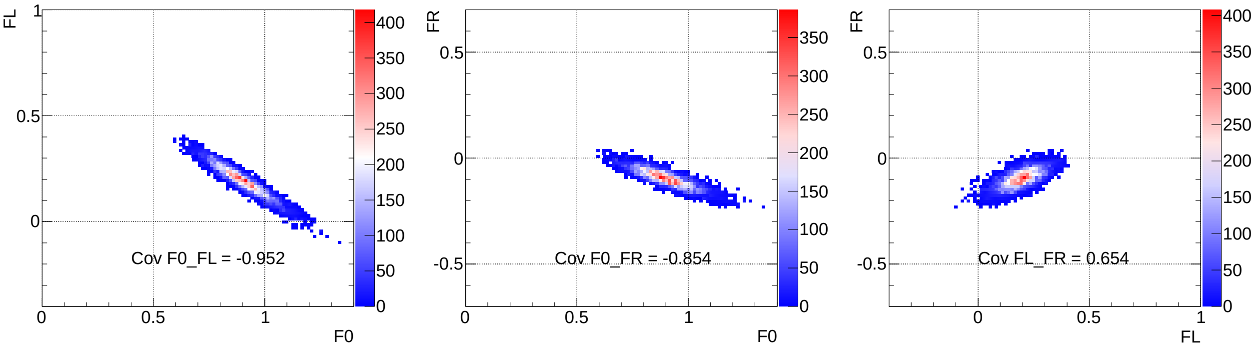

Figure 4.51: Distribution of the measurements on ensemble pseudo data set in emu channel

covariant matrix is

$$C = \begin{pmatrix} 1 & 0 & 0 & 0 & 0 & 0 \\ 0 & 1 & 0 & 0 & 0 & 0 \\ 0 & 0 & 1 & 0 & 0 & 0 \\ 0 & 0 & 0 & 1 & 0 & 0 \\ 0 & 0 & 0 & 0 & 1 & 0 \\ 0 & 0 & 0 & 0 & 0 & 1 \end{pmatrix}. \tag{4.38}$$

Under the conditions, the combined results are

$$\begin{aligned} F_0 &= 0.920 \pm 0.095(\text{stat.}) \pm 0.104(\text{syst.}) \\ F_L &= 0.172 \pm 0.063(\text{stat.}) \pm 0.074(\text{syst.}) \\ F_R &= -0.092 \pm 0.046(\text{stat.}) \pm 0.057(\text{syst.}) \end{aligned} \tag{4.39}$$

and Figure 4.52 shows the result after combining all the channels. Figure 4.53 shows the result on the F_0-F_R space. The deviation of the result from the SM expectation is 1.2 σ. The derived weights are summarized in Table 4.12. Similarly, the combined result of $F_R = 0$ fixed measurement is

$$F_0 = 0.716 \pm 0.048(\text{stat.}) \pm 0.090(\text{syst.}) \tag{4.40}$$

$$F_L = 0.284 \pm 0.048(\text{stat.}) \pm 0.090(\text{syst.}) \tag{4.41}$$

and no deviation from the Standard Model are seen.

4.4.4 The full combination of analyses in ATLAS

The obtained result is compared to other measurements in the ATLAS experiment. Especially, there is one measurement that uses the same method, template fitting, in order to extract the W boson polarization but in different channels, so-called single-lepton channel in which only one W boson decays leptonically. One other measurement uses the same di-lepton channel but extract the W boson polarization with a different method. These analyses are summarized in the reference [52]. and their

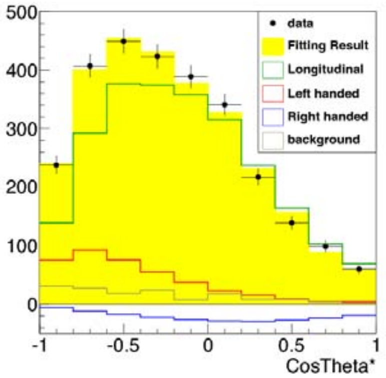

Figure 4.52: Combined template fitting result in the di-lepton channel. The yellow filled histogram is the sum of the three signals and the background, which are shown without stacking.

weight(%)		ω^{F_0}	ω^{F_L}
F_0	ee	-1.00	11.69
	$e\mu$	93.41	-20.78
	$\mu\mu$	7.59	9.09
F_L	ee	7.00	11.82
	$e\mu$	-2.64	60.15
	$\mu\mu$	-4.36	28.03

Table 4.12: The weight for di-lepton combination derived by BLUE method.

results are shown in Figure 4.54 : all of them are consistent with each other. The result of the full combination in the ATLAS experiment measurement is

$$\begin{aligned} F_0 &= 0.662 \pm 0.055(\text{stat.}) \pm 0.067(\text{syst.}) \\ F_L &= 0.326 \pm 0.031(\text{stat.}) \pm 0.034(\text{syst.}) \\ F_R &= 0.012 \pm 0.031(\text{stat.}) \pm 0.049(\text{syst.}) \end{aligned} \tag{4.42}$$

which is also consistent with the Standard Model.

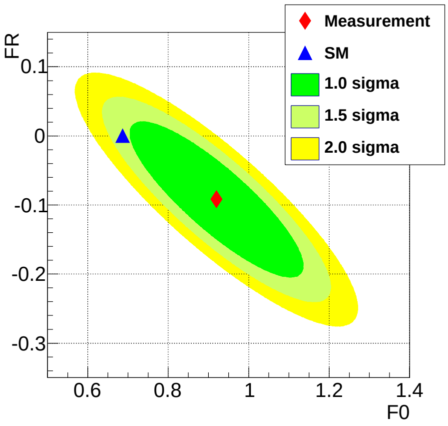

Figure 4.53: The the W boson polarization measurement result in the di-lepton channel on the F_0-F_R space. The deviation of the result from the SM expectation is 1.2 σ.

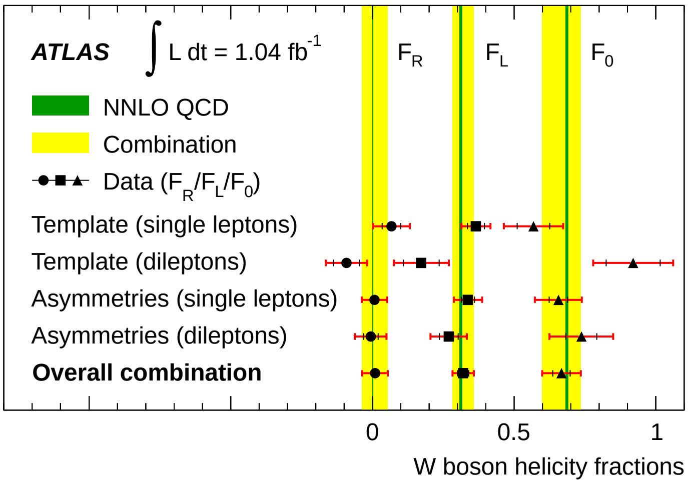

Figure 4.54: The W boson polarization measurements and their combination results from ATLAS experiment.

4.4.5 Physics Interpretation of the Measured W boson polarization

Finally, the result is translated into the parameters of the effective Lagrangian of equation (1.13) : V_L, g_L and g_R. Since the measurement result of the W boson polarization fraction is consistent with the SM, the parameters are assumed to be real, which means CP conservation. The translation is done by the *acceptance-rejection* method which is described below.

1. Take one random number for the parameter to be determined. The parameter $V_L = 1$ and the other parameters are assumed to be the values in the SM($V_R = g_L = g_R = 0$ unless it is the parameter being examined).
2. Translate the combination of V_L', V_R', g_L', g_R' into the W boson polarization fraction F_0', F_L', F_R'. A detail calculation is in the reference [10].
3. Calculate the probability P of the polarization fraction F_0', F_L', F_R' from the measurement results taking into account the correlation among the fractions.
4. Take a random number x in [0-1] and accept the parameter set V_L', V_R', g_L', g_R' if $x < P$.
5. Repeat the step(1-4) for appropriate times and make a histogram.
6. Regarding the normalized histogram as a probability density function, decide the interval for confidence level γ so that each out-side of the interval has probability $(1 - \gamma)/2$ as Figure 4.55 shows.

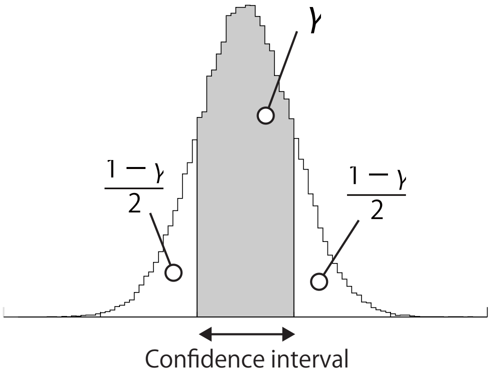

Figure 4.55: The definition of confidence interval with respect to the confidence level γ.

With the method, the confidence interval with 68% confidence level for each variables assuming the others are the SM value. The result from the template method in di-lepton channel analysis (equation (4.39)) are translated into

$$\mathrm{Re}(V_R) \in [-0.52 : 0.58] \tag{4.43}$$

$$\mathrm{Re}(g_L) \in [-0.26 : 0.23] \tag{4.44}$$

$$\mathrm{Re}(g_R) \in [-0.12 : 0.27] \tag{4.45}$$

which are consistent with the SM. Figure 4.56 shows the two-dimensional limits on each variables from the di-lepton analysis.

From the ATLAS combined result (equation (4.42)), the one-dimensional limits are

$$\mathrm{Re}(V_R) \in [-0.20, 0.20] \tag{4.46}$$

$$\mathrm{Re}(g_L) \in [-0.14, 0.11] \tag{4.47}$$

$$\mathrm{Re}(g_R) \in [-0.08, 0.04] \tag{4.48}$$

and the two-dimensional limit on $Re(g_L) - Re(g_R)$ space is Figure 4.57. All of them are also consistent with the SM.

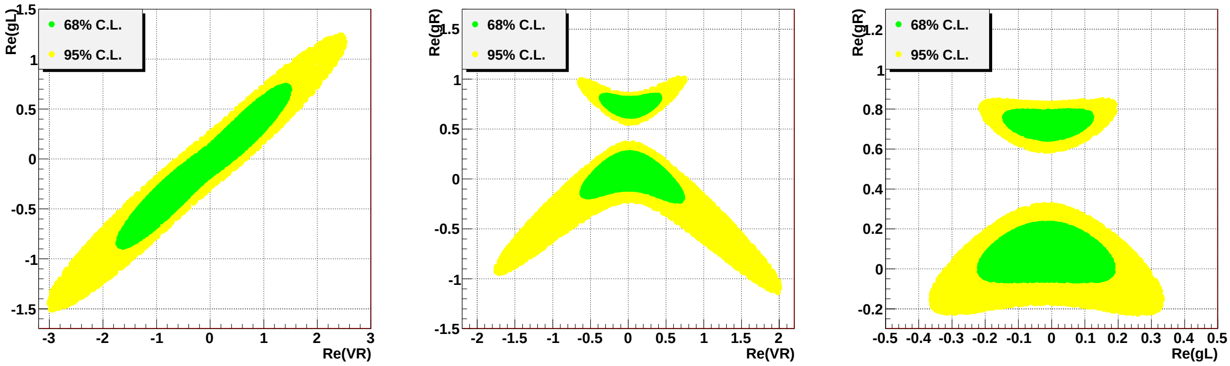

Figure 4.56: The constraint on the $\mathrm{Re}(V_R)$–$\mathrm{Re}(g_L)$ (left), $\mathrm{Re}(V_R)$–$\mathrm{Re}(g_R)$ (middle) and $\mathrm{Re}(g_L)$–$\mathrm{Re}(g_R)$ (right) parameter spaces from the dilepton analysis assuming imaginary parts of all the parameter and the real parts of them expect under consideration are zero

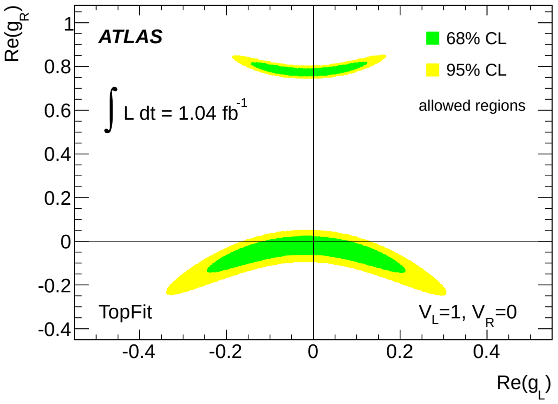

Figure 4.57: The constraint on the $Re(g_L)$ and $Re(g_R)$ parameter space from the ATLAS combined results, assuming $V_L = 1, V_R = 0, Im(g_L) = Im(g_R) = 0$.

Chapter 5

Summary

The W boson polarization fraction is measured with the $t\bar{t}$ that decay into di-lepton final state in pp collisions of 1.04 fb^{-1} in 7 TeV center of mass energy.

In the SM, the top quark decays into a W boson and a b-quark almost exclusively ($t \rightarrow Wb$) , with V-A weak interaction. And the theoretical expectation of the W boson polarization fraction is

$$
\begin{aligned}
F_0 &= 0.687 \pm 0.005 \\
F_L &= 0.311 \pm 0.005 \\
F_R &= 0.0017 \pm 0.0001
\end{aligned}
$$

where $0, L, R$ stands for longitudinal, left- and right-handed of the W boson polarization ($F_0{+}F_L{+}F_R = 1$). The strong suppression of F_R is one of the consequences of the V-A interaction.

The W boson polarization can be measured from the charged lepton emission angle distribution from the W boson. In this analysis, the angle θ^* is defined as the opening angle between the charged lepton momentum in the W boson rest frame and that of the W boson in the top quark rest frame. The angle θ^* in each events are reconstructed from momenta of the bottom quark, the charged lepton and the neutrino from each top quark.

The analysis focuses on the di-lepton final state in which high purity top quark samples can be prepared from 10^9 larger background thanks to the signature of the two charged leptons.

In this measurement, the charged leptons are one of the keys not only for the θ^* reconstruction but also for the triggers in the data taking. Especially, muon is better tool given the fact that it does not suffer from background compared to electron. On that point, this study focuses on the muon detection. The muon trigger system is established with systematic way during the commissioning period, and its trigger and reconstruction efficiencies are evaluated with proton collision data.

Concerning the $t\bar{t}$ event reconstruction, the two neutrinos in the event are also important. This analysis establishes method that can reconstruct the two top quark decay chains keeping the kinematical information. By applying the method on the selected events, the W boson polarization fraction is measured from θ^*(in practical, $\cos\theta^*$) distribution and the result is

$$
\begin{aligned}
F_0 &= 0.920 \pm 0.095(\text{stat.}) \pm 0.104(\text{syst.}) \\
F_L &= 0.172 \pm 0.063(\text{stat.}) \pm 0.074(\text{syst.}) \\
F_R &= -0.092 \pm 0.046(\text{stat.}) \pm 0.057(\text{syst.})
\end{aligned}
$$

which is consistent with the SM expectation: The background is lowered to almost negligible level (S/N = 15~16), and the uncertainty on the background contribution is less than 0.01. The result is also compared to the other three measurements in the ATLAS experiment and found to be consistent. By combining the di-lepton analysis with the other results in the ATLAS, the measurement archives the most presice measuremen in the world :

$$\begin{aligned} F_0 &= 0.662 \pm 0.055(\text{stat.}) \pm 0.067(\text{syst.}) \\ F_L &= 0.326 \pm 0.031(\text{stat.}) \pm 0.034(\text{syst.}) \\ F_R &= 0.012 \pm 0.031(\text{stat.}) \pm 0.049(\text{syst.}) \end{aligned} \tag{5.1}$$

From the result, the limit on the parameters in the effective Lagrangian (equation (1.13)) are set as

$$\begin{aligned} \text{Re}(V_R) &\in [-0.20, 0.20] \\ \text{Re}(g_L) &\in [-0.14, 0.11] \\ \text{Re}(g_R) &\in [-0.08, 0.04] \end{aligned}$$

which is consistent with the SM ($V_R = g_L = g_R = 0$).

This analysis is the first measurement of the W boson polarization in the top quark decay in proton-proton collisions at a center of mass energy of 7 TeV. Following the inclusive cross section measurement, this is a more precise measurement by focusing on kinematical variables and the results is consistent with the SM with its uncertainty. In addition to the method to reconstruct $t\bar{t}$ with the di-lepton final state, this study provides the validity of the $t\bar{t}$ production and decay modeling for the future analyses related to the $t\bar{t}$ di-lepton or di-lepton-like signatures such as a fourth-generation quark t' and the charged Higgs boson decays.

Bibliography

[1] J. Beringer et al. (Particle Data Group). The review of particle physics. *Phys. Rev. D*, Vol. 86, p. 010001, 2012.

[2] ATLAS collaboration. Observation of a new particle in the search for the standard model higgs boson with the atlas detector at the lhc. *Physics Letters B*, Vol. 716, No. 1, pp. 1 – 29, 2012.

[3] CMS collaboration. Observation of a new boson at a mass of 125 gev with the cms experiment at the lhc. *Physics Letters B*, Vol. 716, No. 1, pp. 30 – 61, 2012.

[4] Combination of CDF and D0 results on the mass of the top quark using up to 5.8 fb-1 of data. 2011.

[5] Jonathan Pumplin, Daniel Robert Stump, Joey Huston, Hung-Liang Lai, Pavel Nadolsky, and Wu-Ki Tung. New generation of parton distributions with uncertainties from global qcd analysis. *Journal of High Energy Physics*, Vol. 2002, No. 07, p. 012, 2002.

[6] FRANK-PETER SCHILLING. Top quark physics at the lhc: A review of the first two years. *International Journal of Modern Physics A*, Vol. 27, No. 17, p. 1230016, 2012.

[7] Combination of atlas and cms top-quark pair cross section measurements using up to 1.1 fb^{-1} of data at 7 tev. Technical Report ATLAS-CONF-2012-134, CERN, Geneva, Sep 2012.

[8] Andrzej Czarnecki, Jürgen G. Körner, and Jan H. Piclum. Helicity fractions of w bosons from top quark decays at next-to-next-to-leading order in qcd. *Phys. Rev. D*, Vol. 81, p. 111503, Jun 2010.

[9] T. Aaltonen, et al. Combination of CDF and D0 measurements of the W boson helicity in top quark decays. *Phys.Rev.*, Vol. D85, p. 071106, 2012.

[10] J.A. Aguilar-Saavedra, J. Carvalho, N. Castro, A. Onofre, and F. Veloso. Probing anomalous wtb couplings in top pair decays. *The European Physical Journal C*, Vol. 50, pp. 519–533, 2007.

[11] Werner Bernreuther, Patrick Gonzlez, and Martin Wiebusch. The top-quark decay vertex in standard model extensions. *The European Physical Journal C*, Vol. 60, pp. 197–211, 2009.

[12] Lyndon Evans and Philip Bryant. Lhc machine. *Journal of Instrumentation*, Vol. 3, No. 08, p. S08001, 2008.

[13] G Aad et al. *Journal of Instrumentation*, Vol. 3, No. 07, p. P07007, 2008.

[14] A. Ahmad et al. The silicon microstrip sensors of the atlas semiconductor tracker. *Nuclear Instruments and Methods in Physics Research Section A: Accelerators, Spectrometers, Detectors and Associated Equipment*, Vol. 578, No. 1, pp. 98 – 118, 2007.

[15] B. Aubert et al. Construction, assembly and tests of the atlas electromagnetic barrel calorimeter. *Nuclear Instruments and Methods in Physics Research Section A: Accelerators, Spectrometers, Detectors and Associated Equipment*, Vol. 558, No. 2, pp. 388 – 418, 2006.

[16] ATLAS Electromagnetic Liquid Argon Endcap Calorimeter Group et al. Construction, assembly and tests of the atlas electromagnetic end-cap calorimeters. *Journal of Instrumentation*, Vol. 3, No. 06, p. P06002, 2008.

[17] B. Aubert et al. Development and construction of large size signal electrodes for the atlas electromagnetic calorimeter. *Nuclear Instruments and Methods in Physics Research Section A: Accelerators, Spectrometers, Detectors and Associated Equipment*, Vol. 539, No. 3, pp. 558 – 594, 2005.

[18] *ATLAS liquid-argon calorimeter: Technical Design Report*. Technical Design Report ATLAS. CERN, Geneva, 1996.

[19] W.E. Cleland and E.G. Stern. Signal processing considerations for liquid ionization calorimeters in a high rate environment. *Nuclear Instruments and Methods in Physics Research Section A: Accelerators, Spectrometers, Detectors and Associated Equipment*, Vol. 338, No. 2-1, pp. 467–497, 1994.

[20] Hung-Liang Lai, Marco Guzzi, Joey Huston, Zhao Li, Pavel M. Nadolsky, Jon Pumplin, and C.-P. Yuan. New parton distributions for collider physics. *Phys. Rev. D*, Vol. 82, p. 074024, Oct 2010.

[21] Pavel M. Nadolsky, Hung-Liang Lai, Qing-Hong Cao, Joey Huston, Jon Pumplin, Daniel Stump, Wu-Ki Tung, and C.-P. Yuan. Implications of cteq global analysis for collider observables. *Phys. Rev. D*, Vol. 78, p. 013004, Jul 2008.

[22] S. Agostinelli et al. Geant4 simulation toolkit. *Nuclear Instruments and Methods in Physics Research Section A: Accelerators, Spectrometers, Detectors and Associated Equipment*, Vol. 506, No. 3, pp. 250 – 303, 2003.

[23] New atlas event generator tunes to 2010 data. Technical Report ATL-PHYS-PUB-2011-008, CERN, Geneva, Apr 2011.

[24] Jet shapes in atlas and mc modeling. Technical Report ATL-PHYS-PUB-2011-010, CERN, Geneva, Jul 2011.

[25] The ATLAS collaboration. Expected electron performance in the altas experiment. *ATLAS note*, 2011.

[26] The ATLAS collaboration. Muon reconstruction efficiency in reprocessed 2010 lhc proton-proton collision data recorded with the atlas detector. *ATLAS note*, 2011.

[27] Muon momentum resolution in first pass reconstruction of pp collision data recorded by atlas in 2010. Technical Report ATLAS-CONF-2011-046, CERN, Geneva, Mar 2011.

[28] The e/gamma combined performance group. Electron efficiency measurements using atlas 2010 data at sqrt(s) = 7 tev (atl-com-phys-2011-322). *ATLAS note*, 2011.

[29] Atlas calorimeter response to single isolated hadrons and estimation of the calorimeter jet scale uncertainty. Technical Report ATLAS-CONF-2011-028, CERN, Geneva, Mar 2011.

[30] Peter Z. Skands. Tuning monte carlo generators: The perugia tunes. *Phys. Rev. D*, Vol. 82, p. 074018, Oct 2010.

[31] Georges Aad, et al. Jet energy measurement with the ATLAS detector in proton-proton collisions at sqrt(s) = 7 TeV. 2011.

[32] G Piacquadio and C Weiser. A new inclusive secondary vertex algorithm for b-jet tagging in atlas. *Journal of Physics: Conference Series*, Vol. 119, No. 3, p. 032032, 2008.

[33] Torbjrn Sjstrand, Stephen Mrenna, and Peter Skands. Pythia 6.4 physics and manual. *Journal of High Energy Physics*, Vol. 2006, No. 05, p. 026, 2006.

[34] et al. Aad G. *Expected performance of the ATLAS experiment: detector, trigger and physics*. CERN, Geneva, 2009.

[35] Trigger operation public results. Technical report, CERN, Geneva.

[36] Performance of the atlas electron and photon trigger in p-p collisions at sqrts = 7 tev in 2011. Technical Report ATLAS-CONF-2012-048, CERN, Geneva, May 2012.

[37] Performance of the atlas muon trigger in 2011. Technical Report ATLAS-CONF-2012-099, CERN, Geneva, Jul 2012.

[38] The ATLAS Collaboration. The atlas experiment at the cern large hadron collider. *Journal of Instrumentation*, Vol. 3, No. 08, p. S08003, 2008.

[39] A. Gorisek. Commissioning and first operational experience of the atlas beam conditions and loss monitors based on pcvd diamond sensors. *Nuclear Instruments and Methods in Physics Research Section A: Accelerators, Spectrometers, Detectors and Associated Equipment*, Vol. 617, No. 1-3, pp. 444–448, 2010. Proceedings of the 11th Pisa Meeting on Advanced Detectors.

[40] Luminosity determination in pp collisions at sqrt(s) = 7 tev using the atlas detector in 2011. Technical Report ATLAS-CONF-2011-116, CERN, Geneva, Aug 2011.

[41] Richard D. Ball, Luigi Del Debbio, Stefano Forte, Alberto Guffanti, Jose I. Latorre, et al. A first unbiased global NLO determination of parton distributions and their uncertainties. *Nucl.Phys.*, Vol. B838, pp. 136–206, 2010.

[42] A.D. Martin, W.J. Stirling, R.S. Thorne, and G. Watt. Parton distributions for the LHC. *Eur.Phys.J.*, Vol. C63, pp. 189–285, 2009.

[43] Paolo Nason and Bryan Webber. Next-to-Leading-Order Event Generators. *Ann.Rev.Nucl.Part.Sci.*, Vol. 62, pp. 187–213, 2012.

[44] Peter Zeiler Skands. Tuning Monte Carlo Generators: The Perugia Tunes. *Phys.Rev.*, Vol. D82, p. 074018, 2010.

[45] Nikolaos Kidonakis. Next-to-next-to-leading-order collinear and soft gluon corrections for t-channel single top quark production. *Phys. Rev. D*, Vol. 83, p. 091503, May 2011.

[46] Georges Aad, et al. Measurement of the top quark-pair production cross section with ATLAS in pp collisions at $\sqrt{s} = 7$ TeV. *Eur.Phys.J.*, Vol. C71, p. 1577, 2011.

[47] B et al. Acharya. Estimation of the w+jets background for top quark re-discovery in the single lepton+jets channel. Technical Report ATL-PHYS-INT-2010-136, CERN, Geneva, Dec 2010.

[48] Michael G. Albrow, et al. Tevatron-for-LHC Report of the QCD Working Group. 2006.

[49] Andy Buckley, Hendrik Hoeth, Heiko Lacker, Holger Schulz, and Jan Eike von Seggern. Systematic event generator tuning for the LHC. *Eur.Phys.J.*, Vol. C65, pp. 331–357, 2010.

[50] Louis Lyons, Duncan Gibaut, and Peter Clifford. How to combine correlated estimates of a single physical quantity. *Nuclear Instruments and Methods in Physics Research Section A: Accelerators, Spectrometers, Detectors and Associated Equipment*, Vol. 270, No. 1, pp. 110 – 117, 1988.

[51] Andrea Valassi. Combining correlated measurements of several different physical quantities. *Nuclear Instruments and Methods in Physics Research Section A: Accelerators, Spectrometers, Detectors and Associated Equipment*, Vol. 500, No. 1-3, pp. 391–405, 2003. NIMA Vol 500.

[52] ATLAS collaboration. Measurement of the w boson polarization in top quark decays with the atlas detector. *Journal of High Energy Physics*, Vol. 2012, pp. 1–46, 2012. 10.1007/JHEP06(2012)088.